Origin of anomalous magnetotransport in kagome superconductors AV$_3$Sb$_5$ (A = K,Rb,Cs)

A. E. Koshelev [1,2] R. Chapai [1] D. Y. Chung,[1] J. F. Mitchell [1] and U. Welp [1]

[1]*Materials Science Division, Argonne National Laboratory, Lemont, Illinois 60439, USA*
[2]*Department of Physics and Astronomy, University of Notre Dame, Notre Dame, Indiana 46656, USA*

Multiple anomalous features in electronic spectra of metals with a kagome lattice structure—van Hove singularities, Dirac points, and flat bands—imply that materials containing this structural motif may lie at a nexus of topological and correlated electron physics. Due to the prospects of such exceptional electronic behavior, the recent discovery of superconductivity coexisting with charge-density wave (CDW) order in the layered kagome metals AV$_3$Sb$_5$ (A = K,Rb,Cs) has attracted considerable attention. Notably, these archetypal kagome metals express unconventional magnetotransport behavior, including an unexpected linear-in-H diagonal resistivity at low fields, and an even more peculiar, nonmonotonic sign-changing behavior of the Hall resistivity, which has been speculated to arise from a chiral CDW. We argue here that this unusual magnetotransport derives not from such unconventional phenomena, but rather from the unique fermiology of the AV$_3$Sb$_5$ materials. Specifically, it is caused by a large, concave hexagonal Fermi surface sheet formed in the close proximity to the van Hove singularities, which is backfolded into a small hexagonal sheet and two large triangular sheets in the CDW state. We introduce and analyze a model of the electronic structure of these Fermi surface sheets that allows for a full analytical treatment within Boltzmann kinetic theory and that enables semi-quantitative fits of our transport data. Specifically, we find that the anomalous magnetotransport behavior is caused by the confluence of strong reduction of the Fermi velocity near the van Hove singularities located near the vertices of the hexagonal sheet and sharp corners in Fermi surface generated by the CDW reconstruction. Our analytical approach not only explains the anomalous magnetotransport in the kagome superconductors but also can be extended to a variety of metallic systems hosting singular features in their Fermi surfaces.

I. INTRODUCTION

Kagome lattices composed of networks of corner-sharing triangles have been recognized as a fertile ground to realize novel electronic and magnetic phenomena. Metallic materials with layered kagome-lattice crystal structure display multiple anomalous features in their electronic band structure including Dirac points, van Hove singularities, and flat bands [1–3]. These features inspired several theoretical proposals for exotic electronic states [2–10] such as bond order, loop current state, chiral charge-density wave or unconventional superconductivity. Against this background, the recent discovery of kagome-lattice superconductors AV$_3$Sb$_5$ with A = K,Rb,Cs [11] attracted considerable attention and triggered extensive research activity, see recent reviews [12–15]. The dominant structural motif in these layered materials are kagome nets of vanadium atoms formed around antimony honeycomb lattices. These materials display two electronic instabilities [12–15]: a charge-density wave transition at T_{CDW} = 80–100 K followed by superconducting transition at T_{SC} = 1–2.7 K (in particular, for CsV$_3$Sb$_5$, T_{CDW} = 94 K and T_{SC} = 2.7 K). The CDW instability develops simultaneously at three wave vectors (3Q CDW). The possible realizations are 2 × 2 reconstructions in the form of star of David, inverse star of David (or trihexagonal) patterns, or alternating combination of these states [16]. In addition, experimental indications of chiral charge order and time-reversal symmetry breaking have been reported [17–24]. The exact nature of the CDW order and its relation to superconductivity remain open issues.

The band structure of the kagome superconductors experimentally determined by angle-resolved photoemission spectroscopy (ARPES) [25–33] and quantum oscillations [16,34–39] is qualitatively consistent with electronic band-structure calculations based on density-functional theory (DFT) [16,27,34,40–43]. The Fermi surface (FS) is rather complicated and contains several sheets. In the unfolded hexagonal Brillouin zone (BZ) without CDW order the main pockets are (i) a warped cylindrical pocket around the Γ point derived from *Sb* 5p orbitals, (ii) a large concave hole hexagon derived from 3d orbitals of V, and (iii) convex triangular pockets around K points. While the Dirac points and flat bands are separated from the Fermi energy, the van Hove points are very close [25,27,28,41,42] and affect many physical properties of these materials. In particular, the van Hove singularities are expected to have a pronounced influence on both CDW [2,6,8–10,44] and superconducting [2,6,45–49] instabilities. The 3Q CDW order reconstructs the Fermi-surface structure [30,39,40,43], with the large hexagon pocket being the most significantly transformed.

The kagome superconductors are characterized by unusual magnetotransport behavior below the CDW transition [37,50–53]. The magnetoresistance exhibits a linear field dependence at low fields up to ~1 tesla and at higher fields a downward curvature develops followed by a second region of quasilinear growth with smaller slope. The Hall resistivity is negative at small magnetic fields but shows a pronounced nonmonotonic behavior and changes sign in fields of several kG. At

fields higher than 5 tesla the behavior becomes linear again with the slope strongly dependent on temperature. The unusual small-field behavior of the Hall resistivity has been attributed to the so-called anomalous Hall effect [50,51,53], which may be caused by chiral or time-reversal symmetry breaking states [54].

Here we propose that these unusual features in magnetotransport mostly originate from unique features of the Fermi surface of kagome metals. In particular, the unusual transport behavior is induced by the proximity of the Fermi level to van Hove singularities. In this paper, we present a combined theoretical and experimental study of the magnetotransport of CsV_3Sb_5 crystals. We demonstrate that the anomalous behavior mainly originates from the large hexagonal Fermi pocket in the pristine Brillouin zone due to (i) proximity of its corners to the van Hove points and (ii) its overall concave shape. This observation implies that the proximity to the van Hove singularity has a profound influence on transport behavior in these materials, as it has been recognized before for other systems, see, e.g., Refs. [55–57].

We introduce a simplified minimum model for this Fermi surface allowing for a full analytical consideration. We evaluate the magnetoconductivity both in the pristine phase and the low-temperature 3Q CDW state, where the large hexagon is transformed into a small hexagon and two large triangular sheets. The reconstructed Fermi surface is characterized by sharp corners which enhances the small-field magnetoresistivity. Our model is motivated by our recent observation of a series of break-down orbits in high-field quantum oscillation measurements [39], by the observation that the magnetoresistance increases strongly at the CDW transition (see, e.g., Ref. [37] and discussion below), and by recent DFT calculations [43]. The model provides a qualitative description of the behavior for both the diagonal and Hall conductivity. It also accounts for the strong increase of the magnetoresistance in the CDW state.

Although the large hexagon is nominally a hole pocket, the small-field linear Hall conductivity is *negative*. The reason for this anomalous feature is the velocity reduction near the van Hove points leading to suppression of the hole contribution to the Hall conductivity near the corners. As a result, the concave hexagon sides provide a dominant negative contribution. Strong velocity variations along the Fermi surfaces also lead to strong field dependences of both conductivity components. An important feature of these field dependences is the existence of two magnetic field scales originating from van Hove singularities: the lower scale is set by the two effective masses determining the saddle-point electronic spectrum at the van Hove point while the upper scale logarithmically diverges when the Fermi energy approaches the van Hove energy. The reconstruction of the large hexagon pocket does not change qualitatively the low-field nonmonotonic behavior of the Hall conductivity. On the other hand, this reconstruction generates sharp corners in the new Fermi pockets leading to enhancement of the low-field diagonal magnetoconductivity with linear magnetic field dependence. This linear magnetoconductivity naturally appears in materials with charge and spin density waves having a nonideal nesting. In such materials the reconstruction of the Fermi surface in the folded Brillouin zone leads to the formation of Fermi pockets with

sharp corners. The interruption of the smooth orbital motion of quasiparticles along the Fermi surface at these corners leads to linear magnetoconductivity [58–60] and also to strongly field-dependent Hall conductivity [61]. The rounding of the corners due to finite CDW gap leads to the crossover from a linear to a quadratic field dependence of the diagonal conductivity when magnetic fields drops below the typical value proportional to the gap. Besides the low-field linear behavior, the field dependence of the diagonal conductivity is characterized by an intermediate $1/H$ field dependence between the two field scales set by the van Hove singularity and crosses over to standard $1/H^2$ at higher fields. We demonstrate that the Hall conductivity from the reconstructed pockets qualitatively reproduce shapes of the experimental field dependences.

This paper is organized as follows. In Sec. II, we illustrate the anomalous behavior of the magnetoconductivity that we aim to explain. In Sec. III, we introduce the model for the large hexagon pocket on which our calculations of anomalous magnetotransport are based. In Sec. IV, we consider the reconstructed Fermi surface arising due to the onset of the 3Q CDW order emphasizing a small hexagonal Fermi surface sheet near the zone centered surrounded by large triangular sheets. In Sec. V, we introduce the orbital-integral approach for the calculation of the magnetoconductivity, which is based on the relaxation-time approximation of the Boltzmann transport equation. The theoretical analysis of the magnetoconductivity arising from the large hexagonal hole Fermi surface sheet in the unfolded Brillouin zone is presented in Sec. VI, while in Sec. VII, we compute the magnetoconductivity components for the reconstructed Fermi surface consisting of small hexagon triangle and two large triangular pockets and in Sec. VIII, we analyze the modification of the magnetoconductivity due to the CDW order. In Sec. X, we present our experimental magnetotransport data and their qualitative modeling.

II. ANOMALOUS BEHAVIOR OF MAGNETOCONDUCTIVITY IN CsV_3Sb_5 IN CDW STATE

As an illustration of the anomalous behavior, we show in Fig. 1 the magnetic field dependences of the diagonal and Hall conductivities for CsV_3Sb_5 at 10 K. These conductivities are extracted from the experimentally measured diagonal and Hall resistivities, as discussed in more detail below, in Sec. X. The standard quadratic field dependence of σ_{xx} for the magnetic field H applied along the c axis is limited to very small fields, below 0.1 T, as illustrated in the lower-left inset of Fig. 1. At higher fields up to ~1 T, the magnetoconductivity has linear field dependence followed by upward curvature and a crossover in the range 1.5–3 T to a second region of quasi-linear variation. The behavior of the Hall conductivity σ_{xy} is more complicated. In low fields σ_{xy} is negative. However, at fields <0.3 tesla, it displays a nonmonotonic dependence and changes sign. At even higher field σ_{xy} passes through a smooth maximum.

The unusual small-field behavior of σ_{xy} has been attributed to the so-called anomalous Hall effect [50,51,53,62], i.e., by the manifestation of the spontaneous Hall effect, which may arise without magnetic field in parity-breaking states, such as chiral CDW, or time-reversal symmetry breaking such
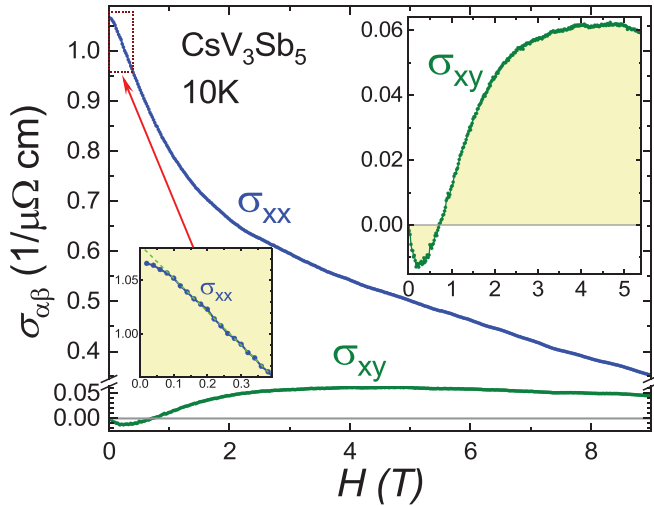
FIG. 1. The diagonal and Hall conductivities of CsV_3Sb_5 at 10 K. The upper-right inset shows the anomalous behavior of $\sigma_{xy}(H)$ in the expanded vertical scale and the lower-left inset zooms into the low-field behavior of $\sigma_{xx}(H)$ illustrating the crossover between the quadratic and linear regimes near 0.1 T. The dashed green line shows linear fit within the range 0.15–0.5 T.
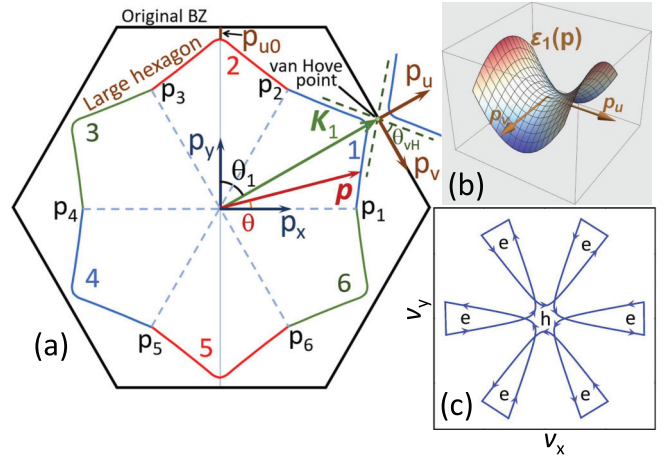

FIG. 2. (a) The large concave hexagon Fermi pocket approximated by the hyperbolic segments. (b) Saddle-point spectrum near the van Hove point. (c) The velocity contour corresponding to this Fermi surface, which determines the linear Hall term [63], Eq. (33). The central small hexagon corresponds to locations near the van Hove points and gives the hole contribution to the Hall conductivity, while the six outside "petals" give electronic contribution.

as loop-current order [54]. In this interpretation, the region near the inflection point around 1 tesla is treated as a linear background. After subtraction of this background, the curve $\sigma_{xy}(H)$ acquires a plateaulike region in the range 0.5–1.5 tesla, which is interpreted as the anomalous Hall contribution. This interpretation, however, is not straightforward. Strictly speaking, in the case of a single chiral domain, a Hall conductivity should be finite even in zero magnetic field. In the scenario where the zero-field Hall conductivity averages to zero due to multiple domains with opposite chiralities, and the plateau appears because the magnetic field selects a definite chirality, one would expect a hysteretic behavior, which was not observed. Despite of these rather obvious issues, the "anomalous Hall effect" interpretation is widely cited in the literature as one of experimental indications for the realization of a chiral CDW state in the kagome family AV_3Sb_5.

We demonstrate that the overall behavior of the conductivity components, especially the Hall conductivity, can be more naturally and straightforwardly explained as arising from the fermionic properties of the large hexagon pocket. In the next section, we present a simple model for this pocket which we employ in our analytic calculations of magnetoconductivity.

III. MODEL FOR THE LARGE CONCAVE HEXAGON POCKET

In this section, we introduce a model for the large concave hexagon pocket in the unreconstructed original Brillouin zone, which we will use to evaluate the components of conductivity in magnetic field. As illustrated in Fig. 2(a), this pocket is mostly determined by the van Hove points which are located near the six wave vectors K_j with

$$K_{j,x} = K \cos\left(-\frac{\pi}{6} + \frac{\pi}{3}j\right), \quad (1a)$$

$$K_{j,y} = K \sin\left(-\frac{\pi}{6} + \frac{\pi}{3}j\right), \quad (1b)$$

where $j = 1, 2, \ldots, 6$, $K = 2\pi/(\sqrt{3}a)$ is half of the basic reciprocal-lattice vector for the unfolded BZ, and a is the lattice parameter (5.45 Å for CsV_3Sb_5 [34]). Note that, due to BZ periodicity, the vectors K_j and $K_{j+3} = -K_j$ point to the same van Hove point meaning that there are only three nonequivalent van Hove points. In the vicinity of these wave vectors, $|p - K_j| \ll K$, we can expand momentum p using the local basis, $p = K_j + p_u e_l + p_v e_t$, where e_l and e_t are the unit vectors along and perpendicular to K_j. The local momenta (p_v, p_u) are connected with the global momenta (p_x, p_y) as

$$p_v = (p_x - K_{j,x})\cos\theta_j + (p_y - K_{j,y})\sin\theta_j, \quad (2a)$$

$$p_u = -(p_x - K_{j,x})\sin\theta_j + (p_y - K_{j,y})\cos\theta_j, \quad (2b)$$

where $\theta_j = (\pi/3)(j-2)$ is the rotation angle of the local frame, see Fig. 2(a). In the local coordinates, the electronic spectrum has a saddle-point shape illustrated in Fig. 2(b),

$$\varepsilon_j(p) = \frac{p_u^2}{2m_u} - \frac{p_v^2}{2m_v}, \quad (3)$$

where m_u and m_v are the effective masses. The shape of the Fermi surface near K_j is determined by the equation $\varepsilon_j(p) = \varepsilon_{vH}$, where ε_{vH} is the Fermi energy measured with respect to the van Hove point. In a 3D layered metal, it depends on the c-axis momentum p_z. At $\varepsilon_{vH} = 0$, the Fermi surfaces are given by straight van Hove lines, $p_u = \pm p_v/\sqrt{r_m} = \pm \tan\theta_{vH}\, p_v$, where the mass ratio $r_m = m_v/m_u$ determines the van Hove angle as $\tan\theta_{vH} = 1/\sqrt{r_m}$. For reference, the mass ratio r_m and other key parameters used in the paper are listed in Table I. At a finite separation between the van Hove point and Fermi level ε_{vH}, the Fermi surfaces are given by hyperbola branches located near every vector K_j,

$$p_{F,u}(p_v) = -\sqrt{p_{u0}^2 + p_v^2/r_m} = -\sqrt{p_{v0}^2 + p_v^2}/\sqrt{r_m} \quad (4)$$

TABLE I. Definitions of the key parameters used throughout the paper.

Quantity	Notation and definition
Mass ratio for saddle-point spectrum	$r_m = m_v/m_u$
Reduced magnetic field	$\omega_h = \lvert e\rvert H\tau/(c\sqrt{m_u m_v})$
Lower magnetic field scale	$H_0 = c\sqrt{m_u m_v}/(\lvert e\rvert\tau)$
Upper magnetic field scale	$H_b = 2t_b H_0$
Conductivity slice scale	$S_0 = 3\tau p_{u0}^2/\sqrt{m_u m_v}$
Ratio of reciprocal-lattice vector and separation from van Hove point	$\kappa = K/p_{u0}$
Boundary hyperbolic parameter	$\sinh t_b = \frac{\sqrt{3r_m}\kappa - \sqrt{\kappa^2 + 3r_m - 1}}{3r_m - 1}$
Crossing-point hyperbolic parameter	$\tanh t_c = 1/\sqrt{3r_m}$

with $p_{u0} = \sqrt{2m_u\varepsilon_{\mathrm{vH}}}$ being the distance between the hexagon corner and van Hove point, see Fig. 2(a), and $p_{v0} = \sqrt{2m_v\varepsilon_{\mathrm{vH}}} = \sqrt{r_m}\,p_{u0}$. The minus sign in Eq. (4) corresponds to the hexagon inside the first BZ. Due to the BZ periodicity, the branches located near opposite wave vectors $\boldsymbol{K}_j$ and $-\boldsymbol{K}_j$ are, in fact, two branches of the same hyperbola. The hexagon is concave if $\theta_{\mathrm{vH}} > 30°$ corresponding to $r_m < 3$. From the ARPES and DFT data for CsV_3Sb_5 [16,27], we estimate $\theta_{\mathrm{vH}} \approx 39°$ giving $\sqrt{r_m} \approx 1.23$ and $r_m \approx 1.51$. We will use $r_m = 1.5$ in the illustrative plots. The Fermi velocity components can be represented as

$$v_u = \frac{p_u}{m_u} = -\frac{\sqrt{p_{v0}^2 + p_v^2}}{\sqrt{m_u m_v}}, \tag{5a}$$

$$v_v = -\frac{p_v}{m_v}, \tag{5b}$$

giving the total in-plane velocity at the Fermi surface

$$v = \sqrt{\frac{p_u^2}{m_u^2} + \frac{p_v^2}{m_v^2}} = \sqrt{v_{u0}^2 + \frac{p_v^2}{m_v^2}(1 + r_m)}. \tag{6}$$

The key feature that strongly influences the magnetotransport behavior is that the velocity drops linearly on approaching the van Hove point, $v \simeq p_v\sqrt{1 + r_m}/m_v$. The minimum value $v_{u0} = p_{u0}/m_u$ is realized at the hexagon corner. Exactly at the van Hove point for $\varepsilon_{\mathrm{vH}} = 0$, the velocity vanishes.

To reveal the qualitative behavior, we will use a simple approximate model for the electronic spectrum in the form of a piecewise function composed of hyperbolic segments

$$\varepsilon(p_x, p_y) = \varepsilon_l(\boldsymbol{p}), \quad \text{for } \frac{\pi}{3}(l-1) < \theta < \frac{\pi}{3}l, \tag{7}$$

where θ is the polar angle of the momentum $p_x = p\cos\theta$, $p_y = p\sin\theta$. This approximation means that the Fermi surface is composed of hyperbola branches located between the momenta p_l and p_{l+1}, see Fig. 2(a). We only need this approximation in the vicinity of the Fermi surface. The piecewise hyperbolic approximation allows for a full analytical evaluation of the conductivity components in arbitrary magnetic fields. The price paid for the model simplicity is the jumps of the Fermi velocities at the boundaries between the regions. Nevertheless, in spite of its simplicity, the model captures the essential anomalous features of magnetoconductivity. As

suggested by the shape of Fermi surface in Eq. (4), calculations can be conveniently carried out using the hyperbolic parametrization,

$$p_v = -p_{v0}\sinh t, \quad p_u = -p_{u0}\cosh t, \tag{8}$$

which automatically places the momentum at the Fermi surface within every segment. Here the hyperbolic parameter t is located within the interval $-t_b < t < t_b$. At the boundaries between the segments, we have the geometric relation $\sqrt{3}\lvert p_v\rvert + \lvert p_u\rvert = K$ yielding the equation for the limiting hyperbolic parameter t_b,

$$\sqrt{3r_m}\sinh t_b + \cosh t_b = \kappa, \tag{9}$$

with $\kappa = K/p_{u0} \gg 1$, which has the following exact solution:

$$\sinh t_b = \frac{\sqrt{3r_m}\kappa - \sqrt{\kappa^2 + 3r_m - 1}}{3r_m - 1}. \tag{10}$$

In the limit of very large κ this gives a simpler approximate relation $\exp(t_b) \approx 2\kappa/(\sqrt{3r_m} + 1)$, i.e., the parameter t_b diverges logarithmically on approaching the van Hove point, $t_b \propto \ln(K/p_{u0})$ for $p_{u0} \to 0$.

IV. CDW RECONSTRUCTION OF THE LARGE HEXAGON IN THE FOLDED BRILLOUIN ZONE

The 3Q CDW order leads to the folding of the Brillouin zone. The folded BZ is given by a hexagon with four times smaller area, as shown in Fig. 3(a). During this folding, all three van Hove points are displaced to the BZ center and the segments of the large hexagon Fermi surface shown in Fig. 2(a) are shifted to the center, $\boldsymbol{p} \to \boldsymbol{p} - \boldsymbol{K}_j$, and reconstructed at the crossings [39]. Three crossing hyperbolas form the electronic hyperbolic-hexagon (HH) pocket at the center, as illustrated in Figs. 3(a) and 3(b). The outside branches form two holelike triangular pockets in the extended BZ, see Fig. 3(c). This reconstruction affects magnetotransport mostly by modifying the pattern of quasiparticle orbital motion in the magnetic field. On the one hand, the formation of sharp corners and their rounding due to the opening of CDW gaps affects the magnetoconductivity at small magnetic fields. On the other hand, modification of pocket areas affects magnetotransport at high magnetic fields.

Let us consider first the structure of the small hyperbolic-hexagon pocket. The HH pocket is composed of three crossing hyperbolas rotated $60°$ with respect to each other. This corresponds to six crossing segments. Near the crossing points, the spectra are reconstructed due to the CDW order. We will maintain the same segment numbering for the original and displaced branches, see Fig. 3(a). For every segment, one can again introduce a local rotated coordinate system (p_v, p_u). Since hyperbolas are now located near the center, in the relation between the local and global momenta, Eqs. (2a) and (2b), we have to remove the shifts by the vectors $\boldsymbol{K}_j$. In these local coordinates, the saddle-point hyperbolic spectrum is again given by Eq. (3). At a finite positive shift of the Fermi level from the van Hove point, $\varepsilon_{\mathrm{vH}} > 0$, the hyperbolic Fermi-surface branches are given by the Eq. (4). The parameter $p_{u0} = \sqrt{2m_u\varepsilon_{\mathrm{vH}}}$ becomes the minimal distance between the hyperbola and origin, see Fig. 3(b). Contrary to the large hexagon, the Fermi surface of the small hexagon is very
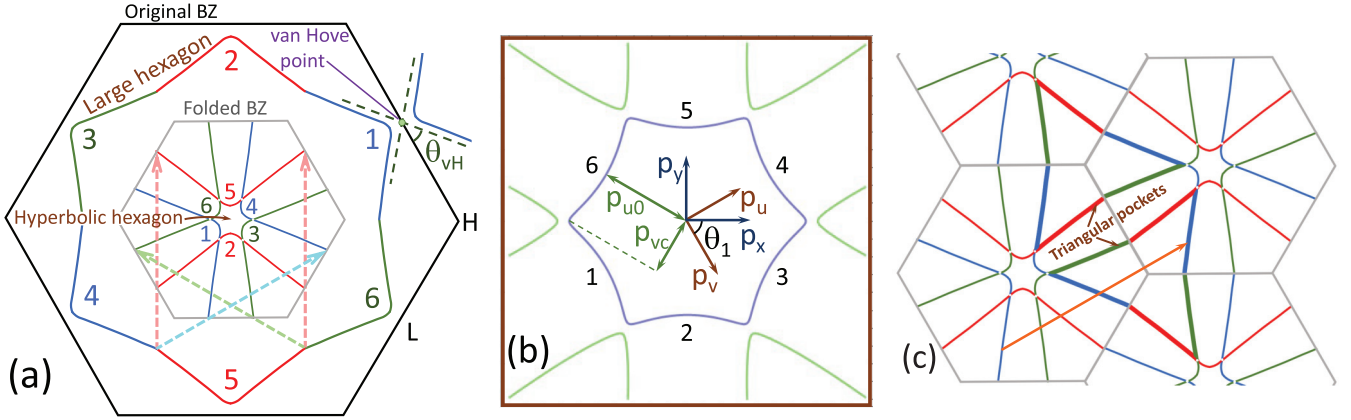
FIG. 3. (a) The large concave hexagon in the original Brillouin zone has vertices close to the three van Hove points. The segments corresponding to the hyperbola branches are color coded. The 3Q CDW reconstruction leads to the formation of a small "hyperbolic hexagon" Fermi pocket in the folded Brillouin zone and outside branches which form two large triangles in the extended Brillouin zone, as illustrated in (c). The dashed arrows in (a) show the CDW wave vectors transferring the colored segments of the original large hexagon into the folded Fermi surface. The van Hove points are transferred to the center. The sharpness of the "hyperbolic hexagon" and of the triangles corners is due to the small value of CDW gap. (b) Zoom into the "hyperbolic hexagon" Fermi pocket which appears due to CDW reconstruction at the crossing points. The definitions of the local coordinates (p_v, p_u) for the first segment as well as the two key geometrical parameters p_{u0} and p_{vc} are also illustrated. (c) Triangular pockets formed in the extended Brillouin zone. The orange arrow shows the reciprocal lattice vector connecting identical branches. Coloring emphasizes that Fermi surfaces of these pockets are composed from the pieces belonging to different hyperbolic branches.

accurately described by the hyperbolic branches due to its immediate proximity to the van Hove points. That is why we use the name "hyperbolic hexagon" for this pocket. For our calculations, the Fermi surface shape in Eq. (4) can be again conveniently parametrized in terms of hyperbolic functions, Eq. (8).

Neglecting the reconstruction due to opening of CDW gap, a hyperbolic branch crosses with the neighboring branch at the angle of $30°$ with respect to the p_u axis. This corresponds to the condition $|p_u| = \sqrt{3}|p_v|$ and gives the relation between the p_v coordinate of the crossing point and p_{u0},

$$p_{vc} = \frac{p_{u0}}{\sqrt{3 - 1/r_m}}. \tag{11}$$

In the hyperbolic parametrization defined by Eq. (8), the crossing takes place at $t = t_c$ with $\tanh t_c = 1/\sqrt{3r_m}$, yielding

$$t_c = \frac{1}{2} \ln \frac{\sqrt{3r_m} + 1}{\sqrt{3r_m} - 1}. \tag{12}$$

We will present the final results for the conductivity components of the reconstructed Fermi surface using this parameter together with the parameter t_b in Eq. (10). For a finite CDW gap, sharp corners at the crossings become rounded, see Fig. 3(b).

In Appendix A 1, we evaluate the HH area A_{HH} and effective mass m_{HH}, which can be probed by magnetic oscillations [34–39]

$$A_{HH} = 6\sqrt{r_m} t_c p_{u0}^2, \tag{13a}$$

$$m_{HH} = \frac{1}{2\pi} \frac{dA_{HH}}{d\varepsilon_F} = \frac{6}{\pi} t_c \sqrt{m_u m_v}. \tag{13b}$$

Clearly, the HH area is always somewhat larger than the area of an ideal hexagon with the same p_{u0}, $A_{hex} = 2\sqrt{3} p_{u0}^2 \approx 3.464 p_{u0}^2$, corresponding to the inequality $\sqrt{3r_m} \ln \frac{\sqrt{3r_m}+1}{\sqrt{3r_m}-1} > 2$.

The relations in Eqs. (13a) and (13b) allow for the estimation of the key parameters p_{u0} and m_u from the experimental data. If we take the oscillation frequency $F_\gamma = 226$ T attributed to hexagon pocket cross section at the top of the Brillouin zone [39], we estimate for the extremal cross section $A_{HH} = 0.0216 \text{ Å}^{-2}$ and $p_{u0} = 0.076 \text{ Å}^{-1}$, which is ∼6% of the size of the original unfolded Brillouin zone, $k_{BZ} = \frac{4\pi}{\sqrt{3}a} = 1.33 \text{ Å}^{-1}$. With experimental value $m_{HH} = 0.71 m_e$ and $r_m = 1.51$, we estimate from Eq. (13b) $m_u = 0.59 m_e$ and $m_v = 0.9 m_e$.

Let us consider now the configuration of the outside triangular pockets. In our model, each triangular pocket is composed of six hyperbola branches with different centers and rotations, see Figs. 3(c) and 4. Each side of the triangle contains two segments belonging to different hyperbolas. We will call these branches as "outgoing" and "incoming", referring to the direction of orbital motion with respect to the hyperbolic hexagon pocket, see Fig. 4. The momentum located at one of the branches of the triangular Fermi surface can be presented as

$$p_x = K_{m,x} + p_v \cos\theta_j - p_u \sin\theta_j, \tag{14a}$$

$$p_y = K_{m,y} + p_v \sin\theta_j + p_u \cos\theta_j, \tag{14b}$$

where $\theta_j = (\pi/3)(j - 2)$, the components of the vectors $\mathbf{K}_m$ are defined in Eqs. (1a) and (1b), and we also added zero vector $K_{0,x} = K_{0,y} = 0$. For example, the lower triangle is located between the vectors $\mathbf{K}_0$, $\mathbf{K}_1$, and $\mathbf{K}_6$, see Fig. 4 and its corresponding indices m, j are summarized in Table II. We will use the same parametrization for hyperbolic coordinates p_v and p_u as for the large hexagon in Eq. (8). The difference is that for the outgoing branches the hyperbolic parameter t varies in the limits $t_c < t < t_b$ and for the incoming branches it varies in the limit $-t_b < t < -t_c$.
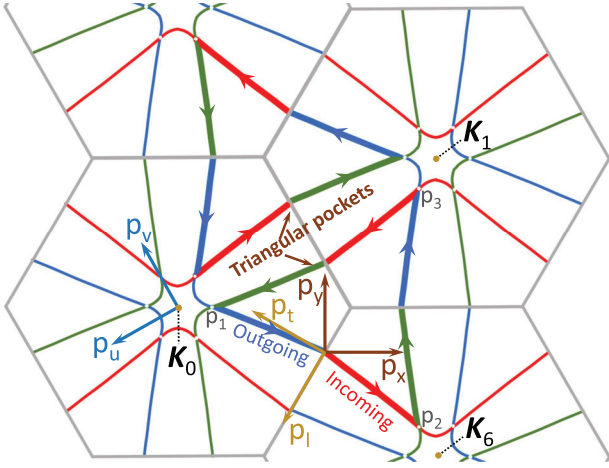
FIG. 4. Geometry of the triangular pockets for the reconstructed Fermi surface. Every side of the triangle is composed of the incoming and outgoing segments belonging to different hyperbolas which can be indexed by the location of its center K_m and rotation angle θ_j. Three axes sets used in the paper are shown: laboratory frame (p_x, p_y), hyperbolic basis (p_u, p_v), and transverse and longitudinal directions (p_t, p_l) for selected side segment.

The area of the triangular pocket is evaluated in Appendix A 2 as

$$
A_{\rm T} = p_{u0}^2 \left[\frac{\sqrt{3}}{2} (3r_m \sinh^2 t_b - \cosh^2 t_b) - 3\sqrt{r_m}(t_b - t_c) \right]
$$
$$
\simeq \frac{\sqrt{3}}{2} K^2 \frac{\sqrt{3r_m} - 1}{\sqrt{3r_m} + 1}. \tag{15}
$$

This area mostly determines the high-field asymptotics of the Hall conductivity, as will be discussed below. Note that the total area of two triangular pockets is more than two times smaller than the area of the large hexagon. We approximately evaluate the effective mass of the triangular pocket as

$$
m_T \approx \frac{3}{\pi}(t_b - t_c)\sqrt{m_u m_v}. \tag{16}
$$

It is larger than the effective mass of the hyperbolic hexagon in Eq. (13b) due to the presence of the large factor t_b.

V. MAGNETOCONDUCTIVITY VIA ORBIT INTEGRALS

Transverse magnetoconductivity of most metallic materials originates from classical orbital mechanism, which arises due to the bending of quasiparticle trajectories by the magnetic field [58,64]. We assume that the system can be described by the quasiclassical Boltzmann equation within the relaxation-

time approximation. In this case, the conductivity tensor for the magnetic field along the z axis can be represented as [60,65]

$$
\sigma_{\alpha\beta} = 2e^2 \sum_{\rm pockets} \int \frac{dp_z}{(2\pi)^3} S_{\alpha\beta}(p_z), \tag{17}
$$

where $S_{\alpha\beta}(p_z)$ describes the contribution from a single orbit at a single p_z slice, which for closed orbits can be written as

$$
S_{\alpha\beta} = \varsigma_{\alpha\beta} \frac{c}{|e|H} \left[1 - \exp\left(-\frac{H_O}{H}\right) \right]^{-1}
$$
$$
\times \oint \frac{dp}{v} v_\beta \oint_p^{p'} \frac{dp'}{v'} v'_\alpha \exp\left(-\int_p^{p'} \frac{dp''}{v''} \frac{c}{|e|H\tau}\right), \tag{18}
$$

where v and τ are the Fermi velocity and the isotropic scattering time, respectively, $\varsigma_{\alpha\alpha} = 1$, $\varsigma_{xy} = -\varsigma_{yx} = 1(-1)$ for an electron (hole) pocket,

$$
H_O = \frac{c}{|e|} \oint \frac{dp}{v} \frac{1}{\tau}
$$

is the field at which the time required to complete the full orbit is equal to the scattering time. For brevity, we will call the quantity $S_{\alpha\beta}$ a conductivity slice. All integrals are performed along fixed-p_z orbits along the Fermi surface and $\oint$ notates the counterclockwise integration over the whole orbit [66]. This "tube-integral" presentation provides a convenient basis for the analysis of the conductivity when the Fermi velocity v has sharp features leading to complicated magnetic field dependences. A similar orbital approach has been used for modeling of anisotropic magnetotransport of cuprate superconductors [67–69].

In the case of a Fermi surface with m-fold symmetry, which can be split into m equivalent segments each having mirror symmetry, we derive in Appendix B a convenient presentation for the conductivity slices containing only integrals for a single segment,

$$
S_{xx}^{(m)} = \frac{m}{2} \frac{c}{|e|H} \left\{ \mathcal{G}_{tt} + \mathcal{G}_{ll} - {\rm Re}\left[\frac{(\mathcal{R}_t + \imath \mathcal{R}_l)^2}{\exp\left(-\imath \frac{2\pi}{m}\right) - \eta} \right] \right\}, \tag{19a}
$$

$$
S_{xy}^{(m)} = \varsigma_{xy} \frac{m}{2} \frac{c}{|e|H} \left\{ \mathcal{G}_{lt} - \mathcal{G}_{tl} + {\rm Im}\left[\frac{(\mathcal{R}_t + \imath \mathcal{R}_l)^2}{\exp\left(-\imath \frac{2\pi}{m}\right) - \eta} \right] \right\}, \tag{19b}
$$

where the indices t and l refer to transverse and longitudinal projections of Fermi velocities inside the segments and the quantities η, $\mathcal{R}_s$, and $\mathcal{G}_{sr}$ are defined in terms of segment integrals as

$$
\eta = \exp\left(-\int_{p_{\rm i}}^{p_{\rm f}} \frac{dp'}{v'} \frac{c}{|e|H\tau}\right), \tag{20a}
$$

$$
\mathcal{R}_s = \int_{p_{\rm i}}^{p_{\rm f}} \frac{dp'}{v'} v'_s \exp\left(-\int_{p_{\rm i}}^{p'} \frac{dp''}{v''} \frac{c}{|e|H\tau}\right), \tag{20b}
$$

$$
\mathcal{G}_{sr} = \int_{p_{\rm i}}^{p_{\rm f}} \frac{dp}{v} v_s \int_p^{p_{\rm f}} \frac{dp'}{v'} v'_r \exp\left(-\int_p^{p'} \frac{dp''}{v''} \frac{c}{|e|H\tau}\right) \tag{20c}
$$

TABLE II. The indices m, j in Eqs. (14a) and (14b) defining central vectors K_m and rotation angles θ_j for for six branches in the lower triangular pocket, see Fig. 4.

m, j	1	2	3
out	0,4	6,6	1,2
in	6,5	1,1	0,3

with $s, r = l, t$. Here the momenta p_i and p_f define segment limits. The terms with the functions $\mathcal{G}_{sr}$ and $\mathcal{R}_s$ represent the contributions from the integration over p and p' in Eq. (18) belonging to the same and different segments of the Fermi surface, respectively.

Generally, the calculation of the conductivity using the above orbital-integral method requires knowledge of the electronic spectrum and local scattering time. Although electronic spectra can be obtained through *ab initio* DFT calculations, detailed microscopic information about scattering times is typically unavailable requiring some simplifying assumptions. Moreover, calculations with a fully realistic electronic spectrum can only be performed numerically. In our case, however, using the simple minimum model of the large hexagon pocket outlined in Sec. III and its subsequent reconstruction discussed in Sec. IV, we can analytically evaluate all orbital integrals and derive closed analytical results for the conductivity slices in Eqs. (19a) and (19b) for both original and reconstructed Fermi sheets. This will allow us to perform a qualitative analysis of the conductivity behavior in a magnetic field.

VI. MAGNETOCONDUCTIVITY FROM LARGE CONCAVE HEXAGON IN UNFOLDED BRILLOUIN ZONE

The anomalous behavior of magnetotransport in kagome superconductors is observed at low temperatures, when the Fermi surface is reconstructed by the CDW order [50,51,53,62]. Nevertheless, we consider first the magnetoconductivity for the large concave hexagon in the unfolded Brillouin zone, because it provides a convenient point of reference and already has a nonstandard behavior due to the proximity to the van Hove singularities. In particular, we will see that the Hall conductivity actually has a shape similar to the experimental one in Fig. 1 pointing to its van Hove origin. Also, the behavior of the Hall conductivity in this case is of general interest, since it represents an almost textbook example of a hole-type Fermi surface with *negative* sign of σ_{xy} at small fields.

We use the general results derived in Appendix B for conductivity slices $S_{x\beta}$ of an arbitrary Fermi pocket with m-fold symmetry, as summarized in Eqs. (19a) and (19b). For the hexagon hole Fermi pocket ($m = 6$), these results become

$$S_{xx}^{\mathrm{LH}} = \frac{3c}{|e|H}\left\{\mathcal{G}_{vv}^{\mathrm{LH}} + \mathcal{G}_{uu}^{\mathrm{LH}} - \frac{\left(\frac{1}{2} - \eta_{\mathrm{LH}}\right)\left[\left(\mathcal{R}_v^{\mathrm{LH}}\right)^2 - \left(\mathcal{R}_u^{\mathrm{LH}}\right)^2\right] - \sqrt{3}\mathcal{R}_v^{\mathrm{LH}}\mathcal{R}_u^{\mathrm{LH}}}{1 - \eta_{\mathrm{LH}} + \eta_{\mathrm{LH}}^2}\right\}, \tag{21a}$$

$$S_{xy}^{\mathrm{LH}} = -\frac{3c}{|e|H}\left\{-2\mathcal{G}_{vu}^{\mathrm{LH}} + \frac{\frac{\sqrt{3}}{2}\left[\left(\mathcal{R}_v^{\mathrm{LH}}\right)^2 - \left(\mathcal{R}_u^{\mathrm{LH}}\right)^2\right] + \left(\frac{1}{2} - \eta_{\mathrm{LH}}\right)2\mathcal{R}_v^{\mathrm{LH}}\mathcal{R}_u^{\mathrm{LH}}}{1 - \eta_{\mathrm{LH}} + \eta_{\mathrm{LH}}^2}\right\}. \tag{21b}$$

Here, the parameter η_{LH} and segment integrals $\mathcal{R}_k^{\mathrm{LH}}$ and $\mathcal{G}_{km}^{\mathrm{LH}}$ are defined by Eqs. (20a)–(20c). The indices $k = v, u$ and $m = v, u$ correspond to the velocity projections to the directions of the local rotated hyperbolic coordinates, which in this case correspond to the transverse and longitudinal directions of the segments. Therefore the p and p' integration over the hyperbolic segments in Eqs. (20a)–(20c) can be analytically carried out expanding the velocity over the local rotated basis and using the hyperbolic parametrization defined in Eq. (8), as described in Appendix C. For the parameter η_{LH} in Eq. (20a), we obtain

$$\eta_{\mathrm{LH}} = \exp\left(-2t_b/\omega_h\right), \tag{22}$$

where t_b is defined in Eq. (10) and

$$\omega_h \equiv \omega_c\tau = H/H_0 = |e|H\tau/(c\sqrt{m_u m_v}) \tag{23}$$

is the reduced magnetic field with the field scale $H_0 = c\sqrt{m_u m_v}/(|e|\tau)$. The ratio in the exponent $2t_b/\omega_h$ is the ratio of the time to pass one hexagon segment $t_{\mathrm{segm}} = 2ct_b\sqrt{m_u m_v}/(|e|H)$ to the scattering time τ. This ratio defines the second field scale, $H_b = 2t_b H_0 \simeq 2\ln\frac{2K/p_{u0}}{\sqrt{3r_m}+1}H_0$, which is much larger than H_0 and diverges on approaching the van Hove singularity for $p_{u0} \to 0$. The integrals $\mathcal{R}_k^{\mathrm{LH}}$ in Eq. (20b) are evaluated as $\mathcal{R}_v^{\mathrm{LH}} = p_{u0}G_{bv}$, $\mathcal{R}_u^{\mathrm{LH}} = -p_{v0}G_{bu}$, with the reduced functions

$$G_{bv} = \frac{1}{1 - \omega_h^{-2}}\left[-\cosh t_b + \frac{1}{\omega_h}\sinh t_b + \left(\cosh t_b + \frac{1}{\omega_h}\sinh t_b\right)\eta_{\mathrm{LH}}\right], \tag{24a}$$

$$G_{bu} = \frac{1}{1 - \omega_h^{-2}}\left[\sinh t_b - \frac{1}{\omega_h}\cosh t_b + \left(\sinh t_b + \frac{1}{\omega_h}\cosh t_b\right)\eta_{\mathrm{LH}}\right]. \tag{24b}$$

In turn, the same-segment integrals $\mathcal{G}_{km}^{\mathrm{LH}}$ defined in Eq. (20c) are evaluated as $\mathcal{G}_{vv}^{\mathrm{LH}} = p_{u0}^2 \mathcal{K}_{bvv}$, $\mathcal{G}_{uu}^{\mathrm{LH}} = p_{v0}^2 \mathcal{K}_{buu}$, and $\mathcal{G}_{vu}^{\mathrm{LH}} = -p_{u0}p_{v0}\mathcal{K}_{bvu}$ with

$$\mathcal{K}_{bvv} = \frac{1}{1 - \omega_h^{-2}}\left[-\left(\cosh t_b + \frac{1}{\omega_h}\sinh t_b\right)G_{bv} - \frac{\sinh(2t_b) - 2t_b}{2\omega_h}\right], \tag{25a}$$

$$\mathcal{K}_{buu} = \frac{1}{1 - \omega_h^{-2}}\left[\left(\sinh t_b + \frac{1}{\omega_h}\cosh t_b\right)G_{bu} - \frac{\sinh(2t_b) + 2t_b}{2\omega_h}\right], \tag{25b}$$

$$\mathcal{K}_{bvu} = \frac{1}{1 - \omega_h^{-2}}\left[\frac{\frac{1}{\omega_h} - \eta_{\mathrm{LH}}\left(\sinh t_b + \frac{1}{\omega_h}\cosh t_b\right)\left(\cosh t_b + \frac{1}{\omega_h}\sinh t_b\right)}{1 - \omega_h^{-2}} + t_b\right]. \tag{25c}$$

Note that, in spite of the denominators $1 - \omega_h^{-2}$ in the above formulas, all functions have regular behavior for $\omega_h \to 1$.

For numerical evaluations, we rewrite the results in Eqs. (21a) and (21b) in the dimensionless form as

$$S_{\alpha\beta}^{\mathrm{LH}} = S_0 F_{\alpha\beta}^{\mathrm{LH}}, \tag{26a}$$

$$F_{xx}^{\mathrm{LH}} = \frac{1}{\omega_h}\left[\mathcal{K}_{bvv} + r_m \mathcal{K}_{buu} - \frac{\left(\frac{1}{2} - \eta_{\mathrm{LH}}\right)\left(G_{bv}^2 - r_m G_{bu}^2\right) + \sqrt{3 r_m} G_{bv} G_{bu}}{1 - \eta_{\mathrm{LH}} + \eta_{\mathrm{LH}}^2} \right], \tag{26b}$$

$$F_{xy}^{\mathrm{LH}} = -\frac{1}{\omega_h}\left[-2\sqrt{r_m}\mathcal{K}_{buv} + \frac{\frac{\sqrt{3}}{2}\left(G_{bv}^2 - r_m G_{bu}^2\right) - \left(\frac{1}{2} - \eta_{\mathrm{LH}}\right)2\sqrt{r_m} G_{bv} G_{bu}}{1 - \eta_{\mathrm{LH}} + \eta_{\mathrm{LH}}^2} \right]. \tag{26c}$$

Here

$$S_0 = 3\tau p_{u0}^2 / \sqrt{m_u m_v} \tag{27}$$

the overall scale for $S_{\alpha\beta}$, which we will use throughout the paper. The dimensionless functions $F_{\alpha\beta}^{\mathrm{LH}}$ of the reduced magnetic field ω_h also depend on two parameters, the mass ratio r_m and the limiting hyperbolic parameter t_b which in turn is determined by r_m and the ratio $\kappa = K/p_{u0}$ in Eq. (10). The latter parameter diverges on approaching the van Hove point for $\varepsilon_{\mathrm{vH}} \to 0$. At large t_b, the functions $F_{\alpha\beta}^{\mathrm{LH}}$ scale as $\exp(2t_b) \propto \kappa^2$ meaning that the main scale of $S_{\alpha\beta}^{\mathrm{LH}}$ is $S_0\kappa^2 = 3\tau K^2/\sqrt{m_u m_v}$, which does not depend on p_{u0}. As a consequence, the slices $S_{\alpha\beta}^{\mathrm{LH}}$ only weakly depend on the distance to the van Hove point $\varepsilon_{\mathrm{vH}}$. We can also note that the product $S_0 H_0 = 3p_{u0}^2 c/|e|$ does not depend on the scattering rate and effective masses and is only determined by the distance between the LH corner and the van Hove point p_{u0}. As follows from Eq. (17), the total contribution of the large hexagon to the conductivity components are obtained by the integration of the slices $S_{\alpha\beta}^{\mathrm{LH}}$ over the c-axis momentum p_z. Most importantly, the distance to the van Hove point p_{u0} depends on p_z and this distance determines both S_0 and t_b.

The key feature determining the behavior of the magnetotransport is the slowing down of the orbital motion near the van Hove points, see Eq. (6). To understand the behavior of the large-hexagon magnetoconductivity at the qualitative level, we will study the dependences $F_{\alpha\beta}^{\mathrm{LH}}(\omega_h)$ at the different values of p_{u0} (or, equivalently, the parameter $\kappa = K/p_{u0}$). A quick inspection of the above results suggests that for $\kappa \gg 1$, these dependences are characterized by two scales of the magnetic field corresponding to $\omega_h \sim 1$ and $\omega_h \sim 2t_b \gg 1$, where the second scale logarithmically diverges when the Fermi energy approaches the van Hove point.

Consider first the behavior of the diagonal function F_{xx}^{LH}. Using the low-field expansions of the reduced functions G_{bk} and $\mathcal{K}_{bkk}$ listed in Appendix C, in Eqs. (C11a), (C11b), (C15), and (C16), we obtain the small-field asymptotics of F_{xx}^{LH},

$$F_{xx}^{\mathrm{LH}} \simeq \frac{r_m + 1}{2} \sinh(2t_b) + (r_m - 1)t_b - \frac{\omega_h}{2}(\sqrt{3}\sinh t_b - \sqrt{r_m}\cosh t_b)^2. \tag{28}$$

The finite linear term here is an artifact of the approximate model, it appears due to velocity jumps at the boundaries between the segments. Numerically, this term is rather small. At higher magnetic fields $\omega_h \gg 1$, using asymptotics in

Eqs. (C19a) and (C19b) also listed in Appendix C, we obtain a simple approximate result

$$F_{xx}^{\mathrm{LH}} \simeq \frac{\kappa^2}{2\omega_h}\frac{1 - \eta_{\mathrm{LH}}^2}{1 - \eta_{\mathrm{LH}} + \eta_{\mathrm{LH}}^2}. \tag{29}$$

As follows from the definition of η_{LH} in Eq. (22), nominally, this function describes a crossover between $1/\omega_h$ behavior for $1 \ll \omega_h \ll 2t_b$ and $1/\omega_h^2$ for $\omega_h \gg 2t_b$. However, since $t_b \sim \ln\kappa$ and the logarithm is a slowly growing function, the first asymptotics is only pronounced for extremely large κ. The highest-field asymptotics of F_{xx}^{LH} is $F_{xx}^{\mathrm{LH}} \simeq 2\kappa^2 t_b/\omega_h^2$.

The full field dependence at the van Hove point, $\kappa \to \infty$, is

$$F_{xx}^{\mathrm{LH}}/\kappa^2 \to \frac{1}{(\sqrt{3 r_m} + 1)^2}\left\{\left[1 - \frac{\omega_h^2}{(1 + \omega_h)^2}\right](1 + r_m) - \frac{\omega_h/2}{(1 + \omega_h)^2}(\sqrt{3} - \sqrt{r_m})^2\right\}. \tag{30}$$

In this case, the high-field decay remains $\propto 1/\omega_h$ in the whole field range $\omega_h \gg 1$ without crossover to $1/\omega_h^2$ limit. Therefore the intermediate $1/\omega_h$ asymptotics is the distinct qualitative feature induced by van Hove singularities. Plots of $F_{xx}^{\mathrm{LH}}(\omega_h)$ for $r_m = 1.5$ and different values of κ are shown in the lower panel of Fig. 5.

The behavior of the Hall component F_{xy}^{LH} in Eq. (26c) is more peculiar. The linear Hall term in small magnetic fields, following from the low-field limits of the functions G_{bs} and $\mathcal{K}_{buv}$ [see Eqs. (C11a), (C11b), and (C18) in Appendix C], can be evaluated as

$$F_{xy}^{\mathrm{LH}} \simeq -\omega_h\left[\frac{1}{2}(\sqrt{3}\sinh t_b - \sqrt{r_m}\cosh t_b)\right.$$
$$\left. \times (\sinh t_b + \sqrt{3 r_m}\cosh t_b) - 2\sqrt{r_m}t_b\right]$$
$$\approx -\frac{\kappa^2\omega_h}{2}\frac{\sqrt{3} - \sqrt{r_m}}{1 + \sqrt{3 r_m}}. \tag{31}$$

The linear Hall component is *negative*, in spite of the hole nature of the large hexagon pocket (its Fermi surface surrounds empty states). It is straightforward to understand the origin of this unusual feature. Due to its concave shape, the Fermi surface is composed of pieces with both curvatures. Since the regions with positive curvature are located near the van Hove points where the Fermi velocity is small, their contribution is suppressed resulting in the dominating electron-like (negative) contribution of the sections with negative curvature.
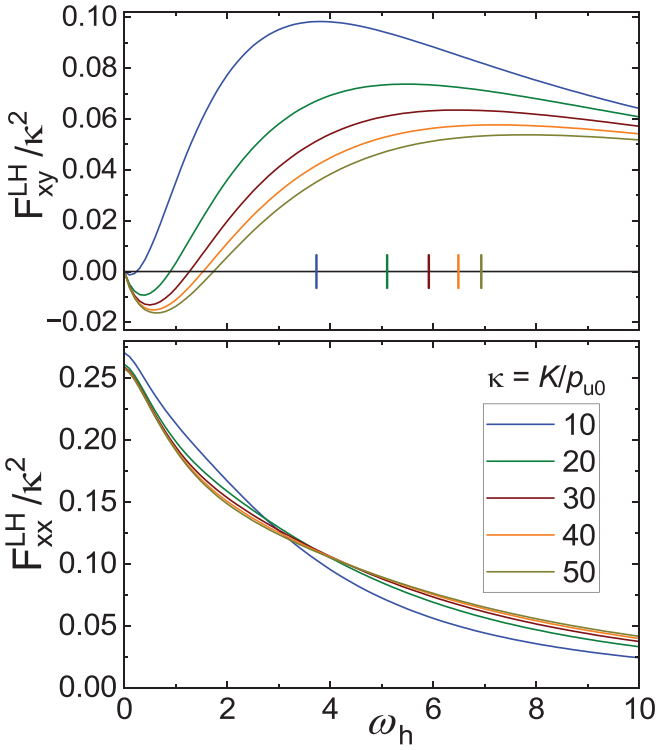
FIG. 5. The dependences of the functions $F_{\alpha\beta}^{\mathrm{LH}}$ on the reduced magnetic field ω_h. These functions determine the slice contributions to the diagonal and Hall conductivities and are defined in Eqs. (26b) and (26c). The plots are made for for $r_m = 1.5$ and different values of the parameter $\kappa = K/p_{u0}$, characterizing proximity to the van Hove point. The vertical bars in the upper plot mark the crossover fields $\omega_h = 2t_b \propto \ln \kappa$.

A simple general geometric interpretation of the linear Hall magnetoconductivity has been suggested by Ong [63], who demonstrated that in the two-dimensional case σ_{xy} is proportional by the area A_l swept by the vector mean-free path $\boldsymbol{l} = \tau \boldsymbol{v}$ during a full orbital cycle, $A_l = \frac{1}{2} \oint (l_y dl_x - l_x dl_y)$. For constant scattering time A_l is proportional to the area A_v swept by the velocity, $A_l = \tau^2 A_v$ with

$$A_v = \frac{1}{2} \oint (v_y dv_x - v_x dv_y) \qquad (32)$$

and in our case, we have

$$S_{xy} = \frac{|e|H\tau^2}{c} A_v \qquad (33)$$

in the small-field limit. Note that areas swept clockwise and counterclockwise contribute to A_v with opposite signs. Figure 2(c) illustrates the velocity contour corresponding to the large concave hexagon Fermi surface shown in Fig. 2(a). It is composed of the central small hexagon corresponding to the regions near the van Hove points and six outside "petals." The area inside the small hexagon is swept clockwise corresponding to holelike contribution, while total area inside the petals which are swept counterclockwise gives electron contribution to A_v and S_{xy}. As the Fermi energy approaches the van Hove point, the central hexagon shrinks and contribution from the

"petals" dominates yielding the total negative sign of the Hall term.

The field range for the linear behavior, however, is rather narrow. The regions near the van Hove points also induce strong field dependence of F_{xy}^{LH}. At higher magnetic fields $\omega_h \gg 1$, using approximate limits for the functions G_{bs} and $\mathcal{K}_{buv}$ listed in Eqs. (C19a) and (C19c), we obtain a simple approximate result,

$$F_{xy}^{\mathrm{LH}} \simeq -\frac{\kappa^2}{2\omega_h} \left[\frac{\sqrt{3} - \sqrt{r_m}}{1 + \sqrt{3r_m}} - \frac{\sqrt{3}\eta_{\mathrm{LH}}}{1 - \eta_{\mathrm{LH}} + \eta_{\mathrm{LH}}^2} \right]. \qquad (34)$$

This function describes the crossover between the two $1/\omega_h$ dependences with opposite signs,

$$F_{xy}^{\mathrm{LH}} \simeq \frac{\kappa^2}{2(1 + \sqrt{3r_m})\omega_h}$$

$$\times \begin{cases} -(\sqrt{3} - \sqrt{r_m}), & \text{for } 1 \ll \omega_h \ll 2t_b \\ 4\sqrt{r_m}, & \text{for } \omega_h \gg 2t_b \end{cases}. \qquad (35)$$

This means that F_{xy}^{LH} changes sign. It is known that the highest-field asymptotics of the Hall conductivity does not depend on the shape of the Fermi surface and is determined only by the type and density of the carriers [64]. In our case, this corresponds to the relation

$$S_{xy}^{\mathrm{LH}} \simeq \frac{A_{\mathrm{LH}}}{|e|H/c}, \qquad (36)$$

where A_{LH} is the area of the large-hexagon pocket, which can be evaluated as $A_{\mathrm{LH}} \approx \frac{6\sqrt{r_m}K^2}{1+\sqrt{3r_m}}$ for the Fermi energy at the van Hove point. The high-field asymptotics in Eq. (35) reproduces this result. On the other hand, the intermediate-filed asymptotics in Eq. (35) corresponds to

$$S_{xy}^{\mathrm{LH}} \simeq \frac{A_{\mathrm{LH}} - A_{\mathrm{hex}}}{|e|H/c}, \qquad (37)$$

where $A_{\mathrm{hex}} \approx \frac{3\sqrt{3}}{2}K^2$ is the area inside the ideal hexagon composed of straight lines connecting the van Hove points. In Fig. 5, we also present plots of $F_{xy}^{\mathrm{LH}}(\omega_h)$ for different values of κ. We see that the field dependences are nonmonotonic and F_{xy}^{LH} changes sign at the magnetic field progressively increasing with κ. At higher fields F_{xy}^{LH} has a smooth maximum. We immediately notice that these shapes resemble the shape of experimental curve $\sigma_{xy}(H)$ for CsV_3Sb_5 shown in Fig. 1 strongly suggesting that the unusual behavior of the Hall conductivity in this material has van Hove origin. The absence of anomalous behavior above the CDW transition is most likely related by high scattering rates leading to large magnetic-field scales. In addition, it is clear that the magnetotransport in this material at low temperatures is also affected by the Fermi

surface reconstruction by CDW, which we analyze in the next section.

VII. MAGNETOCONDUCTIVITY FROM RECONSTRUCTED POCKETS

A. Hyperbolic hexagon pocket

As discussed in Sec. IV, reconstruction of the large hexagon pocket by the 3Q CDW order leads to formation of small hyperbolic hexagon sheet near the BZ center and two large triangular sheets, see Fig. 3. In this section, we consider the contribution of the hyperbolic hexagon to the diagonal conductivity neglecting the CDW gaps near the branch crossings. In this case, the interruption of the smooth motion along the orbit at the sharp corners leads to linear magnetoconductivity [58–60]. The general result for the diagonal and Hall conductivity slices is given by Eqs. (21a) and (21b), where the large-hexagon label LH has to be replaced by the hyperbolic-hexagon label HH. The only differences are in the values of parameter η_{HH} and the segment integrals $\mathcal{R}_s^{\text{HH}}$ and $\mathcal{G}_{sr}^{\text{HH}}$. In calculations, we will employ the same hyperbolic parametrization as for the large hexagon, Eq. (8). Two differences with respect to the large hexagon are (i)the crossing of hyperbolas is determined by the parameter t_c in Eq. (12), which is much smaller than the parameter t_b in Eq. (10) and (ii) the counterclockwise direction of motion along HH Fermi surface corresponds to change of the hyperbolic parameter from t_c to $-t_c$.

The p and p' integration over hyperbolic segments in Eq. (18) for S_{xx} and S_{xy} can be analytically carried out for every segment $[p_j, p_{j+1}]$ expanding the velocity over the local rotated basis and using hyperbolic parametrization. The calculation of segment integrals is virtually identical to the large-hexagon case, as described in Appendix C. The only differences are the range of the hyperbolic parameter, $-t_c < t < t_c$ and the opposite direction of integration with respect to parameter t leading to the opposite signs of the integrals $\mathcal{R}_v^{\text{HH}}$ and $\mathcal{G}_{vu}^{\text{HH}}$ in comparison with $\mathcal{R}_u^{\text{LH}}$ and $\mathcal{G}_{vu}^{\text{LH}}$. Therefore the parameter $\eta_{\text{HH}} = \exp(-\int_{p_1}^{p_2} \frac{dp''}{v''} \frac{c}{|e|H\tau})$ is evaluated as

$$\eta_{\text{HH}} = \exp\left(-2t_c/\omega_h\right) \tag{38}$$

with t_c being defined in Eq. (12). The parameter in the exponent $2t_c/\omega_h$ is the ratio of the time to pass one hexagon segment $t_{\text{segm}} = 2ct_c\sqrt{m_u m_v}/|e|H$ to the scattering time τ. Contrary to the case of the large hexagon considered in the Sec. VI, this ratio does not define an additional field scale, since $t_c \sim 1$. The integrals $\mathcal{R}_k^{\text{HH}}$ are evaluated as $\mathcal{R}_v^{\text{HH}} = -p_{u0}G_{cv}$, $\mathcal{R}_u^{\text{HH}} = -p_{v0}G_{cu}$, where the functions G_{cs} are obtained from the functions G_{bs} in Eqs. (24a) and (24b) by replacements $t_b \to t_c$ and $\eta_{\text{LH}} \to \eta_{\text{HH}}$. Correspondingly, the same-segment integrals $\mathcal{G}_{sr}^{\text{HH}}$ are evaluated as $\mathcal{G}_{vv}^{\text{HH}} = p_{u0}^2 K_{cvv}$, $\mathcal{G}_{uu}^{\text{HH}} = p_{v0}^2 K_{cuu}$, and $\mathcal{G}_{vu}^{\text{HH}} = p_{u0}p_{v0}\mathcal{K}_{cvu}$ and the functions K_{csr} are obtained from the functions K_{bsr} in Eqs. (25a), (25b), and (25c) using the same substitutions $t_b \to t_c$ and $\eta_{\text{LH}} \to \eta_{\text{HH}}$. These results yield the following reduced presentation for the HH conductivity slices

$$S_{\alpha\beta}^{\text{HH}} = S_0 F_{\alpha\beta}^{\text{HH}}, \tag{39a}$$

$$F_{xx}^{\text{HH}} = \frac{1}{\omega_h}\left[\mathcal{K}_{cvv} + r_m \mathcal{K}_{cuu} - \frac{\left(\frac{1}{2} - \eta_{\text{HH}}\right)\left(G_{cv}^2 - r_m G_{cu}^2\right) - \sqrt{3r_m}G_{cv}G_{cu}}{1 - \eta_{\text{HH}} + \eta_{\text{HH}}^2}\right], \tag{39b}$$

$$F_{xy}^{\text{HH}} = \frac{1}{\omega_h}\left[-2\sqrt{r_m}\mathcal{K}_{cvu} + \frac{\frac{\sqrt{3}}{2}\left(G_{cv}^2 - G_{cu}^2\right) + 2\left[\frac{1}{2} - \eta_{\text{HH}}\right]G_{cv}G_{cu}}{1 - \eta_{\text{HH}} + \eta_{\text{HH}}^2}\right]. \tag{39c}$$

Here, the reduced magnetic field ω_h and the scale S_0 are defined in Eqs. (23) and (27), respectively, and, also, listed in Table I.

We observe that the shape of the HH magnetoconductivity is entirely determined by the mass ratio r_m, since neither the magnetic-field scale nor the reduced function $F_{\alpha\beta}^{\text{HH}}$ in Eqs. (39b) and (39c) depend on the shift of the Fermi energy with respect the van Hove point ε_{vH}. This means that only the scale of the HH conductivity S_0 depends on the Fermi energy. As a consequence, the p_z integration in Eq. (17) does not change the shape of the HH contribution to the total conductivity. This means that the HH contribution to the conductivity in Eq. (17) has the form similar to Eq. (39a),

$$\sigma_{xx}^{\text{HH}} = \sigma_0^{\text{HH}}F_{xx}^{\text{HH}}(\omega_h, r_m) \tag{40}$$

with

$$\sigma_0^{\text{HH}} = 2e^2 \int \frac{dp_z}{(2\pi)^3} S_0(p_z) = \frac{3e^2\tau}{4\pi^3\hbar^2\sqrt{m_u m_v}} \int dk_z p_{u0}^2. \tag{41}$$

The last formula is written in real units and, in order to make the units more obvious, we assumed that p_{u0} has the dimension of momentum and $k_z = p_z/\hbar$ has the dimension of wave vector. The k_z integration in the last formula is performed over the c-axis extend of the HH pocket. The maximum possible range is determined by the size of the Brillouin zone $2\pi/\mathsf{c}$ set by the c-axis lattice parameter c. For the product $\sigma_0^{\text{HH}}H_0$, we obtain

$$\sigma_0^{\text{HH}}H_0 = \frac{3e^2}{4\pi^3\hbar^2}\frac{c}{|e|}\int dk_z p_{u0}^2. \tag{42}$$

Since the pocket area A_{HH} is proportional to p_{u0}^2, (13a), and the pocket volume $V_{\text{HH}} = \int dk_z A_{\text{HH}}$ determines the total carrier density in the pocket $n_{\text{HH}} = 2V_{\text{HH}}/(2\pi)^3$, the product $\sigma_0^{\text{HH}}H_0$ is proportional to n_{HH},

$$\sigma_0^{\text{HH}}H_0 = \frac{1}{2\pi\sqrt{r_m}t_c}\frac{e^2}{\hbar}\Phi_0 n_{\text{HH}}.$$

We can also note that the ratio of the product $\sigma_0^{HH} H_0$ to the MO frequency $F_{HH} = \frac{c\hbar}{2\pi|e|} A_{HH}$,

$$\frac{\sigma_0^{HH} H_0}{F_{HH}} = \frac{3e^2}{2\pi^2\hbar} \frac{\int dk_z k_{u0}^2}{A_{HH}} \qquad (43)$$

gives the possibility to evaluate the c axis extend of the HH pocket from experimental data and provides a consistency check.

Let us consider the asymptotic behavior of $F_{xx}^{HH}(\omega_h)$. The asymptotic expansions of the reduced functions G_{cs}, K_{css} are the same as for G_{bs}, K_{bss} in Eqs. (C11a), (C11b), (C15), and (C16) with the substitution $t_b \to t_c$. Using these expansions, in the low-field limit $\omega_h \ll 1$, we derive

$$F_{xx}^{HH}(\omega_h) \simeq (r_m - 1)t_c + \frac{r_m + 1}{2} \sinh 2t_c$$
$$- \frac{\omega_h}{2}(\sqrt{3}\sinh t_c + \sqrt{r_m}\cosh t_c)^2. \qquad (44)$$

In particular, the zero-field value can be directly related with the mass ratio as

$$F_{xx}^{HH}(0) = \frac{\sqrt{3r_m}(1 + r_m)}{3r_m - 1} + (r_m - 1)\tanh^{-1}\left(\frac{1}{\sqrt{3r_m}}\right)$$

giving the zero-field HH partial conductivity

$$\sigma_{xx}^{HH}(0) = \frac{3e^2\tau F_{xx}^{HH}(0)}{4\pi^3\hbar^2\sqrt{m_u m_v}} \int dk_z p_{u0}^2.$$

As expected, at low fields the conductivity has linear magnetic-field dependence caused by sharp corners. When CDW gaps are taken into account, the behavior at very small magnetic fields becomes quadratic and then crosses over to a linear dependence at the field scale set by the CDW gap [60]. Deviation from linearity starts at the field $\omega_h \sim 2t_c$ or $H \sim 2c\sqrt{m_u m_v}t_c/e\tau$, at which the time to pass one HH segment becomes comparable with the scattering time.

In the high-field limit $\omega_h \gg 1$, we obtain

$$F_{xx}^{HH}(\omega_h) \simeq \frac{1}{\omega_h^2}\left[-(r_m - 1)t_c + \frac{r_m + 1}{2}\sinh 2t_c\right], \qquad (45)$$

meaning that the HH contribution decays $\propto H^{-2}$ at high fields. The full shape of the field dependence of F_{xx}^{HH} is illustrated in Fig. 6 for $r_m = 1.5$. We see that the initial linear dependence breaks down at field $\omega_h \sim 0.3$ and is followed by the second region of close-to-linear dependence with smaller slope in the range $0.4 \lesssim \omega_h \lesssim 1$. At higher fields, the function $F_{xx}^{HH}(\omega_h)$ approaches the asymptotics in Eq. (45).

The HH contribution to the Hall conductivity is given by $\sigma_{xy}^{HH} = \sigma_0^{HH} F_{xy}^{HH}(\omega_h)$, where the scale σ_0^{HH} is defined in Eq. (41). In the low-field limit, using the asymptotics $\mathcal{K}_{cvu} \simeq -\omega_h^2(t_c - \omega_h)$, for $\omega_h \to 0$, we obtain

$$F_{xy}^{HH} \simeq \omega_h\left[2\sqrt{r_m}t_c - \frac{\sqrt{3}}{2}(r_m + 1)\right]. \qquad (46)$$

The linear Hall coefficient is negative corresponding to electron pocket. The slice contribution to the linear Hall
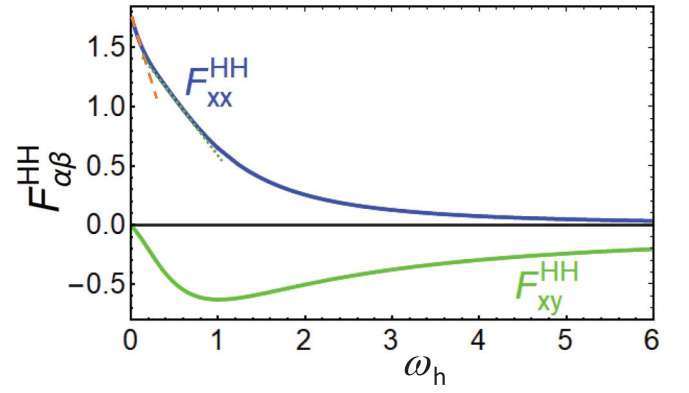

FIG. 6. The field dependences of reduced functions, F_{xx}^{HH} and F_{xy}^{HH}, following from Eqs. (39b) and (39c) computed using $r_m = 1.5$. These functions determine shapes of the HH contributions to the diagonal and Hall conductivities. The orange dashed and green dotted lines mark initial linear drop and further quasilinear decrease of F_{xx}^{HH}.

conductivity is given by

$$S_{xy}^{HH} = 6\frac{|e|H}{c}\tau^2 v_{u0} v_{v0}\left[t_c - \frac{\sqrt{3}}{4}\frac{r_m + 1}{\sqrt{r_m}}\right]. \qquad (47)$$

The velocity contour determining the sign and magnitude of the linear Hall term in Eq. (33) is shown in the inset of Fig. 7(a). We can see that the HH velocity contour is composed of small and smooth hyperbolic branches connected by relatively long straight lines corresponding to velocity jumps at the corners. An interesting observation is that the presence of velocity discontinuities on the Fermi surface does not invalidate the construction and Eq. (33) remains valid. The dominating contribution to the velocity area A_v is coming from the regular electronic hexagon in the center.
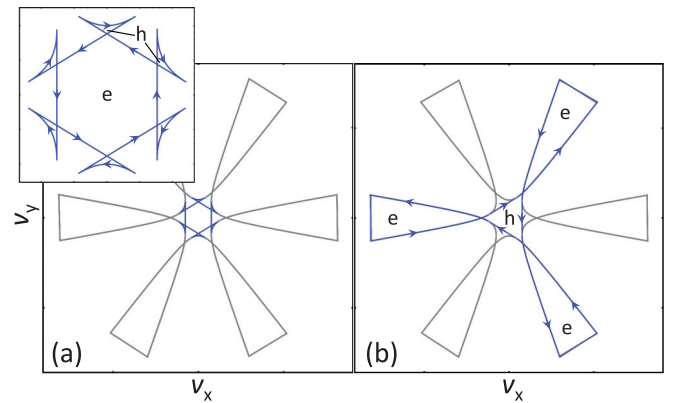

FIG. 7. The velocity contours for the reconstructed Fermi pockets for $r_m = 1.5$ and $\kappa = 20$: (a) hyperbolic hexagon and (b) one of the triangular pockets. These contours define velocity areas A_v which determines the linear Hall term at small magnetic fields according to Eq. (33). The main plot in (a) shows the HH velocity contour with respect to the large hexagon while the inset shows this contour in larger scale.

In the high-field limit, using the asymptotics $\mathcal{K}_{cvu} \simeq -(1/2)[\sinh(2t_c) - 2t_c]$, for $\omega_h \gg 1$, we find

$$F_{xy}^{\text{HH}} \simeq -\frac{2\sqrt{r_m}}{\omega_h} t_c \tag{48}$$

This corresponds to universal relation between the conductivity slice and cross section area A_{HH} in Eq. (13a), $S_{xy}^{\text{HH}} = -A_{\text{HH}}/(|e|H/c)$, which is similar to Eq. (36). Correspondingly, σ_{xy}^{HH} is connected with quasiparticle density inside the pocket by a simple relation [64]

$$\sigma_{xy}^{\text{HH}} = -\frac{e^2}{\pi \hbar} \frac{\Phi_0 n_{\text{HH}}}{H}. \tag{49}$$

The full field dependence of F_{xy}^{HH} is illustrated in Fig. 6 for $r_m = 1.5$. This function remains negative for the whole field range, corresponding to an electron pocket. Its absolute value reaches maximum $|F_{xy}^{\text{HH}}| \approx 0.64$ at $\omega_h \approx 1$ and it exceeds F_{xx}^{HH} roughly at the same field.

B. Triangular pockets

In this section, we evaluate conductivity slices for the triangular pockets described in Sec. IV and illustrated in Figs. 3(c) and 4. Using the general results for m-fold symmetric 2D slices in Eqs. (19a) and (19b), we can write the conductivity slices for a triangular pocket, $m = 3$, as

$$S_{xx}^{\text{T}} = \frac{3}{2} \frac{c}{|e|H} \left\{ \mathcal{G}_{tt}^{\text{T}} + \mathcal{G}_{ll}^{\text{T}} - \text{Re}\left[\frac{(\mathcal{R}_t^{\text{T}} + \iota \mathcal{R}_l^{\text{T}})^2}{\exp\left(-\iota \frac{2\pi}{3}\right) - \eta_T} \right] \right\}, \tag{50a}$$

$$S_{xy}^{\text{T}} = -\frac{3}{2} \frac{c}{|e|H} \left\{ \mathcal{G}_{lt}^{\text{T}} - \mathcal{G}_{tl}^{\text{T}} + \text{Im}\left[\frac{(\mathcal{R}_t^{\text{T}} + \iota \mathcal{R}_l^{\text{T}})^2}{\exp\left(-\iota \frac{2\pi}{3}\right) - \eta_T} \right] \right\}, \tag{50b}$$

where the parameter $\eta_T = \exp(-\mathcal{Q}_T)$ and segment integrals $\mathcal{R}_s^{\text{T}}$ and $\mathcal{G}_{sr}^{\text{T}}$ are defined similar to Eqs. (20a)–(20c). Contrary to the hexagon pockets, the indices $s, r = l, t$ corresponding to the longitudinal and transverse components of velocity do not coincide with the hyperbolic indices u and v, see Fig. 4. The calculations described in Appendix D lead to the following presentation for the conductivity slices for one triangular pocket,

$$S_{\alpha\beta}^{\text{T}} = \frac{S_0}{2} F_{\alpha\beta}^{\text{T}}, \tag{51a}$$

$$F_{xx}^{\text{T}} = \frac{1}{\omega_h} \left\{ 2\mathcal{K}_{vv}(t_b, t_c) + 2r_m \mathcal{K}_{uu}(t_b, t_c) \right.$$
$$\left. - \text{Re}\left[\frac{\exp\left(-\iota \frac{\pi}{3}\right)\left(\mathcal{G}_{bc}^2 + \mathcal{G}_{cb}^2\right) + 2\sqrt{\eta_T}\mathcal{G}_{bc}\mathcal{G}_{cb}}{\exp\left(-\iota \frac{2\pi}{3}\right) - \eta_T} \right] \right\}, \tag{51b}$$

$$F_{xy}^{\text{T}} = -\frac{1}{\omega_h} \left\{ 2\sqrt{r_m}[\mathcal{K}_{vu}(t_b, t_c) + \mathcal{K}_{vu}(-t_c, -t_b)] \right.$$
$$\left. + \text{Im}\left[\frac{\exp\left(-\iota \frac{\pi}{3}\right)\left(\mathcal{G}_{bc}^2 + \mathcal{G}_{cb}^2\right) + 2\sqrt{\eta_T}\mathcal{G}_{bc}\mathcal{G}_{cb}}{\exp\left(-\iota \frac{2\pi}{3}\right) - \eta_T} \right] \right\}. \tag{51c}$$

Here the hyperbolic limits t_b and t_c are defined in Eqs. (10) and (12), respectively, see also Table I,

$$\eta_T = \exp\left[-\frac{2(t_b - t_c)}{\omega_h} \right], \tag{52}$$

$\mathcal{G}_{bc}$ and $\mathcal{G}_{cb}$ are the complex functions defined as

$$\mathcal{G}_{bc} = G_{bcv} - \iota \sqrt{r_m}G_{bcu}, \qquad \mathcal{G}_{cb} = G_{cbv} - \iota \sqrt{r_m}G_{cbu}, \tag{53}$$

where the functions G_{bck} and G_{cbk} with $k = u, v$ are given by

$$G_{bck} = G_k(t_b, t_c), \qquad G_{cbk} = G_k(-t_c, -t_b), \tag{54}$$

with

$$G_v(t_2, t_1) = \frac{\left(\cosh t_2 + \frac{1}{\omega_h}\sinh t_2\right)\exp\left(-\frac{t_2-t_1}{\omega_h}\right) - \left(\cosh t_1 + \frac{1}{\omega_h}\sinh t_1\right)}{1 - \omega_h^{-2}}, \tag{55a}$$

$$G_u(t_2, t_1) = \frac{\left(\sinh t_2 + \frac{1}{\omega_h}\cosh t_2\right)\exp\left(-\frac{t_2-t_1}{\omega_h}\right) - \left(\sinh t_1 + \frac{1}{\omega_h}\cosh t_1\right)}{1 - \omega_h^{-2}}, \tag{55b}$$

see Appendix C for details. The functions $\mathcal{K}_{ss}(t_b, t_c)$ in the first line of Eq. (51b) determining the same-segment contributions to S_{xx}^{T} are evaluated in Appendix D as

$$\mathcal{K}_{vv}(t_b, t_c) = \frac{1}{1 - \omega_h^{-2}}\left[-\left(\cosh t_b + \frac{1}{\omega_h}\sinh t_b\right)G_{cbv} - \frac{\cosh(2t_b) - \cosh(2t_c)}{4} - \frac{\sinh(2t_b) - \sinh(2t_c) - 2(t_b - t_c)}{4\omega_h} \right], \tag{56a}$$

$$\mathcal{K}_{uu}(t_b, t_c) = \frac{1}{1 - \omega_h^{-2}}\left[\left(\sinh t_b + \frac{1}{\omega_h}\cosh t_b\right)G_{cbu} - \frac{\cosh(2t_b) - \cosh(2t_c)}{4} - \frac{\sinh(2t_b) - \sinh(2t_c) + 2(t_b - t_c)}{4\omega_h} \right], \tag{56b}$$

and the off-diagonal function $\mathcal{K}_{vu}(t_b, t_c)$ in the first line of the Hall term in Eq. (51c) is given by

$$\mathcal{K}_{vu}(t_b, t_c) = \frac{1}{1-\omega_h^{-2}} \left[\frac{\frac{1}{\omega_h} - \exp\left(-\frac{t_b - t_c}{\omega_h}\right)\left(\sinh t_b + \frac{1}{\omega_h}\cosh t_b\right)\left(\cosh t_c - \frac{1}{\omega_h}\sinh t_c\right)}{1-\omega_h^{-2}} \right.$$
$$\left. + \frac{\sinh(2t_b) + \sinh(2t_c)}{4} + \frac{t_b - t_c}{2} - \frac{\cosh(2t_b) - \cosh(2t_c)}{4\omega_h} \right]. \tag{57}$$

Two features strongly influence the shape of magnetoconductivity components. The first feature are sharp corners related to FS reconstruction. The second feature is related to proximity of these corners to van Hove singularities. As a consequence, the Fermi velocity reduces on approaching the corners. In fact, the velocity at the corner is only slightly larger than the minimum velocity of the HH pocket v_{u0}. The consequences of this velocity reduction are similar to those for the large hexagon, discussed in Sec. VI. For example, the Hall conductivity for the triangular pocket is negative at small magnetic fields in spite of its hole nature but it has strong field dependence and changes sign.

Let us discuss now the asymptotic behavior of the conductivity components for the triangular pockets. We start with the diagonal component. For small fields, $\omega_h \ll 1$, using asymptotics of the functions G_{bck}, G_{cbk}, $\mathcal{K}_{kk}(t_b, t_c)$ listed in Appendix D, Eqs. (D6), (D7),(D13), and (D14), we obtain the zero-field result

$$F_{xx}^{T}(0) = \tfrac{1}{2}\{(r_m + 1)[\sinh(2t_b) - \sinh(2t_c)] \\ + 2(r_m - 1)(t_b - t_c)\} \tag{58}$$

and the linear term

$$F_{xx}^{T}(\omega_h) - F_{xx}^{T}(0) \simeq -\frac{\omega_h}{2}[(\sqrt{3}\sinh t_c + \sqrt{r_m}\cosh t_c)^2 \\ + (\sqrt{3}\sinh t_b - \sqrt{r_m}\cosh t_b)^2]. \tag{59}$$

Here the first term is caused by the sharp corners of triangles. It is identical with the linear term for the hyperbolic hexagon in Eq. (44). The second term appears due to velocity jumps at the matching point between incoming and outgoing branches and is artifact of the model approximations.

As in the case of the large hexagon, the field dependence of the triangular pockets is characterized by the two field scales corresponding to $\omega_h \sim 1$ and $\omega_h \sim t_b - t_c$. The upper scale is somewhat smaller than the one for the large hexagon. In the limit $\omega_h \gg 1$, using high-field limits in Eqs. (D8),(D9), (D16), and (D17), we obtain a remarkably simple approximate result

for the diagonal term, similar to Eq. (29),

$$F_{xx}^{T} \simeq \frac{\kappa^2}{2\omega_h} \frac{1 - \eta_T^2}{1 + \eta_T + \eta_T^2}, \tag{60}$$

which also describes crossover between $1/H$ and $1/H^2$ decays of diagonal conductivity at $\omega_h \sim 2(t_b - t_c)$. At highest fields, for $\omega_h \gg 2(t_b - t_c)$, we have $F_{xx}^{T} \simeq 2\kappa^2(t_b - t_c)/(3\omega_h^2)$. This is roughly three times smaller than the corresponding asymptotic limit for the large hexagon.

Let us consider the asymptotic limits of the Hall component F_{xy}^{T} in Eq. (51c). Using asymptotic limits of the functions G_{bck}, G_{cbk}, $\mathcal{K}_{uv}(t_b, t_c)$ for $\omega_h \ll 1$ presented in Eqs. (D6), (D7), and (D15), we obtain the linear term at small fields

$$F_{xy}^{T} = -\omega_h\left[\frac{1}{2}(\sqrt{3}\sinh t_b - \sqrt{r_m}\cosh t_b) \right. \\ \times (\sinh t_b + \sqrt{3 r_m}\cosh t_b) - 2\sqrt{r_m}(t_b - t_c) \\ \left. - \frac{\sqrt{3}}{2}(r_m + 1)\right]. \tag{61}$$

As in the case of the large hexagon pocket, Eq. (31), the sign of this term is *negative* even though the triangles are nominally hole-type pockets. The reason for this behavior is also very similar to the case of large hexagon. The triangular pockets have regions with both positive and negative curvature. In this context, the sharp corners should be considered as the regions with extreme positive curvature. However, these corners are located very close to van Hove points where velocities are small and, as a consequence, they give small contribution to the Hall term. The dominating negative contribution is coming from far away regions with negative curvature. This is illustrated by the velocity contour shown in Fig. 7(b). Velocity jumps at the corners from the small triangle at the center. The area of this triangle contributes to the total velocity area A_v in Eq. (32) with positive sign. The larger areas of three outside "blades" contribute to A_v with negative sign yielding the net negative velocity contour area.

At higher field, $\omega_h \gg 1$, using Eqs. (D8), (D9), and (D18), we derive the following approximate result

$$F_{xy}^{T} \simeq -\frac{1}{\omega_h}\left[\frac{\kappa}{2}\left(\sqrt{3}\cosh t_b - \sqrt{r_m}\sinh t_b - \frac{\sqrt{3}\eta_T \kappa}{1 + \eta_T + \eta_T^2}\right) + 2\sqrt{r_m}(t_b - t_c)\right] \simeq -\frac{\kappa^2}{2\omega_h}\left(\frac{\sqrt{3} - \sqrt{r_m}}{1 + \sqrt{3 r_m}} - \frac{\sqrt{3}\eta_T}{1 + \eta_T + \eta_T^2}\right). \tag{62}$$

It describes the crossover between the two $1/\omega_h$ dependences

$$F_{xy}^{T} \simeq \frac{\kappa^2}{2(\sqrt{3 r_m} + 1)\omega_h} \times \begin{cases} -(\sqrt{3} - \sqrt{r_m}), & \text{for } 1 \ll \omega_h \ll 2(t_b - t_c) \\ \frac{2\sqrt{3}}{3}(\sqrt{3 r_m} - 1), & \text{for } \omega_h \gg 2(t_b - t_c) \end{cases}, \tag{63}$$

which have opposite signs, similar to the large-hexagon pocket in Eq. (35). The large-field asymptotic reproduces a universal relation between the Hall conductivity slice and the triangle area A_T in Eq. (15), $S_{xy}^T = \frac{A_T}{|e|H/c}$. Since the total area of two triangles is more than two times smaller than the area of the large hexagon, the Hall conductivity at high fields is also smaller by the same factor.

VIII. MODIFICATION OF MAGNETOCONDUCTIVITY BY FERMI-SURFACE RECONSTRUCTION DUE TO CDW ORDER

As we have now the full analytical results for the conductivity slices for all pockets in the reconstructed Fermi surface, we can analyze them and compare with the behavior of the original large-hexagon pocket. The total magnetoconductivity slice of the reconstructed Fermi surface composed of hyperbolic hexagon and two triangular pockets is given by

$$S_{\alpha\beta}^R(\omega_h) = S_{\alpha\beta}^{HH}(\omega_h) + 2S_{\alpha\beta}^T(\omega_h) = S_0 F_{\alpha\beta}^R(\omega_h), \quad (64a)$$

$$F_{\alpha\beta}^R(\omega_h) = F_{\alpha\beta}^{HH}(\omega_h) + F_{\alpha\beta}^T(\omega_h). \quad (64b)$$

Since we neglected corner rounding by the CDW order, the total zero-field conductivity for the reconstructed FS,

$$F_{xx}^R(0) = F_{xx}^{HH}(0) + F_{xx}^T(0) = \frac{r_m + 1}{2} \sinh(2t_b) + (r_m - 1)t_b \quad (65)$$

coincides with zero-field conductivity for the large hexagon pocket, see Eq. (28). In reality, there is a small correction caused by the Fermi-surface reconstruction by finite CDW gap. The total linear term in the conductivity slice is given by

$$F_{xx}^R(\omega_h) - F_{xx}^R(0) \simeq -\omega_h \left[(\sqrt{3}\sinh t_c + \sqrt{r_m}\cosh t_c)^2 + \frac{1}{2}(\sqrt{3}\sinh t_b - \sqrt{r_m}\cosh t_b)^2 \right]. \quad (66)$$

Here the first term in the square brackets is caused by the sharp corners of the reconstructed FS pockets. The HH pocket and the two triangles give equal contributions to this term in spite of the overall small contribution of the HH pocket. Note that this term only depends on the mass ratio r_m and, using the definition of t_c in Eq. (12), can be computed as $(\sqrt{3}\sinh t_c + \sqrt{r_m}\cosh t_c)^2 = 3(1 + r_m)^2/(3r_m - 1)$. The second term is identical to the large-hexagon pocket in Eq. (28) and appears due to the small velocity jumps at the matching points between the hyperbolic branches.

The full field dependence of the function $F_{xx}^R(\omega_h)$ is compared with the corresponding function $F_{xx}^{LH}(\omega_h)$ for representative parameters $r_m = 1.5$ and $\kappa = 10$ in the lower panel of Fig. 8. We can see that $F_{xx}^R(\omega_h)$ has a sharper drop than $F_{xx}^{LH}(\omega_h)$ with pronounced linear dependence at small fields. This means that the reconstruction of the Fermi surface by the 3Q CDW order significantly enhances small-field magnetoconductivity, in agreement with experiment.

Let us compare now the behavior of the Hall component for original and reconstructed Fermi surfaces. The total linear
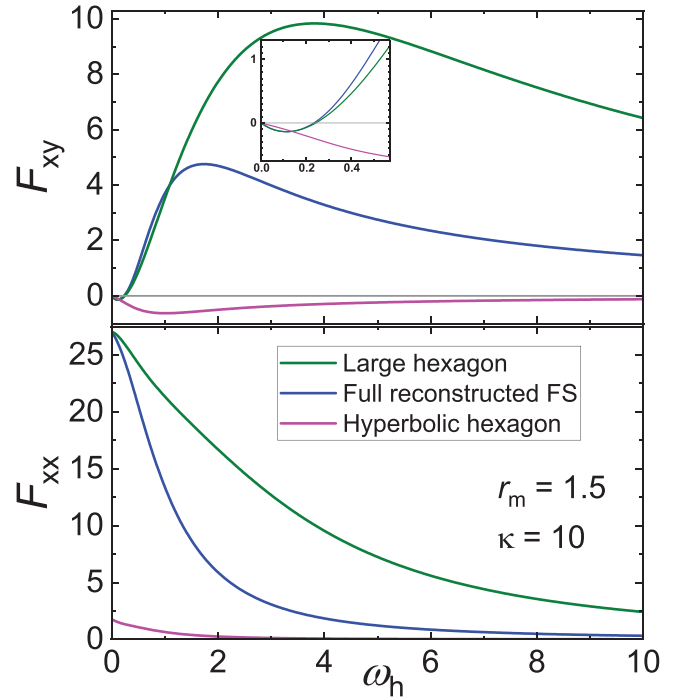

FIG. 8. The shapes of the field dependences of the reduced functions $F_{\alpha\beta}$ determining the conductivity components for the large hexagon and reconstructed pockets. The functions are computed for the representative parameters $r_m = 1.5$ and $\kappa = 10$. The inset in the upper panel zooms into the nonmonotonic low-field behavior of F_{xy}.

term at small fields

$$F_{xy}^R = -\omega_h \left[\frac{1}{2}(\sqrt{3}\sinh t_b - \sqrt{r_m}\cosh t_b) \right. $$
$$\left. \times (\sinh t_b + \sqrt{3r_m}\cosh t_b) - 2\sqrt{r_m}t_b \right] \quad (67)$$

is negative and coincides with the linear term for the large hexagon pocket in Eq. (31). On the other hand, at high magnetic fields, $\omega_h \gg 2(t_b - t_c)$, the dominating contribution to total Hall conductivity is coming from the triangular pockets, Eq. (63). It is positive, decays as $1/\omega_h$, and is more than two times smaller than the Hall conductivity for large hexagon pocket in Eq. (35).

The full field dependences of the Hall components for original and reconstructed Fermi surfaces are illustrated in the upper panel of Fig. 8. We see that the shape of the field dependence remains anomalous after the FS reconstruction. Namely, the function $F_{xy}^R(\omega_h)$ is still nonmonotonic and changes sign. In fact, the reconstruction has a very weak influence on the low-field behavior. The most essential difference is that the conductivity values at the maximum and above become significantly smaller. We also note that even though the hyperbolic hexagon has an overall small contribution, it strongly affects the linear slope at small fields, see the inset in the upper panel of Fig. 8.

To avoid a possible confusion, we note that Fig. 8 compares the behavior of the conductivity slices for original and reconstructed Fermi surfaces in the reduced form. In reality, these Fermi surfaces are realized in different temperature

ranges, above and below the CDW transition temperature. In particular, strong difference in scattering rates leads to strong difference between the scales S_0 and H_0 in these temperature ranges.

IX. ROLE OF CORNER ROUNDING BY FINITE CDW GAP IN LOW-MAGNETIC-FIELD BEHAVIOR

So far, we considered the approximation of sharp corners at the branch crossing. A finite CDW gap rounds these corners. If the CDW gap is small in comparison with other energy scales, these roundings only modify the behavior of the magnetoconductivity at low magnetic fields. The corners emerge because band folding by the CDW wave vectors generates crossing quasiparticle branches. The CDW hybridization transforms the quasiparticle spectrum for two crossing branches $\xi_1(\boldsymbol{p})$ and $\xi_2(\boldsymbol{p})$ as

$$E_{\mathbf{p},\pm} = \frac{\xi_+}{2} \pm \sqrt{\frac{\xi_-^2}{4} + \Delta_{\mathrm{CDW}}^2}, \tag{68}$$

where $\xi_\pm = \xi_1(\boldsymbol{p}) \pm \xi_2(\boldsymbol{p})$ and Δ_{CDW} is the CDW gap parameter. Here we assume that the branches cross at $\boldsymbol{p} = \boldsymbol{p}_c$, $\xi_1(\boldsymbol{p}_c) = \xi_2(\boldsymbol{p}_c)$. At this point, the gap in the quasiparticle spectrum opens equal to Δ_{CDW}. The spectral gap, however, is only finite in a small region of the Fermi surface near $\boldsymbol{p}_c$. The band splitting by CDW order has been directly observed by ARPES [26,32,33]. The CDW hybridization rounds the corners at the crossing converting them to high-curvature turning points.

With the rounded corners, the asymptotics of magnetoconductivity for $H \to 0$ is quadratic $\sigma_{xx}(H) - \sigma_{xx}(0) \propto H^2$ and crosses over to a linear dependence at the magnetic field scale proportional to Δ_{CDW}. The quantitative theoretical description of this crossover has been elaborated in Ref. [60]. The correction to the conductivity slice due to the reconstructed crossing points can be represented as

$$S_{xx}^{(\mathrm{cr})}(H) - S_{xx}(0) = \frac{2n_{\mathrm{cr}}\langle v_{-,x}^2\rangle\tau\,\Delta_{\mathrm{CDW}}}{[\mathbf{v}_1 \times \mathbf{v}_2]_z} G(H/H_\Delta), \tag{69}$$

where n_{cr} is the total number of crossing points (6 in our case), $\mathbf{v}_1$ and $\mathbf{v}_2$ are the velocities of the two branches at the crossing, $v_{-,x} = v_{2,x} - v_{1,x}$ is the jump of the x component of the velocity at the corner for $\Delta_{\mathrm{CDW}} = 0$, $\langle\ldots\rangle$ means averaging over crossings, and

$$H_\Delta = \frac{2c\Delta_{\mathrm{CDW}}}{e\tau[\mathbf{v}_1 \times \mathbf{v}_2]_z} \tag{70}$$

is the magnetic field scale set by the CDW gap Δ_{CDW}. The reduced function $G(h)$ is defined by the integral

$$G(h) = \int_0^\infty dx \int_0^\infty dy \exp(-y)$$
$$\times \left(\frac{x^2 - h^2 y^2/4}{\sqrt{\left(x + h\frac{y}{2}\right)^2 + 1}\sqrt{\left(x - h\frac{y}{2}\right)^2 + 1}} - \frac{x^2}{x^2 + 1} \right) \tag{71}$$

and has the following asymptotics:

$$G(h) = \begin{cases} -\frac{3\pi}{16}h^2 & \text{for } h \ll 1 \\ \frac{\pi}{2} - h & \text{for } h \gg 1 \end{cases}. \tag{72}$$

We find an accurate approximation for this function in the form of superposition of two hyperbolas

$$G(h) \approx \frac{\pi}{2} - f\sqrt{a_1^2 + h^2} - (1 - f)\sqrt{a_2^2 + h^2} \tag{73}$$

with $f = 0.8035$, $a_1 = 0.705$, and $a_2 = 5.112$. This form is more convenient for modeling of the data than the exact integral presentation in Eq. (71).

In the region $H \gg H_\Delta$, Eqs. (69) and (71) give linear magnetoconductivity

$$S_{xx}^{(\mathrm{cr})}(H) - S_{xx}(0) \approx -n_{\mathrm{cr}}\langle v_{-,x}^2\rangle\frac{eH\tau^2}{c}. \tag{74}$$

For the spectrum considered in this paper, we evaluate

$$\langle v_{-,x}^2\rangle = \frac{v_{v0}^2}{2}(\sqrt{3}\sinh t_c + \sqrt{r_m}\cosh t_c)^2. \tag{75}$$

With this result, we can demonstrate that Eq. (74) reproduces Eq. (64a) when we substitute the first term in Eq. (66) describing the contribution from the sharp corners. Also, the z component of the velocity cross product in Eqs. (69) and (70) in our case can be evaluated as

$$[\mathbf{v}_1 \times \mathbf{v}_2]_z = \frac{\sqrt{3}}{2}v_{v0}^2\frac{3r_m^2 + 1}{3r_m - 1}. \tag{76}$$

It is instructive to compare the CDW field scale H_Δ in Eq. (70) with the field scale H_0 listed in the Table I. Using Eq. (76), we obtain for the ratio of these two scales

$$\frac{H_\Delta}{H_0} = \frac{2\Delta_{\mathrm{CDW}}}{\sqrt{m_u m_v}[\mathbf{v}_1 \times \mathbf{v}_2]_l} = C_m\frac{\Delta_{\mathrm{CDW}}}{\varepsilon_{\mathrm{vH}}} \tag{77}$$

with $C_m = 2\sqrt{r_m/3}(3r_m - 1)/(3r_m^2 + 1)$. We see that, up to a numerical factor, this ratio is given by the ratio of the CDW gap and the distance between the van Hove energy and the Fermi level $\varepsilon_{\mathrm{vH}}$.

X. EXPERIMENTAL DATA AND QUALITATIVE MODELING

Single crystals of CsV_3Sb_5 were grown using the flux method as described in our earlier works [35,39]. Our crystals have been extensively characterized by x-ray diffraction, energy dispersive spectroscopy, bulk magnetization, magnetic torque, and tunnel diode oscillator techniques [35,39]. In this work, we focus on electrical transport. The electrical resistivity and magnetotransport measurements were performed using a *dc* technique in a Physical Properties Measurement System (DynaCool-PPMS, Quantum Design) following a standard four-probe method with current applied along the *ab* plane and field along the *c*-axis. For the transverse magnetoresistance (*MR*) and Hall resistivity, measurements were carried out for both positive and negative field directions to correct for misalignment of electrical contacts. A typical temperature dependence of the in-plane electrical resistivity $\rho_{xx}(T)$ of CsV_3Sb_5 single crystal is shown in Fig. 9. The $\rho_{xx}(T)$ exhibits a metallic behavior and displays two anomalies, one
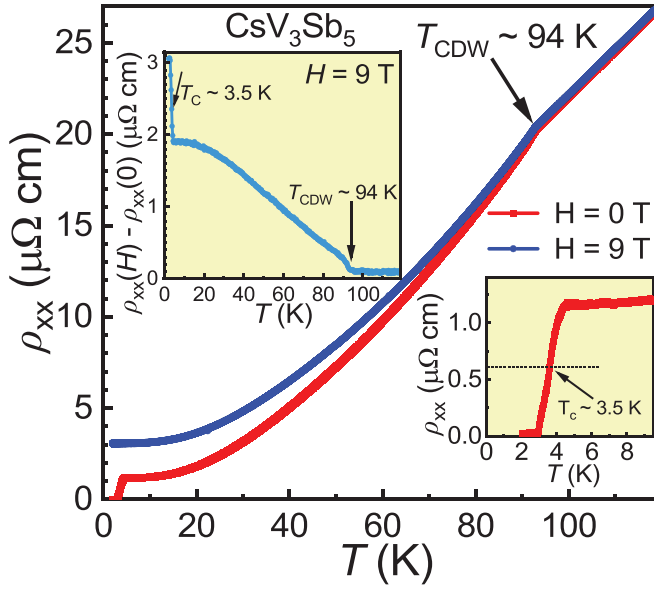
FIG. 9. Temperature dependence of the longitudinal electrical resistivity $\rho_{xx}(T)$ of CsV$_3$Sb$_5$ displaying the CDW transition at $T_{CDW} \approx$ 94 K and the superconducting transition at $T_c \approx 3.5$ K (defined as the midpoint of the transition, see the lower right inset). Red curve is for $H = 0$ T and blue curve is for $H = 9$ T. (Upper left inset) The difference between zero-field data and data at 9 T presented in main frame.

at $T_{CDW} \sim 94$ K arising due to charge density wave ordering and another transition at $T_c \sim 3.5$ K corresponding to superconductivity, as presented in the lower right inset of Fig. 9 (red curve). The CDW transition is seen as a kink in the $\rho_{xx}(T)$ curve and below the transition the resistivity is reduced. This most likely indicates the reduction of the scattering rate in the ordered state. These observations are consistent with previous reports [34,37,51]. The samples display a low residual resistivity ~ 1.2 μΩ cm at ~ 4 K before entering the superconducting state, reflecting their high quality.

Below ~ 94 K, there is a considerable *MR*, as shown in Fig. 9 (9 T, blue curve). In the upper left inset of Fig. 9, we plot the difference between zero field data and the data at 9 T. Interestingly, the *MR* is sharply enhanced below the CDW transition at 94 K. This enhancement can be mostly attributed to the formation of the sharp corners in the reconstructed FS, as discussed in Sec. VIII. Also, *MR* is enhanced due to the reduction of the scattering rate in the ordered state.

Figures 10(a) and 10(b) show the magnetoresistance and Hall resistivity of CsV$_3$Sb$_5$ at various temperatures, respectively. The magnitude and shape of magnetoresistance [$\rho_{xx}(H)$] and Hall resistivity [$\rho_{yx}(H)$] observed in our single crystals are similar to that reported in previous studies [16,34,37,51]. In addition to large magnetoresistance MR$_{xx}$ = [$\rho_{xx}(H) - \rho_{xx}(0)$]/$\rho_{xx}(0)$, we observed clear Shubnikov-de Haas quantum oscillations (QOs) at low temperatures. Figure 10(c) displays MR$_{xx}$ at 10 K, where the QOs are apparent above 5 T as seen more clearly in the background-subtracted data in the inset. The observation of QOs at low temperatures indicates a small scattering rate due to impurities in our samples which is also a prerequisite for the emergence of the anomalous features in the magnetotransport we are aiming to understand.

As established by the DFT calculations [16,27,34,40,43], ARPES measurements [25–33], and magnetic oscillations data [16,34–39], kagome superconductors AV$_3$Sb$_5$ are multiple-band materials with Fermi surfaces composed of multiple sheets. We can hardly expect to quantitatively describe the magnetotransport of a material with such complex band structure by taking into account contribution from only one pocket, even if it has distinct anomalous behavior. In addition, we evaluated the contribution from one k_z slice, and the total conductivity is obtained by integration over k_z accounting for the k_z dependence of the band parameters. A full microscopic calculation of the magnetoconductivity does not appear feasible. Therefore we aim at a qualitative modeling of the experimental data assuming that (i) all bands except the ones originating from the large hexagon pocket give a smooth background contribution and (ii) averaging over k_z can be
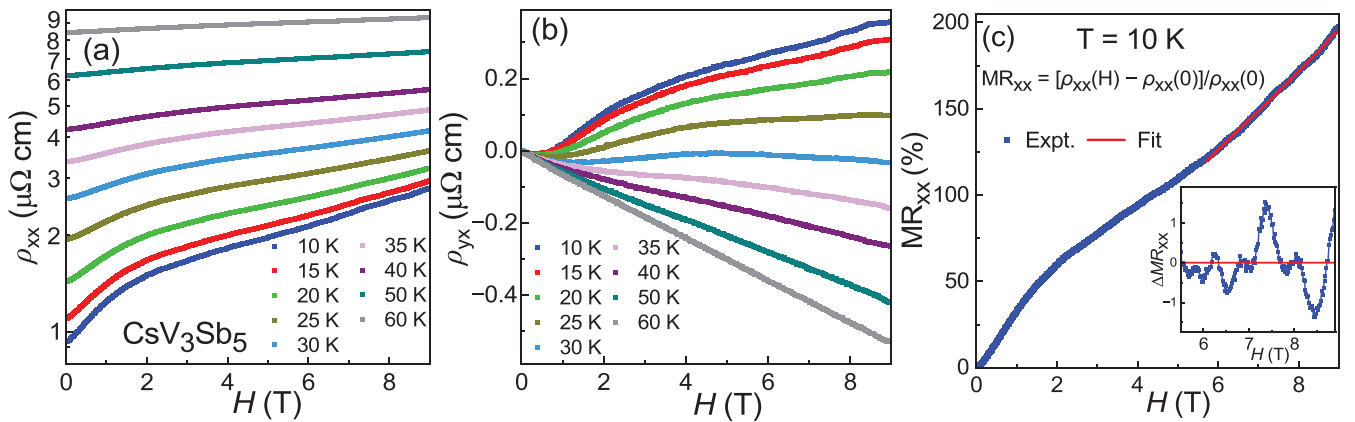

FIG. 10. Magnetic-field dependences of the diagonal (a) and Hall resistivity (b) of CsV$_3$Sb$_5$ at indicated temperatures. These data are used to evaluate the diagonal and Hall conductivities presented in Figs. 1 and 11. (c) shows the diagonal magnetoresistance MR$_{xx}$ at 10 K (blue dots). Red curve shows the third-order polynomial fit for the smooth background. (Inset) Magnetoresistance above 5 T after background subtraction (ΔMR$_{xx}$). In addition to the anomalous magnetoresistance (described in the text), there are clear Shubnikov-de Haas quantum oscillations above 5 T in the background-subtracted data affirming the high quality of the sample.
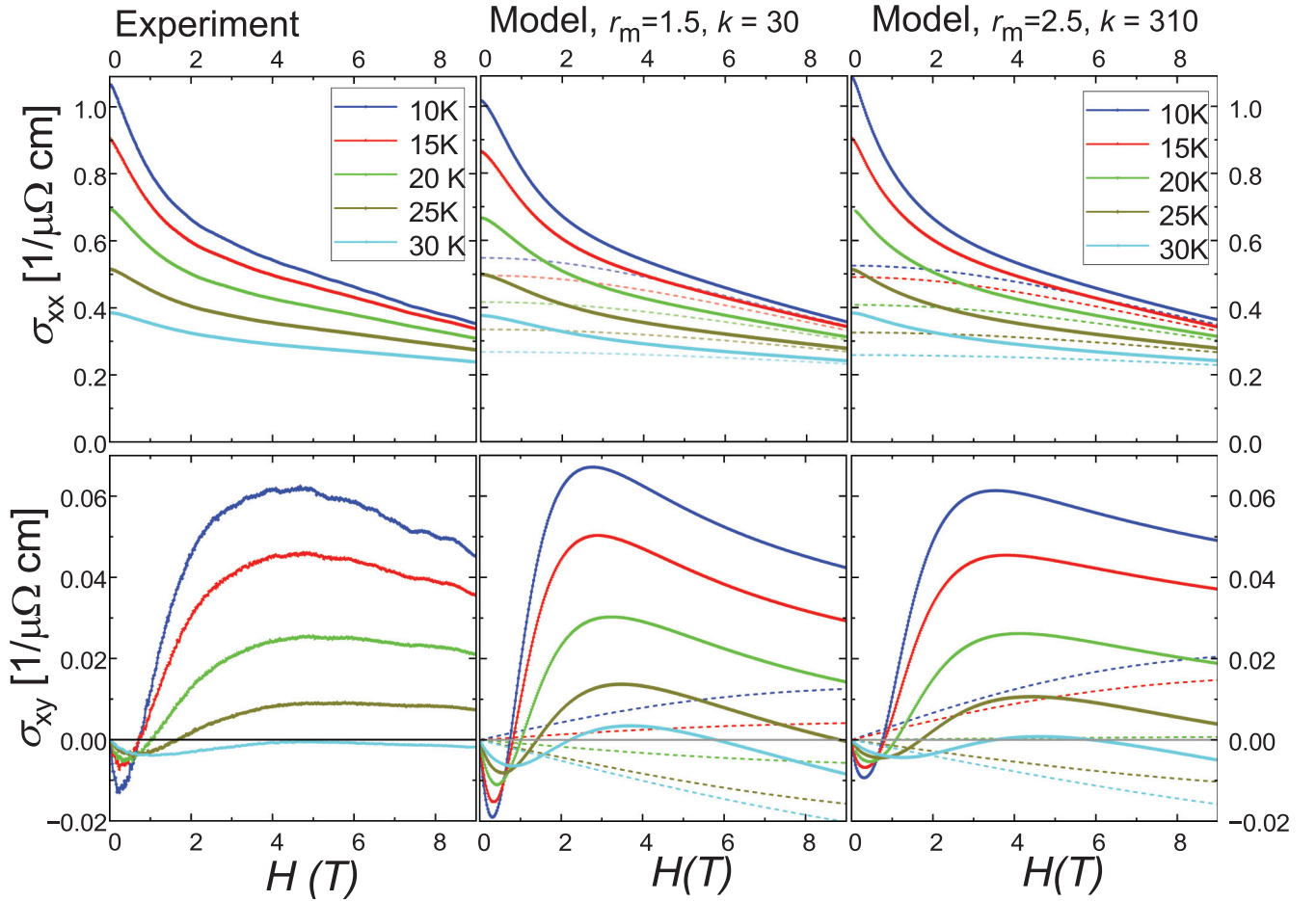
FIG. 11. (Left) Experimental field dependences of the diagonal and Hall conductivities for CsV_3Sb_5 at five different temperatures. Modeling of these data using Eqs. (79), (80), (81a), and (81b) with two sets of band parameters in Eq. (80), $r_m = 1.5$ and $\kappa = 30$ (middle) and $r_m = 2.5$ and $\kappa = 310$ (right). The second set looks less reasonable but gives better fits. The dashed lines show fitted background contributions.

approximately replaced by taking parameters from a typical k_z slice, i.e., we approximate Eq. (17) for the anomalous part dominated by van Hove singularities as

$$\sigma_{\alpha\beta}^{\text{vH}} \approx 2e^2 \frac{p_{z0}}{(2\pi)^3} \bar{S}_{\alpha\beta}, \tag{78}$$

where p_{z0} is the size of the large hexagon in the c-axis direction. and $\bar{S}_{\alpha\beta} = S_0 F_{\alpha\beta}^R(H/H_0, \bar{\kappa}, r_m)$ is the typical slice contribution with the parameter $\bar{\kappa}$ being the typical value of the ratio K/p_{u0}, see Eq. (64a). The maximum value of p_{z0} is obviously given by the size of the Brillouin zone $K_z = 2\pi/c$. Therefore we try to model the experimental magnetoconductivity data with the following ansatz

$$\sigma_{\alpha\beta}(H) = \sigma_{\alpha\beta}^{\text{vH}}(H) + \sigma_{\alpha\beta}^{\text{bg}}(H), \tag{79}$$

where $\sigma_{\alpha\beta}^{\text{vH}}(H)$ is the anomalous magnetoconductivity due to reconstructed FSs computed in the previous sections, which we approximate as

$$\sigma_{\alpha\beta}^{\text{vH}}(H) = \sigma_0^{\text{vH}} \kappa^{-2} F_{\alpha\beta}^R(H/H_0, \kappa, r_m) \tag{80}$$

and $\sigma_{\alpha\beta}^{\text{bg}}(H)$ is the background contribution from all other bands for which we assume simple Drude shapes

$$\sigma_{xx}^{\text{bg}}(H) = \frac{\sigma_{0xx}^{\text{bg}}}{1 + (H/H_{\text{bg}})^2}, \tag{81a}$$

$$\sigma_{xy}^{\text{bg}}(H) = \frac{\sigma_{0xy}^{\text{bg}} H/H_{\text{bg}}}{1 + (H/H_{\text{bg}})^2}. \tag{81b}$$

As follows from Eqs. (78), the scale for the anomalous part can be estimated as

$$\sigma_0^{\text{vH}} \simeq 2e^2 \frac{p_{z0}}{(2\pi)^3} \frac{3\tau K^2}{\sqrt{m_u m_v}},$$

while the definition of the field scale H_0 is in Table I. We observe that the product of conductivity and field scales does not depend on scattering rate and effective masses

$$\sigma_0^{\text{vH}} H_0 \simeq 2\frac{e^2}{\hbar} \frac{\Phi_0}{\pi} \frac{3K^2 p_{z0}}{(2\pi)^3}. \tag{82}$$
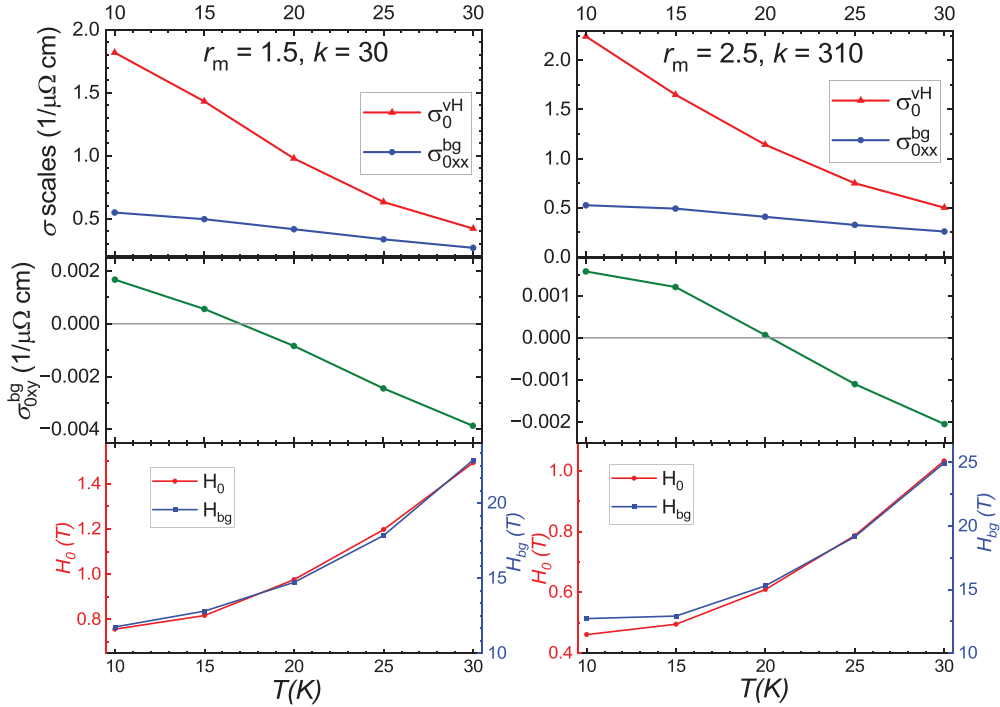
FIG. 12. Temperature dependences of the fitted conductivity and field scales for two sets of the anomalous band parameters.

Using $\frac{e^2}{\hbar} = 2.433 \times 10^{-4} \, \Omega^{-1}$, $K_z = 2\pi/c$ with $c = 0.94$ nm [34], $K = 2\pi/(\sqrt{3}a)$ with $a = 0.55$ nm, we estimate

$$\sigma_0^{\mathrm{vH}} H_0 \approx 11.3 \frac{p_{z0}}{K_z} \frac{T}{\mu\Omega\,\mathrm{cm}}. \tag{83}$$

For modeling, we use only data below 30K which display distinctly anomalous behavior of the Hall resistivity in Fig. 10(b). The experimental field dependences of the diagonal and Hall conductivities for CsV_3Sb_5 we are trying to model are shown in the left column of Fig. 11. They are obtained by inverting the resistivity matrix using experimental data presented in Figs. 10(a) and 10(b), $\sigma_{xx} = \rho_{xx}/(\rho_{xx}^2 + \rho_{yx}^2)$ and $\sigma_{xy} = \rho_{yx}/(\rho_{xx}^2 + \rho_{yx}^2)$. We fixed the temperature-independent band parameters r_m and k and fitted simultaneously two experimental curves $\sigma_{xx}(H)$ and $\sigma_{xy}(H)$ at a given temperature using five fitting parameters for the conductivity and field scales, σ_0^{vH}, $\sigma_{0xx}^{\mathrm{bg}}$, $\sigma_{0xy}^{\mathrm{bg}}$, H_0, and H_{bg}, which vary with temperature. Presumably, this temperature dependence mostly originates from the scattering rate. We also modified the parameters r_m and k to find the set giving the best modeling of the data for all temperatures. We found that for "naively reasonable" parameter sets within the ranges $r_m = 1.2 - 1.8$, $k = 15 - 50$, one can obtain qualitative description of the data with some deviations, see, for example, series of the simulated $\sigma_{\alpha\beta}(H)$ curves in the middle column of Fig. 11 for $r_m = 1.5$ and $k = 30$. Much better fits, however, may be achieved assuming larger mass ratio $r_m = 2.5$ and very large $k = 310$ corresponding to very close proximity to the van Hove point. The modeled curves with these parameters are shown in the right column of Fig. 11.

Figure 12 shows temperature dependences of the fitted conductivity and field scales for the two sets of the anomalous band parameters used in Fig. 11. We can see that all

parameters display regular temperature dependences. The conductivity and field scales for two parameter sets are very close with somewhat smaller field scales for the second set. The anomalous and background diagonal conductivities have similar sizes. Note that the zero-field anomalous conductivity is given by $\sigma_{\alpha\beta}^{\mathrm{vH}}(0) = 0.26\sigma_0^{\mathrm{vH}}$ and $0.25\sigma_0^{\mathrm{vH}}$ for the first and second set, respectively. The scale for the anomalous conductivity is characterized by a stronger temperature dependence. The magnetic field scale for the anomalous part decreases with temperature from 1.45 to 0.8 teslas for the first set and from 1 to 0.5 teslas for the second set. The field scale for the regular contribution is 15–25 times larger. Nevertheless, both scales have very similar temperature dependences described by the law $a + bT^3$. The value of $H_0 = 1$ T together with the estimated values of the masses m_u and m_v gives an estimate for the scattering time $\tau \approx 4.2 \times 10^{-12}$ s. We also observe that the background Hall conductivity changes sign with increasing temperature.

Figure 13 shows temperature dependences of the product $\sigma_0^{\mathrm{vH}} H_0$ for two sets of the anomalous band parameters. Even though Eq. (82) suggests that this product depends only on band parameters, it does have a weak temperature dependence. A comparison of the absolute value of this product with the estimate in Eq. (83) suggests that the large hexagon occupies only small fraction of the Brillouin zone $p_{z0}/K_z \sim 0.1$.

We consider now the behavior at low magnetic fields $\lesssim$ 0.5 T. The linear magnetic-field dependence of the diagonal conductivity crosses over to the quadratic one for $H \rightarrow 0$. This is an expected behavior because the corners at the branch crossing are not infinitely sharp but rounded due opening of the CDW gap, as described in Sec. IX. We model the low-field behavior of the experimental magnetoconductivity using theoretical results from Ref. [60] presented in Sec. IX. Figure 14 shows the representative field dependences of
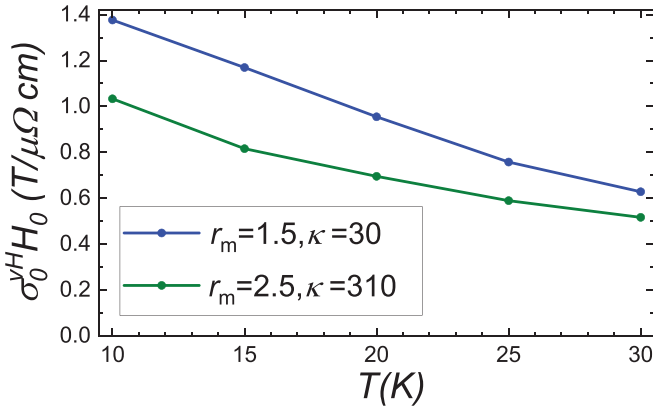
FIG. 13. Temperature dependences of the product $\sigma_0^{vH} H_0$ for two sets of the anomalous band parameters.

diagonal conductivity at low magnetic fields for three temperatures, 10, 20, and 30 K. We can see that these dependences indeed display a clear crossover between quadratic and linear behaviors around 0.1–0.2 T. The solid lines show fits using Eqs. (69) and (73). We see that the crossover is very accurately described by the theory based on the CDW FS reconstruction. The extracted CDW field scale H_Δ defined in Eq. (70) increases from 0.095 T at 10 K to 0.23 T at 30 K. This increase is mostly caused by the temperature dependence of the scattering time. The ratio H_Δ/H_0 is approximately 0.125-0.15 for the parameter set in the left column of Fig. 11. According to Eq. (77), this ratio is determined by the ratio of the CDW gap Δ_{CDW} and the shift of the Fermi level with respect to the van Hove energy ε_{vH}. For $r_m = 1.5$, we estimate the numerical constant in Eq. (77) as $C_m \approx 0.64$. This means that our consideration suggests that Δ_{CDW} is 4–5 times smaller than ε_{vH}.

The ARPES data reported in Refs. [27,28] suggest that the van Hove energy relevant for the large hexagon is located at 100–200 meV below the Fermi level. Also, the feature at -200 meV in the tunneling spectrum of CsV_3Sb_5 has

been attributed to the van Hove singularity in Ref. [70]. On the other hand, the CDW gap at the large-hexagon branch crossing estimated from ARPES [18,26,32] and STM [17,70] is $\sim$20 meV. This means that the relation between Δ_{CDW} and ε_{vH} following from our qualitative analysis is reasonably consistent with the experimental data.

XI. SUMMARY AND DISCUSSION

In summary, we have introduced a minimal model of the large hexagon pocket in the Fermi surface of kagome metals that provides a natural interpretation for the experimentally observed anomalous magnetotransport in the CDW state of the compounds AV_3Sb_5. The shapes of magnetoconductivity components in our model are determined by two dimensionless parameters: the mass ratio of the saddle-point spectrum and the ratio of the reciprocal-lattice vector to the minimum separation of the large-hexagon vertices from the van Hove point.

We evaluated magnetoconductivity components for both large hexagon pocket in the pristine BZ and Fermi-surface sheets emerging from its reconstruction by the CDW order in the folded BZ, small hexagon and two large triangles. Two features account for the anomalous magnetotransport in AV_3Sb_5: proximity of the vertices of a large hexagonal pocket to the van Hove points and the presence of very sharp corners in the reconstructed FS sheets. The magnetoconductivity components of the large hexagon are characterized by the two van Hove magnetic field scales: the lower scale H_0 is determined by the two effective masses of the saddle-point electronic spectrum and the upper scale H_b contains an additional large logarithmic factor diverging as the Fermi energy approaches the van Hove energy. While these two scales are still present for the partial conductivities of the triangular pockets in the reconstructed FS, the third magnetic-field scale H_Δ emerges due to the sharp corners. It is proportional to the CDW gap and is the lowest scale in the problem. For CsV_3Sb_5, our analysis yields the following hierarchy of the field scales at low temperatures: $H_\Delta \approx 0.1$ T, $H_0 \approx 1$ T, and $H_b \approx 7$ T.

The sign of the linear Hall conductivity for the large hexagon and triangles is *negative*, in spite of the hole nature of these Fermi sheets. The reason for this anomalous feature is the proximity of the regions with large positive curvature to the van Hove points in combination with overall concave shape of these pockets. The same feature causes strong nonmonotonic field dependence and sign change of the Hall conductivity. Therefore our model naturally accounts for the anomalous magnetotransport behavior of the kagome family AV_3Sb_5. Furthermore, it allows for a semi-quantitative description of the experimental magnetoconductivity in CsV_3Sb_5 with reasonable fitting parameters. Following the Occam's razor principle, the proposed mechanism provides a more likely explanation for a peculiar behavior of the Hall resistivity than the previously employed interpretation based on spontaneous Hall effect due to chiral CDW. We would like to point, however, that our interpretation by itself does not rule out possibility of a chiral CDW state in these materials considering that the anomalous Hall effect is not the only experimental indication for such a state. One can naturally expect that if a chiral CDW is realized, a random
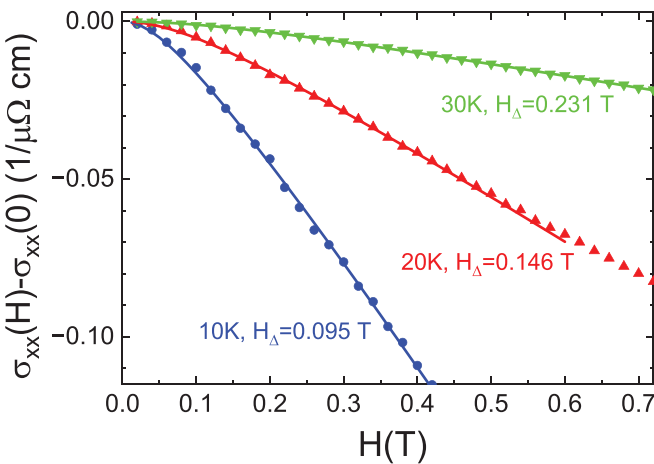

FIG. 14. The field dependences of the diagonal conductivity at low magnetic fields for three temperatures displaying crossover between quadratic and linear behaviors. The solid lines show fits using Eqs. (69) and (73).

array of domains with opposite chiralities would form in a bulk sample. In such multidomain state a small spontaneous Hall effect will be hidden due to the averaging between the domains. This cancellation may persist in a finite magnetic field if it does not generate a single-domain state, which is not obvious *a priori*.

In conclusion, our work reveals the crucial role of van Hove singularities and CDW Fermi-surface reconstruction on the transport phenomena in the kagome superconductors AV_3Sb_5. Since van Hove points are ubiquitous in kagome metals, they very likely influence magnetotransport in other systems including recently discovered kagome families AV_6Sn_6 (A=Y, Gd, Ho, Sc, Sm) [71–75] and ATi_3Bi_5 (A=Cs, Rb) [76–78]. For example, it is highly probable that the mechanism discussed here is responsible for a nonmonotonic, sign-changing magnetic-field dependence of Hall resistivity recently reported for ScV_6Sn_6 [79]. Furthermore, our approach can be extended to a large family of metallic systems hosting singular features in their electronic spectrum.

APPENDIX A: CALCULATION OF HYPERBOLIC HEXAGON AREA AND EFFECTIVE MASS

1. Hyperbolic hexagon

With the Fermi-surface hyperbolic equation

$$p_{F,u}(p_v) = \sqrt{p_{v0}^2 + p_v^2} / \sqrt{r_m},$$

the hexagon area can be written as

$$A_{HH} = 12 \int_0^{p_{vc}} (p_{F,u}(p_v) - \sqrt{3}p_v) dp_v.$$

Using hyperbolic parametrization, we can evaluate this integral as

$$
\begin{aligned}
A_{HH} &= \frac{12 p_{v0}^2}{\sqrt{r_m}} \int_0^{t_c} \cosh^2 t \, dt - 6\sqrt{3} p_{vc}^2 \\
&= \frac{6 p_{v0}^2}{\sqrt{r_m}} \left(t_c + \frac{\sinh 2t_c}{2} \right) - 6\sqrt{3} p_{v0}^2 \sinh^2 t_c \\
&= 6 p_{u0}^2 \sqrt{r_m} t_c.
\end{aligned}
$$

Using the relation $\tanh t_c = \frac{1}{\sqrt{3 r_m}}$, we finally obtain

$$A_{HH} = 3 p_{u0}^2 \sqrt{r_m} \ln \frac{\sqrt{3 r_m} + 1}{\sqrt{3 r_m} - 1}. \tag{A1}$$

For comparison, the area of an ideal hexagon is $A_{hex} = 2\sqrt{3} p_{u0}^2 \approx 3.464 p_{u0}^2$ (clearly, $A_{HH} < A_{hex}$ corresponding to $\sqrt{3 r_m} \ln \frac{\sqrt{3 r_m}+1}{\sqrt{3 r_m}-1} < 2$).

The effective mass probed by magnetic oscillations is defined as

$$m_{HH} = \frac{1}{2\pi} \frac{dA_{HH}}{d\varepsilon_F}$$
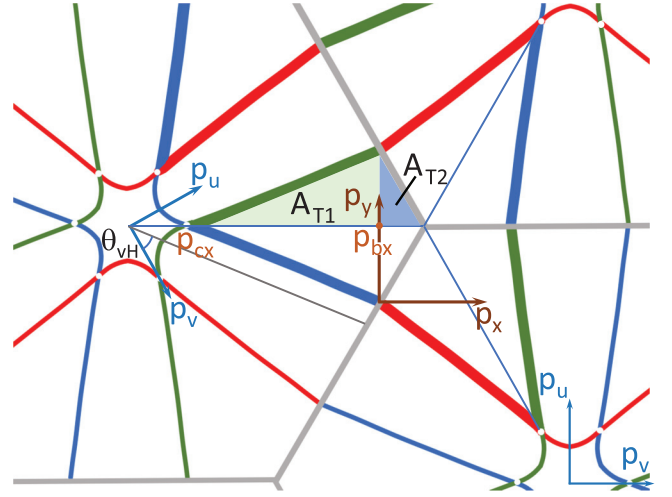

FIG. 15. Triangular pocket composed of the highlighted small triangles with areas A_{T1} and A_{T2} computed in the text.

and from Eq. (A1) we immediately obtain

$$m_{HH} = \frac{3}{\pi} \sqrt{m_u m_v} \ln \frac{\sqrt{3 r_m} + 1}{\sqrt{3 r_m} - 1} = \frac{3}{\pi} m_u \sqrt{r_m} \ln \frac{\sqrt{3 r_m} + 1}{\sqrt{3 r_m} - 1}. \tag{A2}$$

2. Triangular pocket

The triangular pocket is composed of six triangular pieces. Each piece, in turn can be split into two smaller triangles highlighted in Fig. 15. We compute the areas of these two pieces notated as A_{T1} and A_{T2}. The area of the triangle located between the horizontal point p_{cx} and p_{bx} shown in Fig. 15, can be evaluated as

$$A_{T1} = \int_{p_{cx}}^{p_{bx}} p_y(p_x) dp_x.$$

Using hyperbolic parametrization

$$p_x = p_{u0} \left(\frac{1}{2} \sqrt{r_m} \sinh t + \frac{\sqrt{3}}{2} \cosh t \right),$$

$$p_y = p_{u0} \left(\frac{\sqrt{3}}{2} \sqrt{r_m} \sinh t - \frac{1}{2} \cosh t \right),$$

we compute

$$
\begin{aligned}
A_{T1} &= \frac{p_{u0}^2}{4} \int_{t_c}^{t_b} (\sqrt{3 r_m} \sinh t - \cosh t) \\
&\quad \times (\sqrt{r_m} \cosh t + \sqrt{3} \sinh t) dt \\
&= \frac{p_{u0}^2}{8} [(\sqrt{3 r_m} \sinh t_b - \cosh t_b) \\
&\quad \times (\sqrt{r_m} \sinh t_b + \sqrt{3} \cosh t_b) \\
&\quad - 4\sqrt{r_m}(t_b - t_c)]. \tag{A3}
\end{aligned}
$$

The area of the second small triangle can be straightforwardly evaluated as

$$A_{T2} = \frac{1}{2} p_{by} \left(\frac{K}{\sqrt{3}} - p_{xb} \right) = \frac{p_{u0}^2}{8\sqrt{3}} (\sqrt{3r_m} \sinh t_b - \cosh t_b)^2.$$

$$\text{(A4)}$$

Therefore the full area of the triangular pocket is given by

$$A_T = 6(A_{T1} + A_{T2})$$
$$= p_{u0}^2 \left[\frac{\sqrt{3}}{2} (3r_m \sinh^2 t_b - \cosh^2 t_b) - 3\sqrt{r_m}(t_b - t_c) \right]$$

$$\text{(A5)}$$

Using definition of the parameter t_b in Eq. (10), we can also transform this result to a more transparent form

$$A_T = \frac{\sqrt{3}}{2} \frac{\sqrt{3r_m} - 1}{\sqrt{3r_m} + 1} K^2$$
$$- 3\sqrt{r_m} p_{u0}^2 \left(t_b - t_c + \frac{\kappa}{\sqrt{\kappa^2 + 3r_m - 1} + \kappa} \right). \quad \text{(A6)}$$

Using this result and dependencies of p_{u0} and t_b on the Fermi energy, we can also derive the following result for the effective mass of the triangular pocket

$$m_T = \frac{1}{2\pi} \frac{dA_T}{d\varepsilon_F} \approx -\frac{3}{\pi} (t_b - t_c) \sqrt{m_u m_v}. \quad \text{(A7)}$$

Due to proximity to the van Hove point, the effective mass has additional large factor $\sim t_b$.

APPENDIX B: CONDUCTIVITY SLICE $S_{x\beta}$ FOR ARBITRARY POCKET WITH M-FOLD SYMMETRY

Consider a 2D slice of a Fermi surface having m-fold symmetry. We split it into m equivalent segments separated by the momenta p_k with $k = 1, \ldots, m$, located at the Fermi contour. Each segment is assumed to have mirror symmetry. Figure 2(a) illustrates such a split for $m = 6$. We select the local coordinate system for each segment along and perpendicular to the mirror plane. The local axes for the segment with index k are rotated at an angle $\theta_k = 2(k-1)\pi/m + \alpha$ with respect to the laboratory frame. We can split the Fermi velocity into the longitudinal and transverse components, v_l and v_t, which are symmetric and antisymmetric, respectively, with respect to the mirror plane.

To proceed, we rewrite the slice $S_{x\beta}$ in Eq. (18) as

$$S_{x\beta} = \varsigma_{x\beta} \frac{c}{|e|H} \left[1 - \exp \left(-\oint \frac{dp}{v} \frac{c}{|e|H\tau} \right) \right]^{-1}$$
$$\times \oint \frac{dp}{v} v_\beta \mathcal{I}_x(p), \quad \text{(B1)}$$

where

$$\mathcal{I}_x(p) = \oint_p \frac{dp'}{v'} v'_x \exp \left(-\mathfrak{J}_p^{p'} \right)$$

represents the p' integral over the whole orbit for fixed initial momentum p and

$$\mathfrak{J}_p^{p'} \equiv \int_p^{p'} \frac{dp''}{v''} \frac{c}{|e|H\tau} \quad \text{(B2)}$$

is the orbit integral between point p and p', which has an obvious property $\mathfrak{J}_p^{p'} = \mathfrak{J}_p^{p_0} + \mathfrak{J}_{p_0}^{p'}$ for an arbitrary intermediate point p_0 at the orbit. For p located inside the segment $[p_1, p_2]$, the full integral over p' can be split into the segments as

$$\mathcal{I}_x(p) = \int_p^{p_2} \frac{dp'}{v'} v'_x \exp \left(-\mathfrak{J}_p^{p'} \right)$$
$$+ \sum_{k=2}^{m} \exp \left(-\mathfrak{J}_p^{p_2} - \sum_{j=2}^{k-1} \mathfrak{J}_{p_j}^{p_{j+1}} \right)$$
$$\times \int_{p_k}^{p_{k+1}} \frac{dp'}{v'} v'_x \exp \left(-\mathfrak{J}_{p_k}^{p'} \right)$$
$$+ \exp \left(-\mathfrak{J}_p^{p_2} - \sum_{j=2}^{m} \int_{p_j}^{p_{j+1}} \mathfrak{J}_{p_j}^{p_{j+1}} \right)$$
$$\times \int_{p_1}^{p} \frac{dp'}{v'} v'_x \exp \left(-\mathfrak{J}_{p_1}^{p'} \right).$$

For the momentum p' located inside the k's segment $[p_k, p_{k+1}]$, we can expand the velocity over the local longitudinal and transverse components, $v'_x = c_k v'_t - s_k v'_l$ with $c_k = \cos[2(k-1)\pi/m + \alpha]$ and $s_k = \sin[2(k-1)\pi/m + \alpha]$. Since the segments are equivalent, the integrals

$$\mathcal{Q} = \mathfrak{J}_{p_k}^{p_{k+1}}, \quad \text{(B3a)}$$
$$\mathcal{R}_s = \int_{p_k}^{p_{k+1}} \frac{dp'}{v'} v'_s \exp \left(-\mathfrak{J}_{p_k}^{p'} \right) \quad \text{(B3b)}$$

with $s = l, t$ do not depend on the segment index k. This allows us to represent the p' integral as

$$\mathcal{I}_x(p) = \int_p^{p_2} \frac{dp'}{v'} (c_1 v'_t - s_1 v'_l) \exp \left(-\mathfrak{J}_p^{p'} \right)$$
$$+ \exp \left(-\mathfrak{J}_p^{p_2} \right) \sum_{k=2}^{m} \exp \left[-(k-2)\mathcal{Q} \right] (c_k \mathcal{R}_t - s_k \mathcal{R}_l)$$
$$+ \exp \left(-\mathfrak{J}_p^{p_2} - (m-1)\mathcal{Q} \right) \int_{p_1}^{p} \frac{dp'}{v'} (c_1 v'_t - s_1 v'_l)$$
$$\times \exp \left(-\mathfrak{J}_{p_1}^{p'} \right).$$

Further, the last term can be transformed as

$$\exp \left(-\mathfrak{J}_p^{p_2} - (m-1)\mathcal{Q} \right) \int_{p_1}^{p} \frac{dp'}{v'} (c_1 v'_t - s_1 v'_l) \exp \left(-\mathfrak{J}_{p_1}^{p'} \right)$$
$$= \exp \left(-\mathfrak{J}_p^{p_2} - (m-1)\mathcal{Q} \right) (c_1 \mathcal{R}_t - s_1 \mathcal{R}_l)$$
$$- \exp \left(-m\mathcal{Q} \right) \int_p^{p_2} \frac{dp'}{v'} (c_1 v'_t - s_1 v'_l) \exp \left(-\mathfrak{J}_p^{p'} \right),$$

allowing us to combine it with the first two terms and obtain the convenient presentation for $\mathcal{I}_x(p)$,

$$\mathcal{I}_x(p) = [1 - \exp(-m\mathcal{Q})] \int_p^{p_{r+1}} \frac{dp'}{v'} (c_r v'_t - s_r v'_l) \exp \left(-\mathfrak{J}_{p_r}^{p'} \right)$$
$$+ \exp \left(-\mathfrak{J}_p^{p_{r+1}} \right) \sum_{k=r+1}^{r+m} \exp \left[-(k-r-1)\mathcal{Q} \right]$$
$$\times (c_k \mathcal{R}_t - s_k \mathcal{R}_l), \quad \text{(B4)}$$

where we generalized the result for p located inside an arbitrary segment $[p_r, p_{r+1}]$ and used the periodicity $c_{k+m} = c_k$, $s_{k+m} = s_k$. We will use this result for calculation of slices S_{xx} and S_{xy} from Eq. (B1).

1. Diagonal conductivity

We proceed with calculation of the diagonal part of the slice conductivity, S_{xx} from Eq. (B1). The part of the integral in S_{xx} for the momentum p inside the segment $[p_r, p_{r+1}]$ using the result for $\mathcal{I}_x(p)$ in Eq. (B4) can now be written as

$$\frac{c}{|e|H}\int_{p_r}^{p_{r+1}}\frac{dp}{v}v_x\mathcal{I}_x(p) = \frac{c}{|e|H}[1 - \exp(-m\mathcal{Q})]\int_{p_r}^{p_{r+1}}\frac{dp}{v}(c_rv_t - s_rv_l)\int_p^{p_{r+1}}\frac{dp'}{v'}(c_rv_t' - s_rv_l')\exp(-\mathfrak{I}_p^{p'})$$

$$+ \frac{c}{|e|H}\int_{p_r}^{p_{r+1}}\frac{dp}{v}(c_rv_t - s_rv_l)\exp(-\mathfrak{I}_p^{p_{r+1}})\sum_{k=r+1}^{m+r}\exp[-(k - r - 1)\mathcal{Q}](c_k\mathcal{R}_t - s_k\mathcal{R}_l).$$

Using the symmetry properties of v_t and v_l, the integrals in the second line can be related to the segment integrals in Eq. (B3b) as

$$\int_{p_r}^{p_{r+1}}\frac{dp}{v}v_t\exp(-\mathfrak{I}_p^{p_{r+1}}) = -\mathcal{R}_t, \tag{B5a}$$

$$\int_{p_r}^{p_{r+1}}\frac{dp}{v}v_l\exp(-\mathfrak{I}_p^{p_{r+1}}) = \mathcal{R}_l. \tag{B5b}$$

We also introduce the following notations:

$$\mathcal{G}_{sq} = \int_{p_r}^{p_{r+1}}\frac{dp}{v}v_s\int_p^{p_{r+1}}\frac{dp'}{v'}v_q'\exp(-\mathfrak{I}_p^{p'}), \tag{B6}$$

with $s, r = l, t$ for the same-segment integrals in the second line. They also are identical for all segments. This gives the following result for the p integral over the segment $[p_r, p_{r+1}]$

$$\frac{c}{|e|H}\int_{p_r}^{p_{r+1}}\frac{dp}{v}v_x\mathcal{I}_x(p) = \frac{c}{|e|H}[1 - \exp(-m\mathcal{Q})]\big(c_r^2\mathcal{G}_{tt} + s_r^2\mathcal{G}_{ll} - c_rs_r(\mathcal{G}_{tl} + \mathcal{G}_{lt})\big)$$

$$- \frac{c}{|e|H}(c_r\mathcal{R}_t + s_r\mathcal{R}_l)\sum_{k=r+1}^{r+m}\exp[-(k - r - 1)\mathcal{Q}](c_k\mathcal{R}_t - s_k\mathcal{R}_l). \tag{B7}$$

Adding all p segments and using the identities $\sum_{r=1}^m c_r^2 = \sum_{r=1}^m s_r^2 = m/2$ and $\sum_{r=1}^m c_rs_r = 0$, we can write the full result as

$$S_{xx} = \frac{c}{|e|H}\left\{\frac{m}{2}(\mathcal{G}_{tt} + \mathcal{G}_{ll}) - [1 - \exp(-m\mathcal{Q})]^{-1}\sum_{r=1}^m(c_r\mathcal{R}_t + s_r\mathcal{R}_l)\sum_{k=r+1}^{r+m}\exp[-(k - r - 1)\mathcal{Q}](c_k\mathcal{R}_t - s_k\mathcal{R}_l)\right\}. \tag{B8}$$

As $c_k = \cos[2(k - 1)\pi/m + \alpha]$ and $s_k = \sin[2(k - 1)\pi/m + \alpha]$, calculation of the trigonometric sums is facilitated by the complex presentations

$$c_k\mathcal{R}_t - s_k\mathcal{R}_l = \text{Re}\left[\exp\left(\iota\frac{2\pi}{m}(k - 1) + i\alpha\right)(\mathcal{R}_t + \iota\mathcal{R}_l)\right] \tag{B9}$$

and $c_r\mathcal{R}_t + s_r\mathcal{R}_l = \text{Re}[\exp(\iota\frac{2\pi}{m}(r - 1) + \iota\alpha)(\mathcal{R}_t - \iota\mathcal{R}_l)] = \frac{1}{2}\sum_{\delta=\pm 1}\exp(\iota\frac{2\pi}{m}\delta(r - 1) + \iota\delta\alpha)(\mathcal{R}_t - \iota\delta\mathcal{R}_l)$. Using these presentations, we compute the sum over the index k as,

$$\sum_{k=r+1}^{r+m}\exp\left[-(k - r - 1)\mathcal{Q} + \iota\frac{2\pi}{m}(k - 1) + i\alpha\right] = \exp\left(i\alpha + \iota r\frac{2\pi}{m}\right)\frac{1 - \exp(-m\mathcal{Q})}{1 - \exp(-\mathcal{Q} + \iota\frac{2\pi}{m})} \tag{B10}$$

and obtain

$$S_{xx} = \frac{c}{|e|H}\left\{\frac{m}{2}(\mathcal{G}_{tt} + \mathcal{G}_{ll}) - \frac{1}{2}\text{Re}\left[\sum_{\delta=\pm 1}(\mathcal{R}_t - \iota\delta\mathcal{R}_l)\sum_{r=1}^m\exp\left[\iota\frac{2\pi}{m}\delta(r - 1) + \iota r\frac{2\pi}{m} + \iota(\delta + 1)\alpha\right]\frac{\mathcal{R}_t + \iota\mathcal{R}_l}{1 - \exp(-\mathcal{Q} + \iota\frac{2\pi}{m})}\right]\right\}. \tag{B11}$$

As the sum over index r vanishes for $\delta = 1$ and the terms are r independent for $\delta = -1$, we arrive at the final result

$$S_{xx}^{(m)} = \frac{m}{2} \frac{c}{|e|H} \left\{ \mathcal{G}_{tt} + \mathcal{G}_{ll} - \text{Re} \left[\frac{(\mathcal{R}_t + \iota \mathcal{R}_l)^2}{\exp\left(-\iota \frac{2\pi}{m}\right) - \exp\left(-\mathcal{Q}\right)} \right] \right\}$$

$$= \frac{m}{2} \frac{c}{|e|H} \left\{ \mathcal{G}_{tt} + \mathcal{G}_{ll} - \frac{\left(\mathcal{R}_t^2 - \mathcal{R}_l^2\right)\left[\cos\left(\frac{2\pi}{m}\right) - \exp\left(-\mathcal{Q}\right)\right] - 2\mathcal{R}_t\mathcal{R}_l \sin\left(\frac{2\pi}{m}\right)}{1 - 2\cos\left(\frac{2\pi}{m}\right)\exp\left(-\mathcal{Q}\right) + \exp\left(-2\mathcal{Q}\right)} \right\}, \quad \text{(B12)}$$

which expresses the diagonal conductivity slice in terms of segment integrals defined in Eqs. (B3a), (B3b), and (B6).

2. Hall conductivity

The calculation of the Hall component S_{xy} is again based on the presentation in Eq. (B1) in combination with $\mathcal{I}_x(p)$ in Eq. (B4). Using the expansion $v_y = s_r v_t + c_r v_l$, the p integral for segment $[p_r, p_{r+1}]$ in S_{xy} can be represented as

$$\frac{c}{|e|H} \int_{p_r}^{p_{r+1}} \frac{dp}{v} v_y \mathcal{I}_x(p) = \frac{c}{|e|H}[1 - \exp\left(-m\mathcal{Q}\right)] \int_{p_r}^{p_{r+1}} \frac{dp}{v}(s_r v_t + c_r v_l) \int_p^{p_{r+1}} \frac{dp'}{v'}(c_r v_t' - s_r v_l') \exp\left(-\mathfrak{J}_p^{p'}\right)$$

$$+ \frac{c}{|e|H} \int_{p_r}^{p_{r+1}} \frac{dp}{v}(s_r v_t + c_r v_l) \exp\left(-\mathfrak{J}_p^{p_{r+1}}\right) \sum_{k=r+1}^{m+r} \exp\left[-(k-r-1)\mathcal{Q}\right](c_k \mathcal{R}_t - s_k \mathcal{R}_l)$$

$$= \frac{c}{|e|H}[1 - \exp\left(-m\mathcal{Q}\right)]\left(c_r^2 \mathcal{G}_{lt} - s_r^2 \mathcal{G}_{tl} + c_r s_r(\mathcal{G}_{tt} - \mathcal{G}_{ll})\right)$$

$$+ \frac{c}{|e|H}(-s_r \mathcal{R}_t + c_r \mathcal{R}_l) \sum_{k=r+1}^{m+r} \exp\left[-(k-r-1)\mathcal{Q}\right](c_k \mathcal{R}_t - s_k \mathcal{R}_l).$$

Therefore, for the full Hall conductivity slice, we obtain

$$S_{xy} = \varsigma_{xy} \frac{c}{|e|H} \left\{ \frac{m}{2}(\mathcal{G}_{lt} - \mathcal{G}_{tl}) + [1 - \exp\left(-m\mathcal{Q}\right)]^{-1} \sum_{r=1}^{m}(-s_r \mathcal{R}_t + c_r \mathcal{R}_l) \sum_{k=r+1}^{r+m} \exp\left[-(k-r-1)\mathcal{Q}\right](c_k \mathcal{R}_t - s_k \mathcal{R}_l) \right\}. \quad \text{(B13)}$$

Using the complex presentation in Eq. (B9) and $-s_r \mathcal{R}_t + c_r \mathcal{R}_l = \frac{1}{2}\sum_{\delta=\pm 1}\exp(\iota\delta\frac{2\pi}{m}(r-1) + i\delta\alpha)(\iota\delta\mathcal{R}_t + \mathcal{R}_l)$, as well as Eq. (B10) for the sum in the second line, we derive

$$S_{xy} = \varsigma_{xy} \frac{c}{|e|H} \left\{ \frac{m}{2}(\mathcal{G}_{lt} - \mathcal{G}_{tl}) + \frac{1}{2}\text{Re}\left[\sum_{\delta=\pm 1}\sum_{r=1}^{m}\exp\left(\iota\delta\frac{2\pi}{m}(r-1) + \iota r\frac{2\pi}{m} + i(\delta+1)\alpha\right)\frac{(\iota\delta\mathcal{R}_t + \mathcal{R}_l)(\mathcal{R}_t + \iota\mathcal{R}_l)}{1 - \exp\left[-\mathcal{Q} + \iota\frac{2\pi}{m}\right]} \right] \right\}.$$

Again, only the term with $\delta = -1$ is finite yielding the final result

$$S_{xy}^{(m)} = \varsigma_{xy} \frac{m}{2} \frac{c}{|e|H} \left[\mathcal{G}_{lt} - \mathcal{G}_{tl} + \text{Im}\left[\frac{(\mathcal{R}_t + \iota\mathcal{R}_l)^2}{\exp\left(-\iota\frac{2\pi}{m}\right) - \exp\left(-\mathcal{Q}\right)} \right] \right]$$

$$= \varsigma_{xy} \frac{m}{2} \frac{c}{|e|H} \left\{ \mathcal{G}_{lt} - \mathcal{G}_{tl} + \frac{\sin\left(\frac{2\pi}{m}\right)\left(\mathcal{R}_t^2 - \mathcal{R}_l^2\right) + 2\left[\cos\left(\frac{2\pi}{m}\right) - \exp\left(-\mathcal{Q}\right)\right]\mathcal{R}_l\mathcal{R}_t}{1 - 2\exp\left(-\mathcal{Q}\right)\cos\left(\frac{2\pi}{m}\right) + \exp\left(-2\mathcal{Q}\right)} \right\}, \quad \text{(B14)}$$

which have a form similar to the diagonal slice in Eq. (19a).

APPENDIX C: INTEGRATIONS ALONG HYPERBOLIC FERMI SURFACE NEAR VAN HOVE POINT FOR LARGE HEXAGON

In this Appendix, we analytically calculate the segment integrals $\mathcal{R}_k^{\text{LH}}$ and $\mathcal{G}_{km}^{\text{LH}}$ in Eqs. (20b) and (20c) determining the single-slice contribution to conductivity in Eq. (18). The Fermi pocket of the large concave hexagon is approximated by segments of hyperbola, Eq. (7), see Fig. 2. The momenta tracing the Fermi surface can be presented in the local coordinates as

$$p_x = K_{j,x} + p_v c_j - p_u s_j, \quad \text{(C1a)}$$

$$p_y = K_{j,y} + p_v s_j + p_u c_j. \quad \text{(C1b)}$$

for $\frac{\pi}{3}(j-1) < \theta < \frac{\pi}{3}j$, where $p_x = p\cos\theta$, $p_y = p\sin\theta$, $\theta_j = (\pi/3)(j-2)$, with $j = (1, 2, \ldots, 6)$, $c_j \equiv \cos\theta_j$, and $s_j \equiv \sin\theta_j$. For the integrations along the Fermi surface in Eqs. (20b) and (20c), it is convenient to use the hyperbolic parametrization

defined in Eq. (8). Correspondingly, the velocity components in real space are expanded as

$$v_x = v_v c_j - v_u s_j, \tag{C2a}$$

$$v_y = v_v s_j + v_u c_j, \tag{C2b}$$

where $v_v = -\frac{p_v}{m_v}$ and $v_u = \frac{p_u}{m_u}$ are velocity components in hyperbolic basis, which can be parametrized as

$$v_v = v_{v0} \sinh t, \quad v_u = -v_{u0} \cosh t, \tag{C3}$$

with

$$v_{u0} = \frac{p_{u0}}{m_u}, \quad v_{v0} = \frac{p_{v0}}{m_v}, \tag{C4}$$

so that $v_{v0}/v_{u0} = p_{u0}/p_{v0} = 1/\sqrt{r_m}$. Therefore, for the total in-plane velocity, we obtain

$$v = \sqrt{v_{u0}^2 \cosh^2 t + v_{v0}^2 \sinh^2 t}. $$

For the integrations in the exponent of Eq. (18), we obtain the relation

$$\frac{dp}{v} = \frac{\sqrt{(dp_v/dt)^2 + (dp_u/dt)^2}}{\sqrt{v_{u0}^2 \cosh^2 t + v_{v0}^2 \sinh^2 t}} dt = \frac{p_{u0}}{v_{v0}} dt = \sqrt{m_u m_v} dt \tag{C5}$$

yielding

$$\int_p^{p'} \frac{dp''}{v''} \frac{c}{|e|H\tau} = \frac{t'-t}{\omega_h} = -\frac{\mathrm{arcsinh}(p_v'/p_{v0}) - \mathrm{arcsinh}(p_v/p_{v0})}{\omega_h}. \tag{C6}$$

In particular, for the whole-orbit integral in Eq. (18), we have

$$\oint \frac{dp}{v} \frac{c}{|e|H\tau} = \frac{12 t_b}{\omega_h} = 6\mathcal{Q}_{\mathrm{LH}},$$

where the limiting hyperbolic parameter t_b is defined in Eq. (10).

Both $\mathcal{R}_k^{\mathrm{LH}}$ and $\mathcal{G}_{km}^{\mathrm{LH}}$ in Eqs. (20b) and (20c) are determined by the integrals

$$\mathcal{J}_k(p) = \int_p^{p_2} \frac{dp'}{v'} v_k' \exp\left(-\int_p^{p'} \frac{dp''}{v''} \frac{c}{|e|H\tau}\right) \tag{C7}$$

with $k = v, u$. Using the hyperbolic parametrization for the point at the Fermi surface, $p(t)$, and for the Fermi velocities, Eqs. (8) and (C3), these integrals can be evaluated analytically

$$\mathcal{J}_v(t) = p_{u0} G_v(t_b, t), \tag{C8a}$$

$$\mathcal{J}_u(t) = -p_{v0} G_u(t_b, t), \tag{C8b}$$

where the functions $G_v(t_2, t_1)$ and $G_u(t_2, t_1)$ are defined and evaluated as

$$G_v(t_2, t_1) \equiv \int_{t_1}^{t_2} dt' \sinh t' \exp\left(-\frac{t'-t_1}{\omega_h}\right) = \frac{\left(\cosh t_2 + \frac{1}{\omega_h} \sinh t_2\right) \exp\left(-\frac{t_2-t_1}{\omega_h}\right) - \left(\cosh t_1 + \frac{1}{\omega_h} \sinh t_1\right)}{1 - \omega_h^{-2}}, \tag{C9a}$$

$$G_u(t_2, t_1) \equiv \int_{t_1}^{t_2} dt' \cosh t' \exp\left(-\frac{t'-t_1}{\omega_h}\right) = \frac{\left(\sinh t_2 + \frac{1}{\omega_h} \cosh t_2\right) \exp\left(-\frac{t_2-t_1}{\omega_h}\right) - \left(\sinh t_1 + \frac{1}{\omega_h} \cosh t_1\right)}{1 - \omega_h^{-2}}, \tag{C9b}$$

and we also used the relations $\sqrt{m_u m_v} v_{v0} = p_{u0}$, $\sqrt{m_u m_v} v_{u0} = p_{v0}$.

The integrals over the whole segment $[p_1, p_2]$ defined in Eq. (20b) are given by $\mathcal{R}_s^{\mathrm{LH}} = \mathcal{J}_s(-t_b)$ with $s = u, v$. Introducing shortened notations $G_{bs} \equiv G_s(t_b, -t_b)$, we can present $\mathcal{R}_v^{\mathrm{LH}} = p_{u0} G_{bv}$ and $\mathcal{R}_u^{\mathrm{LH}} = -p_{v0} G_{bu}$. The explicit presentations for the functions G_{bv} and G_{bu} directly following from Eqs. (C9a) and (C9b) are given in Eqs. (24a) and (24b). One can also derive alternative presentations

$$G_{bv} = -2 \exp\left(-\frac{t_b}{\omega_h}\right) \frac{\cosh t_b \sinh(t_b/\omega_h) - \frac{1}{\omega_h} \sinh t_b \cosh(t_b/\omega_h)}{1 - \omega_h^{-2}}, \tag{C10a}$$

$$G_{bu} = 2 \exp\left(-\frac{t_b}{\omega_h}\right) \frac{\sinh t_b \cosh(t_b/\omega_h) - \frac{1}{\omega_h} \cosh t_b \sinh(t_b/\omega_h)}{1 - \omega_h^{-2}}. \tag{C10b}$$

These functions have the following asymptotics:

$$G_{bv} \simeq \begin{cases} -\omega_h(\sinh t_b - \omega_h \cosh t_b), & \text{for } \omega_h \ll 1 \\ -\frac{2}{\omega_h}(t_b \cosh t_b - \sinh t_b), & \text{for } \omega_h \gg 2t_b \end{cases}, \tag{C11a}$$

$$G_{bu} \simeq \begin{cases} \omega_h(\cosh t_b - \omega_h \sinh t_b), & \text{for } \omega_h \ll 1 \\ 2 \sinh t_b\left(1 - \frac{t_b}{\omega_h}\right), & \text{for } \omega_h \gg 2t_b \end{cases}. \tag{C11b}$$

In calculations, we will also need the supplemental integrals over p defined as

$$\bar{\mathcal{R}}_v^{\text{LH}} = \int_{p_1}^{p_2} \frac{dp}{v} v_v \exp\left(-\int_p^{p_2} \frac{dp''}{v''} \frac{c}{|e|H\tau}\right) = -\mathcal{R}_v^{\text{LH}}, \tag{C12a}$$

$$\bar{\mathcal{R}}_u^{\text{LH}} = \int_{p_1}^{p_2} \frac{dp}{v} v_u \exp\left(-\int_p^{p_2} \frac{dp''}{v''} \frac{c}{|e|H\tau}\right) = \mathcal{R}_u^{\text{LH}}. \tag{C12b}$$

We now evaluate the same-segment integrals $\mathcal{G}_{km}^{\text{LH}}$ in Eq. (20c). The term $\mathcal{G}_{vv}^{\text{LH}}$ is connected with the integral $\mathcal{J}_v(p)$ defined in Eq. (C7) as

$$\mathcal{G}_{vv}^{\text{LH}} = \int_{p_1}^{p_2} \frac{dp}{v} v_v \mathcal{J}_v(p).$$

Using again the hyperbolic parametrization for for p and v_v together with the result for $\mathcal{J}_v(p)$ in Eqs. (C8a) and (C9a), we compute

$$\mathcal{G}_{vv}^{\text{LH}} = p_{u0}^2 K_{bvv},$$

$$\begin{aligned} K_{bvv} &= \int_{-t_b}^{t_b} dt \sinh t\, G_v(t_b, t) \\ &= \frac{1}{1 - \omega_h^{-2}}\left[\left(\cosh t_b + \frac{1}{\omega_h}\sinh t_b\right)\frac{\cosh t_b - \omega_h^{-2}\sinh t_b - \exp\left(-\frac{2}{\omega_h}t_b\right)\left(\cosh t_b + \frac{1}{\omega_h}\sinh t_b\right)}{1 - \omega_h^{-2}} - \frac{1}{2\omega_h}(\sinh 2t_b - 2t_b)\right] \\ &= \frac{1}{1 - \omega_h^{-2}}\left[\sinh^2 t_b + \frac{1 - \exp\left(-\frac{2}{\omega_h}t_b\right)\left(\cosh t_b + \frac{1}{\omega_h}\sinh t_b\right)^2}{1 - \omega_h^{-2}} - \frac{1}{2\omega_h}(\sinh 2t_b - 2t_b)\right]. \end{aligned} \tag{C13}$$

Even though this result contains $1 - \omega_h^{-2}$ denominators, one can check that it does not diverge and approaches a finite limit for $\omega_h \to 1$,

$$K_{bvv} \to \frac{1}{2}\left\{\frac{\sinh(2t_b)}{2}\left(1 + \frac{\exp(-2t_b)}{2}\right) - \exp(-2t_b)t_b - \frac{t_b(1 + 2t_b)}{2}\right\}.$$

In a similar way, one can evaluate the term

$$\mathcal{G}_{uu}^{\text{LH}} = \int_{p_1}^{p_2} \frac{dp}{v} v_u \mathcal{J}_u(p)$$

using the result for $\mathcal{J}_u(p)$ in Eqs. (C8b) and (C9b). Explicit calculation gives

$$\mathcal{G}_{uu}^{\text{LH}} = p_{v0}^2 K_{buu},$$

$$\begin{aligned} K_{buu} &= \int_{-t_b}^{t_b} dt \cosh t\, G_u(t_b, t) \\ &= \frac{1}{1 - \omega_h^{-2}}\left[\left(\sinh t_b + \frac{1}{\omega_h}\cosh t_b\right)\frac{\sinh t_b - \frac{1}{\omega_h^2}\cosh t_b + \exp\left(-\frac{2}{\omega_h}t_b\right)\left(\sinh t_b + \frac{1}{\omega_h}\cosh t_b\right)}{1 - \omega_h^{-2}} - \frac{1}{\omega_h}\left(\frac{\sinh 2t_b}{2} + t_b\right)\right] \\ &= \frac{1}{1 - \omega_h^{-2}}\left[\cosh^2 t_b - \frac{1 - \exp\left(-\frac{2}{\omega_h}t_b\right)\left(\sinh t_b + \frac{1}{\omega_h}\cosh t_b\right)^2}{1 - \omega_h^{-2}} - \frac{1}{\omega_h}\left(\frac{\sinh 2t_b}{2} + t_b\right)\right]. \end{aligned} \tag{C14}$$

The functions $\mathcal{K}_{bss}$ have the following asymptotics.

$$\mathcal{K}_{bvv} \simeq \begin{cases} \omega_h\left[\left(\frac{\sinh 2t_b}{2} - t_b\right) - \omega_h \sinh^2 t_b\right], & \text{for } \omega_h \ll 1 \\ \frac{1}{\omega_h}\left[t_b(\cosh 2t_b + 2) - \frac{3\sinh 2t_b}{2}\right], & \text{for } \omega_h \gg 2t_b \end{cases} \tag{C15}$$

$$\mathcal{K}_{buu} \simeq \begin{cases} \omega_h\left[\left(\frac{\sinh 2t_b}{2} + t_b\right) - \omega_h \cosh^2 t_b\right], & \text{for } \omega_h \ll 1 \\ 2\sinh^2 t_b + \frac{1}{\omega_h}\left(\frac{\sinh 2t_b}{2} - t_b(2\sinh^2 t_b + 1)\right), & \text{for } \omega_h \gg 2t_b \end{cases} \tag{C16}$$

The Hall component also contains the off-diagonal function,

$$\mathcal{G}_{uv}^{\text{LH}} = \int_{p_1}^{p_2} \frac{dp}{v} v_u \mathcal{J}_v(p),$$

which we evaluate as

$$\mathcal{G}_{uv}^{\text{LH}} = -p_{u0}p_{v0}K_{buv},$$

$$K_{buv} = \int_{-t_b}^{t_b} dt \cosh t\, G_v(t_b,, t)$$

$$= \frac{1}{1 - \omega_h^{-2}}\left[\left(\cosh t_b + \frac{1}{\omega_h}\sinh t_b\right)\frac{\left(\sinh t_b - \frac{1}{\omega_h}\cosh t_b\right) + \left(\sinh t_b + \frac{1}{\omega_h}\cosh t_b\right)\exp\left(-\frac{2}{\omega_h}t_b\right)}{1 - \omega_h^{-2}} - \frac{\sinh 2t_b}{2} - t_b\right]$$

$$= \frac{1}{1 - \omega_h^{-2}}\left[\frac{-\frac{1}{\omega_h} + \left[(1 + \omega_h^{-2})\sinh(2t_b)/2 + \frac{1}{\omega_h}\cosh(2t_b)\right]\exp\left(-\frac{2}{\omega_h}t_b\right)}{1 - \omega_h^{-2}} - t_b\right]. \tag{C17}$$

This function has the following asymptotics:

$$\mathcal{K}_{buv} \simeq \begin{cases} \omega_h^2(t_b - \omega_h), & \text{for } \omega_h \ll 1 \\ \frac{1}{2}\sinh(2t_b) - t_b - \frac{1}{\omega_h}[1 + t_b \sinh(2t_b) - \cosh(2t_b)], & \text{for } \omega_h \gg 2t_b \end{cases} \tag{C18}$$

One can demonstrate antisymmetry with respect to the index switching, $\mathcal{G}_{vu}^{\text{LH}} = -\mathcal{G}_{uv}^{\text{LH}}$.

In addition to the asymptotic limit $\omega_h \gg 2t_b$, the functions G_{bs} and $\mathcal{K}_{bst}$ are also characterized by more general asymptotic limits valid in the whole range $\omega_h \gg 1$:

$$G_{bv} \simeq -\cosh t_b(1 - \eta_{\text{LH}}), \quad G_{bu} \simeq \sinh t_b(1 + \eta_{\text{LH}}), \tag{C19a}$$

$$\mathcal{K}_{bvv} \simeq \cosh^2 t_b(1 - \eta_{\text{LH}}), \quad \mathcal{K}_{buu} \simeq \sinh^2 t_b(1 + \eta_{\text{LH}}), \tag{C19b}$$

$$\mathcal{K}_{buv} \simeq -t_b + \eta_{\text{LH}} \sinh t_b \cosh t_b \tag{C19c}$$

with $\eta_{\text{LH}} \equiv \exp(-2t_b/\omega_h)$. These asymptotics also describe behavior in the intermediate field range $1 \ll \omega_h \ll 2t_b$.

APPENDIX D: MAGNETOCONDUCTIVITY CONTRIBUTION FOR TRIANGULAR POCKETS

In this Appendix we evaluate the conductivity slices for the triangular pocket illustrated in Figs. 3(c) and 4 based on the general presentations in Eqs. (50a) and (50b). For this, we need to evaluate the segment integrals in Eqs. (20a), (20b), and (20c). In our model, the segment is the triangle side, which is composed of "outgoing" and "incoming" hyperbola branches.

We will again use the local hyperbolic coordinates p_v and p_u for every branch. However, contrary to the hexagon pockets, the transverse and longitudinal directions do not coincide with these coordinates. This means that we need to expand the transverse and longitudinal velocity components v_t and v_l over the hyperbolic components v_v and v_u for every hyperbola branch. We write these expansions in a unified way as

$$v_s = \alpha_{a,s}v_u + \beta_{a,s}v_v, \tag{D1}$$

where $s = t, l$, the index $a = o, i$ corresponds to the outgoing and incoming branches, and the coefficients are given by

$$\alpha_{o,l} = \alpha_{i,l} = \beta_{o,t} = \beta_{i,t} = \frac{\sqrt{3}}{2}, \quad \alpha_{o,t} = -\alpha_{i,t} = -\beta_{o,l} = \beta_{i,l} = \frac{1}{2}.$$

The presentations in Eq. (D1) can be also rewritten in a compact complex way as $v_t + \iota v_l = \exp(-\iota\delta\frac{\pi}{6})(v_v + \iota v_u)$ with $\delta = 1(-1)$ for the outgoing (incoming) branch. We will use the hyperbolic parametrization defined in Eq. (8), in which the hyperbolic parameter t varies in the range $t_c < t < t_b$ for the outgoing branch and $-t_b < t < -t_c$ for the incoming branch. The hyperbolic velocity components v_v and v_u are parametrized identically with the large hexagon in Eq. (C3). Note that v_l is continuous and v_t has a jump at the matching point between outgoing and incoming branches.

Relations in Eqs. (C5) and (C6) allow us straightforwardly evaluate the parameter $\mathcal{Q}_\mathrm{T} = \int_{p_k}^{p_{k+1}} \frac{dp'}{v'} \frac{c}{|e|H\tau}$ yielding the result in Eq. (52). We evaluate the integrals $\mathcal{R}_s^\mathrm{T}$ in Eq. (50a) for the segment between p_k and p_{k+1} as

$$\mathcal{R}_s^\mathrm{T} = \int_{p_k}^{p_b} \frac{dp'}{v'}(\alpha_{o,s}v_u' + \beta_{o,s}v_v')\exp\left(-\mathfrak{J}_{p_k}^{p'}\right) + \exp\left(-\mathfrak{J}_{p_k}^{p_b}\right)\int_{p_b}^{p_{k+1}} \frac{dp'}{v'}(\alpha_{i,s}v_u' + \beta_{i,s}v_v')\exp\left(-\mathfrak{J}_{p_b}^{p'}\right), \tag{D2}$$

where p_b is the momentum at the matching point between outgoing and incoming branches and we again employ the notation $\mathfrak{J}_p^{p'}$ for the orbit integral between the points p and p' as defined in Eq. (B2). Introducing the contributions from the outgoing and incoming branches

$$\mathcal{R}_{o,s}^\mathrm{T} = \int_{p_k}^{p_b} \frac{dp'}{v'}v_s'\exp\left(-\mathfrak{J}_{p_k}^{p'}\right), \tag{D3a}$$

$$\mathcal{R}_{i,s}^\mathrm{T} = \int_{p_b}^{p_{k+1}} \frac{dp'}{v'}v_s'\exp\left(-\mathfrak{J}_{p_b}^{p'}\right), \tag{D3b}$$

we rewrite the presentation in Eq. (D2) as

$$\mathcal{R}_s^\mathrm{T} = \mathcal{R}_{o,s}^\mathrm{T} + \sqrt{\eta_T}\mathcal{R}_{i,s}^\mathrm{T} \tag{D4}$$

with $\eta_T \equiv \exp(-\mathcal{Q}_\mathrm{T})$. Substituting the hyperbolic parametrization, we obtain

$$\mathcal{R}_{o,s}^\mathrm{T} = \int_{t_c}^{t_b} dt'(-\alpha_{o,s}p_{v0}\cosh t' + \beta_{o,s}p_{u0}\sinh t')\exp\left(-\frac{t'-t_c}{\omega_h}\right) = -\alpha_{o,s}p_{v0}G_{bcu} + \beta_{o,s}p_{u0}G_{bcv}, \tag{D5a}$$

$$\mathcal{R}_{i,s}^\mathrm{T} = \int_{-t_b}^{-t_c} dt'(-\alpha_{i,s}p_{v0}\cosh t' + \beta_{i,s}p_{u0}\sinh t')\exp\left(-\frac{t'+t_b}{\omega_h}\right) = -\alpha_{i,s}p_{v0}G_{cbu} + \beta_{i,s}p_{u0}G_{cbv}, \tag{D5b}$$

where we introduced notations

$$G_{bck} = G_k(t_b, t_c), \quad G_{cbk} = G_k(-t_c, -t_b)$$

with $k = u, v$ and the functions $G_k(t_2, t_1)$ with $k = v, u$ defined as

$$G_v(t_2, t_1) = \int_{t_1}^{t_2} dt'\sinh t'\exp\left(-\frac{t'-t_1}{\omega_h}\right), \quad G_u(t_2, t_1) = \int_{t_1}^{t_2} dt'\cosh t'\exp\left(-\frac{t'-t_1}{\omega_h}\right)$$

are evaluated in Eqs. (55a) and (55b). The functions G_{bck} and G_{cbk} have the following asymptotic limits

$$G_{bcv} \simeq \omega_h\sinh t_c, \quad G_{bcu} \simeq \omega_h\cosh t_c, \tag{D6}$$

$$G_{cbv} \simeq -\omega_h\sinh t_b, \quad G_{cbu} \simeq \omega_h\cosh t_b \tag{D7}$$

for $\omega_h \ll 1$ and

$$G_{bcv} \simeq \cosh t_b\sqrt{\eta_T} - \cosh t_c, \quad G_{bcu} \simeq \sinh t_b\sqrt{\eta_T} - \sinh t_c, \tag{D8}$$

$$G_{cbv} \simeq \cosh t_c\sqrt{\eta_T} - \cosh t_b, \quad G_{cbu} \simeq -\sinh t_c\sqrt{\eta_T} + \sinh t_b \tag{D9}$$

for $\omega_h \gg 1$.

Using complex presentation for the trigonometric coefficients

$$\alpha_{o,t} + \iota\alpha_{o,l} = \iota\exp\left(-\iota\frac{\pi}{6}\right), \quad \alpha_{i,t} + \iota\alpha_{i,l} = \iota\exp\left(\iota\frac{\pi}{6}\right), \quad \beta_{o,t} + \iota\beta_{o,l} = \exp\left(-\iota\frac{\pi}{6}\right), \quad \beta_{i,t} + \iota\beta_{i,l} = \exp\left(\iota\frac{\pi}{6}\right),$$

and introducing two complex functions $\mathcal{G}_{bc}$ and $\mathcal{G}_{cb}$ in Eq. (53), we obtain complex combination which determines the conductivity slices in Eqs. (50a) and (50b).

$$\mathcal{R}_t^\mathrm{T} + \iota\mathcal{R}_l^\mathrm{T} = p_{u0}\exp\left(-\iota\frac{\pi}{6}\right)\left[\mathcal{G}_{bc} + \exp\left(-\frac{\mathcal{Q}_\mathrm{T}}{2} + \iota\frac{\pi}{3}\right)\mathcal{G}_{cb}\right]. \tag{D10}$$

For the combination in Eqs. (50a) and (50b), we find

$$\frac{\left(\mathcal{R}_t^\mathrm{T} + \iota\mathcal{R}_l^\mathrm{T}\right)^2}{\exp\left(-\iota\frac{2\pi}{3}\right) - \exp(-\mathcal{Q}_\mathrm{T})} = p_{u0}^2\frac{\exp\left(-\iota\frac{\pi}{3}\right)\mathcal{G}_{bc}^2 + 2\exp\left(-\frac{\mathcal{Q}_\mathrm{T}}{2}\right)\mathcal{G}_{bc}\mathcal{G}_{cb} + \exp\left(-\mathcal{Q}_\mathrm{T} + \iota\frac{\pi}{3}\right)\mathcal{G}_{cb}^2}{\exp\left(-\iota\frac{2\pi}{3}\right) - \exp(-\mathcal{Q}_\mathrm{T})}. \tag{D11}$$

The same-segment integrals $\mathcal{G}_{sr}^{\mathrm{T}}$ defined in Eq. (20c), we also split into contributions from incoming and outgoing segments,

$$
\mathcal{G}_{sr}^{\mathrm{T}} = \int_{p_k}^{p_b} \frac{dp}{v} v_s \int_{p}^{p_b} \frac{dp'}{v'} v_r' \exp\left(-\mathfrak{J}_p^{p'}\right) + \int_{p_k}^{p_b} \frac{dp}{v} v_s \exp\left(-\mathfrak{J}_p^{p_b}\right) \int_{p_b}^{p_{k+1}} \frac{dp'}{v'} v_r' \exp\left(-\mathfrak{J}_{p_b}^{p'}\right)
$$
$$
+ \int_{p_b}^{p_{k+1}} \frac{dp}{v} v_s \int_{p}^{p_{k+1}} \frac{dp'}{v'} v_r' \exp\left(-\mathfrak{J}_p^{p'}\right).
$$

The middle term here can be transformed as

$$
\int_{p_k}^{p_b} \frac{dp}{v} v_s \exp\left(-\mathfrak{J}_p^{p_b}\right) \int_{p_b}^{p_{k+1}} \frac{dp'}{v'} v_r' \exp\left(-\mathfrak{J}_{p_b}^{p'}\right) = \delta_s \mathcal{R}_{i,s}^{\mathrm{T}} \mathcal{R}_{i,r}^{\mathrm{T}}
$$

with $\delta_l = 1$, $\delta_t = -1$, where the integrals $\mathcal{R}_{i,s}^{\mathrm{T}}$ are defined in Eq. (D3b) and evaluated in Eq. (D5b). Here we used an alternative presentation for $\mathcal{R}_{i,s}^{\mathrm{T}}$, $\mathcal{R}_{i,s}^{\mathrm{T}} = \delta_s \int_{p_k}^{p_b} \frac{dp}{v} v_s \exp(-\mathfrak{J}_p^{p_b})$ following from the symmetry properties of the velocity components. Substituting hyperbolic parametrization, we obtain

$$
\mathcal{G}_{sr}^{\mathrm{T}} = \int_{t_c}^{t_b} dt (\alpha_{o,s} p_{v0} \cosh t - \beta_{o,s} p_{u0} \sinh t)(\alpha_{o,r} p_{v0} G_u(t_b, t) - \beta_{o,r} p_{u0} G_v(t_b, t)) + \delta_s \mathcal{R}_{i,s}^{\mathrm{T}} \mathcal{R}_{i,r}^{\mathrm{T}}
$$
$$
+ \int_{-t_b}^{-t_c} dt (\alpha_{i,s} p_{v0} \cosh t - \beta_{i,s} p_{u0} \sinh t)(\alpha_{i,r} p_{v0} G_u(-t_c, t) - \beta_{i,r} p_{u0} G_v(-t_c, t)),
$$

where we used identities

$$
\int_{t_c}^{t_b} dt \sinh t \exp\left(-\frac{t_b - t}{\omega_h}\right) = -G_v(-t_c, -t_b), \qquad \int_{t_c}^{t_b} dt \cosh t \exp\left(-\frac{t_b - t}{\omega_h}\right) = G_u(-t_c, -t_b).
$$

Introducing the integrals $\mathcal{K}_{\alpha\beta}(t_2, t_1)$ as

$$
\mathcal{K}_{vv}(t_2, t_1) = \int_{t_1}^{t_2} dt \sinh t\, G_v(t_2, t), \quad \mathcal{K}_{uu}(t_2, t_1) = \int_{t_1}^{t_2} dt \cosh t\, G_u(t_2, t),
$$
$$
\mathcal{K}_{vu}(t_2, t_1) = \int_{t_1}^{t_2} dt \sinh t\, G_u(t_2, t), \quad \mathcal{K}_{uv}(t_2, t_1) = \int_{t_1}^{t_2} dt \cosh t\, G_v(t_2, t),
$$

we arrive at the finite presentation for the same-segment integrals,

$$
\mathcal{G}_{sr}^{\mathrm{T}} = (\alpha_{o,s}\alpha_{o,r} + \alpha_{i,s}\alpha_{i,r}) p_{v0}^2 \mathcal{K}_{uu}(t_b, t_c) + (\beta_{o,s}\beta_{o,r} + \beta_{i,s}\beta_{i,r}) p_{u0}^2 \mathcal{K}_{vv}(t_b, t_c)
$$
$$
- p_{v0} p_{u0} [(\alpha_{o,s}\beta_{o,r} - \beta_{i,s}\alpha_{i,r}) \mathcal{K}_{uv}(t_b, t_c) + (\beta_{o,s}\alpha_{o,r} - \alpha_{i,s}\beta_{i,r}) \mathcal{K}_{vu}(t_b, t_c)] + \delta_s \mathcal{R}_{i,s}^{\mathrm{T}} \mathcal{R}_{i,r}^{\mathrm{T}}. \tag{D12}
$$

The functions $\mathcal{K}_{\alpha\beta}(t_2, t_1)$ can be analytically evaluated as

$$
\mathcal{K}_{vv}(t_2, t_1) = \frac{1}{1 - \omega_h^{-2}} \left\{ \left(\cosh t_2 + \frac{1}{\omega_h}\sinh t_2\right) \frac{\cosh t_2 - \frac{1}{\omega_h}\sinh t_2 - \exp\left(-\frac{1}{\omega_h}(t_2 - t_1)\right)\left(\cosh t_1 - \frac{1}{\omega_h}\sinh t_1\right)}{1 - \omega_h^{-2}} \right.
$$
$$
\left. - \frac{\cosh(2t_2) - \cosh(2t_1)}{4} - \frac{1}{2\omega_h}\left[\frac{\sinh(2t_2) - \sinh(2t_1)}{2} - t_2 + t_1\right] \right\},
$$

$$
\mathcal{K}_{uu}(t_2, t_1) = \frac{1/2}{1 - \frac{1}{\omega_h^2}} \left\{ 2\left(\sinh t_2 + \frac{1}{\omega_h}\cosh t_2\right) \frac{\sinh t_2 - \frac{1}{\omega_h}\cosh t_2 - \exp\left[-\frac{1}{\omega_h}(t_2 - t_1)\right]\left(\sinh t_1 - \frac{1}{\omega_h}\cosh t_1\right)}{1 - \omega_h^{-2}} \right.
$$
$$
\left. - \frac{\cosh(2t_2) - \cosh(2t_1)}{2} - \frac{1}{\omega_h}\left(\frac{\sinh(2t_2) - \sinh(2t_1)}{2} + t_2 - t_1\right) \right\},
$$

$$
\mathcal{K}_{vu}(t_2, t_1) = \frac{1}{1 - \omega_h^{-2}} \left\{ \frac{\frac{1}{\omega_h} - \exp\left(-\frac{t_2 - t_1}{\omega_h}\right)\left(\sinh t_2 + \frac{1}{\omega_h}\cosh t_2\right)\left(\cosh t_1 - \frac{1}{\omega_h}\sinh t_1\right)}{1 - \frac{1}{\omega_h^2}} \right.
$$
$$
\left. + \frac{\sinh(2t_2) + \sinh(2t_1)}{4} + \frac{t_2 - t_1}{2} - \frac{1}{\omega_h}\frac{\cosh(2t_2) - \cosh(2t_1)}{4} \right\},
$$

$$\mathcal{K}_{uv}(t_2, t_1) = \frac{1}{1 - \frac{1}{\omega_h^2}} \left\{ -\frac{\frac{1}{\omega_h} + \exp\left(-\frac{t_2 - t_1}{\omega_h}\right)\left(\cosh t_2 + \frac{1}{\omega_h}\sinh t_2\right)\left(\sinh t_1 - \frac{1}{\omega_h}\cosh t_1\right)}{1 - \frac{1}{\omega_h^2}} \right.$$
$$\left. + \frac{\sinh(2t_2) + \sinh(2t_1)}{4} - \frac{t_2 - t_1}{2} - \frac{1}{\omega_h}\frac{\cosh(2t_2) - \cosh(2t_1)}{4} \right\}.$$

These functions have the symmetry properties

$$\mathcal{K}_{ss}(-t_1, -t_2) = \mathcal{K}_{ss}(t_2, t_1), \quad \mathcal{K}_{vu}(-t_1, -t_2) = -\mathcal{K}_{uv}(t_2, t_1),$$

which we have already used to simplify Eq. (D12). The functions $\mathcal{K}_{\alpha\beta}(t_b, t_c)$ have the following behavior in different limits:

$$\mathcal{K}_{vv}(t_b, t_c) \simeq \frac{\omega_h}{2}\left(\frac{\sinh(2t_b) - \sinh(2t_c)}{2} - t_b + t_c\right) - \frac{\omega_h^2}{2}\left(\frac{\cosh(2t_b) + \cosh(2t_c)}{2} - 1\right), \tag{D13}$$

$$\mathcal{K}_{uu}(t_b, t_c) \simeq \frac{\omega_h}{2}\left(\frac{\sinh(2t_b) - \sinh(2t_c)}{2} + t_b - t_c\right) - \frac{\omega_h^2}{2}\left(\frac{\cosh(2t_b) + \cosh(2t_c)}{2} + 1\right), \tag{D14}$$

$$\mathcal{K}_{vu}(t_b, t_c) = \frac{\omega_h}{4}(\cosh(2t_b) - \cosh(2t_c)) - \frac{\omega_h^2}{4}(\sinh(2t_b) + \sinh(2t_c) + 2(t_b - t_c)) \tag{D15}$$

for $\omega_h \ll 1$ and

$$\mathcal{K}_{vv}(t_b, t_c) \simeq \frac{\cosh^2 t_b + \cosh^2 t_c}{2} - \cosh t_b \cosh t_c \sqrt{\eta_T}, \tag{D16}$$

$$\mathcal{K}_{uu}(t_b, t_c) \simeq \frac{\sinh^2 t_b + \sinh^2 t_c}{2} - \sinh t_b \sinh t_c \sqrt{\eta_T}, \tag{D17}$$

$$\mathcal{K}_{vu}(t_b, t_c) \simeq \frac{\sinh(2t_b) + \sinh(2t_c)}{4} + \frac{t_b - t_c}{2} - \sqrt{\eta_T}\sinh t_b \cosh t_c \tag{D18}$$

for $\omega_h \gg 1$.

We proceed with evaluation of the diagonal conductivity slice S_{xx}^T based on the complex presentation in Eq. (50a). For combination in the first line of Eq. (50a), we obtain from Eq. (D12)

$$\mathcal{G}_{tt}^T + \mathcal{G}_{ll}^T = 2p_{v0}^2 \mathcal{K}_{uu}(t_b, t_c) + 2p_{u0}^2 \mathcal{K}_{vv}(t_b, t_c) + \frac{1}{2}p_{v0}^2 G_{cbu}^2 - \sqrt{3}p_{v0}p_{u0}G_{cbu}G_{cbv} - \frac{1}{2}p_{u0}^2 G_{cbv}^2. \tag{D19}$$

Using the complex function $\mathcal{G}_{cb}$ introduced in Eq. (53), we can combine the three last terms in this equation as

$$\frac{1}{2}p_{v0}^2 G_{cbu}^2 - \sqrt{3}p_{v0}p_{u0}G_{cbu}G_{cbv} - \frac{1}{2}p_{u0}^2 G_{cbv}^2 = -p_{u0}^2 \text{Re}\left[\exp\left(\iota\frac{\pi}{3}\right)\mathcal{G}_{cb}^2\right].$$

Substituting the above results and Eq. (D11) into Eq. (50a), we obtain

$$S_{xx}^T = \frac{3}{2}\frac{c}{|e|H}p_{u0}^2 \left\{ 2\mathcal{K}_{vv}(t_b, t_c) + 2r_m \mathcal{K}_{uu}(t_b, t_c) \right.$$
$$\left. - \text{Re}\left[\exp\left(\iota\frac{\pi}{3}\right)\mathcal{G}_{cb}^2 + \frac{\exp\left(-\iota\frac{\pi}{3}\right)\mathcal{G}_{bc}^2 + 2\mathcal{G}_{bc}\exp\left(-\frac{\mathcal{Q}_T}{2}\right)\mathcal{G}_{cb} + \exp\left(-\mathcal{Q}_T + \iota\frac{\pi}{3}\right)\mathcal{G}_{cb}^2}{\exp\left(-\iota\frac{2\pi}{3}\right) - \exp(-\mathcal{Q}_T)}\right] \right\},$$

which is identical to the result in Eq. (51b) of the main text.

For the Hall conductivity slice in Eq. (50b), we need the function $\mathcal{G}_{lt}^T$, which we evaluate from the general presentation in Eq. (D12) as

$$\mathcal{G}_{lt}^T = -p_{v0}p_{u0}[\mathcal{K}_{uv}(t_b, t_c) - \mathcal{K}_{vu}(t_b, t_c)] - \frac{\sqrt{3}}{4}(p_{v0}^2 G_{cbu}^2 - p_{u0}^2 G_{cbv}^2) - \frac{1}{2}p_{v0}p_{u0}G_{cbv}G_{cbu}. \tag{D20}$$

Using the complex function $\mathcal{G}_{cb}$ in Eq. (53), the last terms in this equation can be presented as

$$-\frac{\sqrt{3}}{4}(p_{v0}^2 G_{cbu}^2 - p_{u0}^2 G_{cbv}^2) - \frac{1}{2}p_{v0}p_{u0}G_{cbv}G_{cbu} = \frac{p_{u0}^2}{2}\text{Im}\left[\exp\left(\iota\frac{\pi}{3}\right)\mathcal{G}_{cb}^2\right].$$

As $\mathcal{G}_{tl}^{\mathrm{T}} = -\mathcal{G}_{lt}^{\mathrm{T}}$, substituting the above results and Eq. (D11) into Eq. (50b) yields

$$
S_{xy}^{\mathrm{T}} = -\frac{3}{2}\frac{c}{|e|H}p_{u0}^2\Bigg\{2\sqrt{r_m}[\mathcal{K}_{vu}(t_b,t_c) - \mathcal{K}_{uv}(t_b,t_c)]
$$
$$
+ \mathrm{Im}\Bigg[\exp\left(\iota\frac{\pi}{3}\right)\mathcal{G}_{cb}^2 + \frac{\exp\left(-\iota\frac{\pi}{3}\right)\mathcal{G}_{bc}^2 + 2\mathcal{G}_{bc}\exp\left(-\frac{\mathcal{Q}_{\mathrm{T}}}{2}\right)\mathcal{G}_{cb} + \exp\left(-\mathcal{Q}_{\mathrm{T}} + \iota\frac{\pi}{3}\right)\mathcal{G}_{cb}^2}{\exp\left(-\iota\frac{2\pi}{3}\right) - \exp\left(-\mathcal{Q}_{\mathrm{T}}\right)}\Bigg]\Bigg\}.
$$

This result is equivalent to Eq. (51c) of the main text. Note that the difference $\mathcal{K}_{vu}(t_b,t_c) - \mathcal{K}_{uv}(t_b,t_c)$ in the first line can be represented in alternative form:

$$
\mathcal{K}_{vu}(t_b,t_c) - \mathcal{K}_{uv}(t_b,t_c) = -\frac{\exp\left[\left(1-\frac{1}{\omega_h}\right)(t_b-t_c)\right]-1}{2\left(1-\frac{1}{\omega_h}\right)^2} + \frac{\exp\left[-\left(1+\frac{1}{\omega_h}\right)(t_b-t_c)\right]-1}{2\left(1+\frac{1}{\omega_h}\right)^2} + \frac{t_b-t_c}{1-\frac{1}{\omega_h^2}},
$$

which is somewhat more convenient for numerical evaluation.

---

[1] H.-M. Guo and M. Franz, Topological insulator on the kagome lattice, Phys. Rev. B **80**, 113102 (2009).

[2] W.-S. Wang, Z.-Z. Li, Y.-Y. Xiang, and Q.-H. Wang, Competing electronic orders on kagome lattices at van Hove filling, Phys. Rev. B **87**, 115135 (2013).

[3] I. I. Mazin, H. O. Jeschke, F. Lechermann, H. Lee, M. Fink, R. Thomale, and R. Valenti, Theoretical prediction of a strongly correlated Dirac metal, Nat. Commun. **5**, 4261 (2014).

[4] W.-H. Ko, P. A. Lee, and X.-G. Wen, Doped kagome system as exotic superconductor, Phys. Rev. B **79**, 214502 (2009).

[5] S.-L. Yu and J.-X. Li, Chiral superconducting phase and chiral spin-density-wave phase in a Hubbard model on the kagome lattice, Phys. Rev. B **85**, 144402 (2012).

[6] M. L. Kiesel, C. Platt, and R. Thomale, Unconventional Fermi surface instabilities in the kagome Hubbard model, Phys. Rev. Lett. **110**, 126405 (2013).

[7] X. Feng, K. Jiang, Z. Wang, and J. Hu, Chiral flux phase in the kagome superconductor AV$_3$Sb$_5$, Sci. Bull. **66**, 1384 (2021).

[8] M. M. Denner, R. Thomale, and T. Neupert, Analysis of charge order in the kagome metal AV$_3$Sb$_5$ (A =K,Rb,Cs), Phys. Rev. Lett. **127**, 217601 (2021).

[9] Y.-P. Lin and R. M. Nandkishore, Complex charge density waves at van hove singularity on hexagonal lattices: Haldane-model phase diagram and potential realization in the kagome metals AV$_3$Sb$_5$ (A=K,Rb,Cs), Phys. Rev. B **104**, 045122 (2021).

[10] H. D. Scammell, J. Ingham, T. Li, and O. P. Sushkov, Chiral excitonic order from twofold van Hove singularities in kagome metals, Nat. Commun. **14**, 605 (2023).

[11] B. R. Ortiz, L. C. Gomes, J. R. Morey, M. Winiarski, M. Bordelon, J. S. Mangum, I. W. H. Oswald, J. A. Rodriguez-Rivera, J. R. Neilson, S. D. Wilson, E. Ertekin, T. M. McQueen, and E. S. Toberer, New kagome prototype materials: Discovery of KV$_3$Sb$_5$, RbV$_3$Sb$_5$, and CsV$_3$Sb$_5$, Phys. Rev. Mater. **3**, 094407 (2019).

[12] H. Chen, B. Hu, Y. Ye, H. Yang, and H.-J. Gao, Superconductivity and unconventional density waves in vanadium-based kagome materials AV$_3$Sb$_5$, Chin. Phys. B **31**, 097405 (2022).

[13] T. Neupert, M. M. Denner, J.-X. Yin, R. Thomale, and M. Z. Hasan, Charge order and superconductivity in kagome materials, Nat. Phys. **18**, 137 (2022).

[14] K. Jiang, T. Wu, J.-X. Yin, Z. Wang, M. Z. Hasan, S. D. Wilson, X. Chen, and J. Hu, Kagome superconductors AV$_3$Sb$_5$ (A = K,Rb,Cs), Natl. Sci. Rev. **10**, nwac199 (2023).

[15] Y. Hu, X. Wu, A. P. Schnyder, and M. Shi, Electronic landscape of kagome superconductors AV$_3$Sb$_5$ (A = K,Rb,Cs) from angle-resolved photoemission spectroscopy, npj Quantum Mater. **8**, 67 (2023).

[16] B. R. Ortiz, S. M. L. Teicher, L. Kautzsch, P. M. Sarte, N. Ratcliff, J. Harter, J. P. C. Ruff, R. Seshadri, and S. D. Wilson, Fermi surface mapping and the nature of charge-density-wave order in the kagome superconductor CsV$_3$Sb$_5$, Phys. Rev. X **11**, 041030 (2021).

[17] Y.-X. Jiang, J.-X. Yin, M. M. Denner, N. Shumiya, B. R. Ortiz, G. Xu, Z. Guguchia, J. He, M. S. Hossain, X. Liu, J. Ruff, L. Kautzsch, S. S. Zhang, G. Chang, I. Belopolski, Q. Zhang, T. A. Cochran, D. Multer, M. Litskevich, Z.-J. Cheng *et al.*, Unconventional chiral charge order in kagome superconductor KV$_3$Sb$_5$, Nat. Mater. **20**, 1353 (2021).

[18] Z. Wang, Y.-X. Jiang, J.-X. Yin, Y. Li, G.-Y. Wang, H.-L. Huang, S. Shao, J. Liu, P. Zhu, N. Shumiya, M. S. Hossain, H. Liu, Y. Shi, J. Duan, X. Li, G. Chang, P. Dai, Z. Ye, G. Xu, Y. Wang *et al.*, Electronic nature of chiral charge order in the kagome superconductor CsV$_3$Sb$_5$, Phys. Rev. B **104**, 075148 (2021).

[19] N. Shumiya, M. S. Hossain, J.-X. Yin, Y.-X. Jiang, B. R. Ortiz, H. Liu, Y. Shi, Q. Yin, H. Lei, S. S. Zhang, G. Chang, Q. Zhang, T. A. Cochran, D. Multer, M. Litskevich, Z.-J. Cheng, X. P. Yang, Z. Guguchia, S. D. Wilson, and M. Z. Hasan, Intrinsic nature of chiral charge order in the kagome superconductor RbV$_3$Sb$_5$, Phys. Rev. B **104**, 035131 (2021).

[20] L. Yu, C. Wang, Y. Zhang, M. Sander, S. Ni, Z. Lu, S. Ma, Z. Wang, Z. Zhao, H. Chen, K. Jiang, Y. Zhang, H. Yang, F. Zhou, X. Dong, S. L. Johnson, M. J. Graf, J. Hu, H.-J. Gao, and Z. Zhao, Evidence of a hidden flux phase in the topological kagome metal CsV$_3$Sb$_5$, arXiv:2107.10714.

[21] Y. Xu, Z. Ni, Y. Liu, B. R. Ortiz, Q. Deng, S. D. Wilson, B. Yan, L. Balents, and L. Wu, Three-state nematicity and magneto-optical Kerr effect in the charge density waves in kagome superconductors, Nat. Phys. **18**, 1470 (2022).

[22] R. Khasanov, D. Das, R. Gupta, C. Mielke, M. Elender, Q. Yin, Z. Tu, C. Gong, H. Lei, E. T. Ritz, R. M. Fernandes, T. Birol,

Z. Guguchia, and H. Luetkens, Time-reversal symmetry broken by charge order in CsV$_3$Sb$_5$, Phys. Rev. Res. **4**, 023244 (2022).

[23] C. Mielke, D. Das, J.-X. Yin, H. Liu, R. Gupta, Y.-X. Jiang, M. Medarde, X. Wu, H. C. Lei, J. Chang, P. Dai, Q. Si, H. Miao, R. Thomale, T. Neupert, Y. Shi, R. Khasanov, M. Z. Hasan, H. Luetkens, and Z. Guguchia, Time-reversal symmetry-breaking charge order in a kagome superconductor, Nature (London) **602**, 245 (2022).

[24] T. Le, Z. Pan, Z. Xu, J. Liu, J. Wang, Z. Lou, X. Yang, Z. Wang, Y. Yao, C. Wu, and X. Lin, Superconducting diode effect and interference patterns in kagome CsV$_3$Sb$_5$, Nature (London) **630**, 64 (2024).

[25] S. Cho, H. Ma, W. Xia, Y. Yang, Z. Liu, Z. Huang, Z. Jiang, X. Lu, J. Liu, Z. Liu, J. Li, J. Wang, Y. Liu, J. Jia, Y. Guo, J. Liu, and D. Shen, Emergence of new van Hove singularities in the charge density wave state of a topological kagome metal RbV$_3$Sb$_5$, Phys. Rev. Lett. **127**, 236401 (2021).

[26] K. Nakayama, Y. Li, T. Kato, M. Liu, Z. Wang, T. Takahashi, Y. Yao, and T. Sato, Multiple energy scales and anisotropic energy gap in the charge-density-wave phase of the kagome superconductor CsV$_3$Sb$_5$, Phys. Rev. B **104**, L161112 (2021).

[27] M. Kang, S. Fang, J.-K. Kim, B. R. Ortiz, S. H. Ryu, J. Kim, J. Yoo, G. Sangiovanni, D. Di Sante, B.-G. Park, C. Jozwiak, A. Bostwick, E. Rotenberg, E. Kaxiras, S. D. Wilson, J.-H. Park, and R. Comin, Twofold van Hove singularity and origin of charge order in topological kagome superconductor CsV$_3$Sb$_5$, Nat. Phys. **18**, 301 (2022).

[28] Y. Hu, X. Wu, B. R. Ortiz, S. Ju, X. Han, J. Ma, N. C. Plumb, M. Radovic, R. Thomale, S. D. Wilson, A. P. Schnyder, and M. Shi, Rich nature of van Hove singularities in kagome superconductor CsV$_3$Sb$_5$, Nat. Commun. **13**, 2220 (2022).

[29] T. Kato, Y. Li, T. Kawakami, M. Liu, K. Nakayama, Z. Wang, A. Moriya, K. Tanaka, T. Takahashi, Y. Yao, and T. Sato, Three-dimensional energy gap and origin of charge-density wave in kagome superconductor KV$_3$Sb$_5$, Comm. Mater. **3**, 30 (2022).

[30] R. Lou, A. Fedorov, Q. Yin, A. Kuibarov, Z. Tu, C. Gong, E. F. Schwier, B. Büchner, H. Lei, and S. Borisenko, Charge-density-wave-induced peak-dip-hump structure and the multiband superconductivity in a kagome superconductor CsV$_3$Sb$_5$, Phys. Rev. Lett. **128**, 036402 (2022).

[31] Y. Luo, S. Peng, S. M. L. Teicher, L. Huai, Y. Hu, Y. Han, B. R. Ortiz, Z. Liang, Z. Wei, J. Shen, Z. Ou, B. Wang, Y. Miao, M. Guo, M. Hashimoto, D. Lu, Z. Qiao, Z. Wang, S. D. Wilson, X. Chen *et al.*, Electronic states dressed by an out-of-plane supermodulation in the quasi-two-dimensional kagome superconductor CsV$_3$Sb$_5$, Phys. Rev. B **105**, L241111 (2022).

[32] H. Luo, Q. Gao, H. Liu, Y. Gu, D. Wu, C. Yi, J. Jia, S. Wu, X. Luo, Y. Xu, L. Zhao, Q. Wang, H. Mao, G. Liu, Z. Zhu, Y. Shi, K. Jiang, J. Hu, Z. Xu, and X. J. Zhou, Electronic nature of charge density wave and electron-phonon coupling in kagome superconductor KV$_3$Sb$_5$, Nat. Commun. **13**, 273 (2022).

[33] Y. Hu, X. Wu, B. R. Ortiz, X. Han, N. C. Plumb, S. D. Wilson, A. P. Schnyder, and M. Shi, Coexistence of trihexagonal and star-of-David pattern in the charge density wave of the kagome superconductor AV$_3$Sb$_5$, Phys. Rev. B **106**, L241106 (2022).

[34] Y. Fu, N. Zhao, Z. Chen, Q. Yin, Z. Tu, C. Gong, C. Xi, X. Zhu, Y. Sun, K. Liu, and H. Lei, Quantum transport evidence of topological band structures of kagome superconductor CsV$_3$Sb$_5$, Phys. Rev. Lett. **127**, 207002 (2021).

[35] K. Shrestha, R. Chapai, B. K. Pokharel, D. Miertschin, T. Nguyen, X. Zhou, D. Y. Chung, M. G. Kanatzidis, J. F. Mitchell, U. Welp, D. Popović, D. E. Graf, B. Lorenz, and W. K. Kwok, Nontrivial Fermi surface topology of the kagome superconductor CsV$_3$Sb$_5$ probed by de Haas–van Alphen oscillations, Phys. Rev. B **105**, 024508 (2022).

[36] W. Zhang, L. Wang, C. W. Tsang, X. Liu, J. Xie, W. C. Yu, K. T. Lai, and S. K. Goh, Emergence of large quantum oscillation frequencies in thin flakes of the kagome superconductor CsV$_3$Sb$_5$, Phys. Rev. B **106**, 195103 (2022).

[37] X. Huang, C. Guo, C. Putzke, M. Gutierrez-Amigo, Y. Sun, M. G. Vergniory, I. Errea, D. Chen, C. Felser, and P. J. W. Moll, Three-dimensional Fermi surfaces from charge order in layered CsV$_3$Sb$_5$, Phys. Rev. B **106**, 064510 (2022).

[38] C. Broyles, D. Graf, H. Yang, X. Dong, H. Gao, and S. Ran, Effect of the interlayer ordering on the Fermi surface of kagome superconductor CsV$_3$Sb$_5$ revealed by quantum oscillations, Phys. Rev. Lett. **129**, 157001 (2022).

[39] R. Chapai, M. Leroux, V. Oliviero, D. Vignolles, N. Bruyant, M. P. Smylie, D. Y. Chung, M. G. Kanatzidis, W.-K. Kwok, J. F. Mitchell, and U. Welp, Magnetic breakdown and topology in the kagome superconductor CsV$_3$Sb$_5$ under high magnetic field, Phys. Rev. Lett. **130**, 126401 (2023).

[40] H. Tan, Y. Liu, Z. Wang, and B. Yan, Charge density waves and electronic properties of superconducting kagome metals, Phys. Rev. Lett. **127**, 046401 (2021).

[41] H. LaBollita and A. S. Botana, Tuning the van Hove singularities in AV$_3$Sb$_5$(A =K,Rb,Cs) via pressure and doping, Phys. Rev. B **104**, 205129 (2021).

[42] M. Y. Jeong, H.-J. Yang, H. S. Kim, Y. B. Kim, S. Lee, and M. J. Han, Crucial role of out-of-plane Sb p orbitals in van Hove singularity formation and electronic correlations in the superconducting kagome metal CsV$_3$Sb$_5$, Phys. Rev. B **105**, 235145 (2022).

[43] H. Tan, Y. Li, Y. Liu, D. Kaplan, Z. Wang, and B. Yan, Emergent topological quantum orbits in the charge density wave phase of kagome metal CsV$_3$Sb$_5$, npj Quantum Mater. **8**, 39 (2023).

[44] F. Ferrari, F. Becca, and R. Valentí, Charge density waves in kagome-lattice extended Hubbard models at the van Hove filling, Phys. Rev. B **106**, L081107 (2022).

[45] J. E. Hirsch and D. J. Scalapino, Enhanced superconductivity in quasi two-dimensional systems, Phys. Rev. Lett. **56**, 2732 (1986).

[46] I. E. Dzyaloshinskii, Superconducting transitions due to van Hove singularities in the electron spectrum, Zh. Eksp. Teor. Fiz. **93**, 1487 (1987) [Sov. Phys.-JETP **66**, 848 (1987)].

[47] R. S. Markiewicz, A survey of the van Hove scenario for high-T$_c$ superconductivity with special emphasis on pseudogaps and striped phases, J. Phys. Chem. Solids **58**, 1179 (1997).

[48] V. Y. Irkhin, A. A. Katanin, and M. I. Katsnelson, Robustness of the van Hove scenario for high-T$_c$ superconductors, Phys. Rev. Lett. **89**, 076401 (2002).

[49] Y. Luo, Y. Han, J. Liu, H. Chen, Z. Huang, L. Huai, H. Li, B. Wang, J. Shen, S. Ding, Z. Li, S. Peng, Z. Wei, Y. Miao, X. Sun, Z. Ou, Z. Xiang, M. Hashimoto, D. Lu, Y. Yao *et al.*, A unique van Hove singularity in kagome superconductor CsV$_{3-x}$Ta$_x$Sb$_5$ with enhanced superconductivity, Nat. Commun. **14**, 3819 (2023).

[50] S.-Y. Yang, Y. Wang, B. R. Ortiz, D. Liu, J. Gayles, E. Derunova, R. Gonzalez-Hernandez, L. Šmejkal, Y. Chen,

S. S. P. Parkin, S. D. Wilson, E. S. Toberer, T. McQueen, and M. N. Ali, Giant, unconventional anomalous Hall effect in the metallic frustrated magnet candidate, KV_3Sb_5, Sci. Adv. **6**, eabb6003 (2020).

[51] F. H. Yu, T. Wu, Z. Y. Wang, B. Lei, W. Z. Zhuo, J. J. Ying, and X. H. Chen, Concurrence of anomalous Hall effect and charge density wave in a superconducting topological kagome metal, Phys. Rev. B **104**, L041103 (2021).

[52] X. Zhou, H. Liu, W. Wu, K. Jiang, Y. Shi, Z. Li, Y. Sui, J. Hu, and J. Luo, Anomalous thermal Hall effect and anomalous Nernst effect of CsV_3Sb_5, Phys. Rev. B **105**, 205104 (2022).

[53] G. Zheng, C. Tan, Z. Chen, M. Wang, X. Zhu, S. Albarakati, M. Algarni, J. Partridge, L. Farrar, J. Zhou, W. Ning, M. Tian, M. S. Fuhrer, and L. Wang, Electrically controlled superconductor-to-failed insulator transition and giant anomalous Hall effect in kagome metal CsV_3Sb_5 nanoflakes, Nat. Commun. **14**, 678 (2023).

[54] N. Nagaosa, J. Sinova, S. Onoda, A. H. MacDonald, and N. P. Ong, Anomalous Hall effect, Rev. Mod. Phys. **82**, 1539 (2010).

[55] A. V. Maharaj, I. Esterlis, Y. Zhang, B. J. Ramshaw, and S. A. Kivelson, Hall number across a van Hove singularity, Phys. Rev. B **96**, 045132 (2017).

[56] F. Herman, J. Buhmann, M. H. Fischer, and M. Sigrist, Deviation from Fermi-liquid transport behavior in the vicinity of a van Hove singularity, Phys. Rev. B **99**, 184107 (2019).

[57] R.-Y. Mao, D. Wang, C. Wu, and Q.-H. Wang, Magnetotransport in overdoped $La_{2-x}Sr_xCuO_4$: Fermi liquid approach, Phys. Rev. B **104**, 024501 (2021).

[58] A. B. Pippard, *Magnetoresistance in Metals* (Cambridge University Press, New York, 1989).

[59] J. Fenton and A. J. Schofield, Breakdown of weak-field magnetotransport at a metallic quantum critical point, Phys. Rev. Lett. **95**, 247201 (2005).

[60] A. E. Koshelev, Linear magnetoconductivity in multiband spin-density-wave metals with nonideal nesting, Phys. Rev. B **88**, 060412(R) (2013).

[61] J. Lin and A. J. Millis, Theory of low-temperature Hall effect in electron-doped cuprates, Phys. Rev. B **72**, 214506 (2005).

[62] Y. Wang, Z. Chen, Y. Nie, Y. Zhang, Q. Niu, G. Zheng, X. Zhu, W. Ning, and M. Tian, Nontrivial fermi surface topology and large anomalous Hall effect in the kagome superconductor RbV_3Sb_5, Phys. Rev. B **108**, 035117 (2023).

[63] N. P. Ong, Geometric interpretation of the weak-field Hall conductivity in two-dimensional metals with arbitrary Fermi surface, Phys. Rev. B **43**, 193 (1991).

[64] A. A. Abrikosov, *Fundamentals of the Theory of Metals* (Dover Publications, Mineola, New York, 2017).

[65] W. Shockley, Effect of magnetic fields on conduction - "tube integrals", Phys. Rev. **79**, 191 (1950).

[66] Note that the counterclockwise integration direction in Eq. (18) coincides with direction of orbital motion for hole pockets while for electron pockets the orbital motion is clockwise.

[67] M. Abdel-Jawad, M. P. Kennett, L. Balicas, A. Carrington, A. P. Mackenzie, R. H. McKenzie, and N. E. Hussey, Anisotropic scattering and anomalous normal-state transport in a high-temperature superconductor, Nat. Phys. **2**, 821 (2006).

[68] J. Ayres, M. Berben, M. Čulo, Y.-T. Hsu, E. van Heumen, Y. Huang, J. Zaanen, T. Kondo, T. Takeuchi, J. R. Cooper, C. Putzke, S. Friedemann, A. Carrington, and N. E. Hussey, Incoherent transport across the strange-metal regime of overdoped cuprates, Nature (London) **595**, 661 (2021).

[69] Y. Fang, G. Grissonnanche, A. Legros, S. Verret, F. Laliberté, C. Collignon, A. Ataei, M. Dion, J. Zhou, D. Graf, M. J. Lawler, P. A. Goddard, L. Taillefer, and B. J. Ramshaw, Fermi surface transformation at the pseudogap critical point of a cuprate superconductor, Nat. Phys. **18**, 558 (2022).

[70] H. Zhao, H. Li, B. R. Ortiz, S. M. L. Teicher, T. Park, M. Ye, Z. Wang, L. Balents, S. D. Wilson, and I. Zeljkovic, Cascade of correlated electron states in the kagome superconductor CsV_3Sb_5, Nature (London) **599**, 216 (2021).

[71] G. Pokharel, S. M. L. Teicher, B. R. Ortiz, P. M. Sarte, G. Wu, S. Peng, J. He, R. Seshadri, and S. D. Wilson, Electronic properties of the topological kagome metals YV_6Sn_6 and GdV_6Sn_6, Phys. Rev. B **104**, 235139 (2021).

[72] S. Peng, Y. Han, G. Pokharel, J. Shen, Z. Li, M. Hashimoto, D. Lu, B. R. Ortiz, Y. Luo, H. Li, M. Guo, B. Wang, S. Cui, Z. Sun, Z. Qiao, S. D. Wilson, and J. He, Realizing kagome band structure in two-dimensional kagome surface states of RV_6Sn_6 (R = Gd, Ho), Phys. Rev. Lett. **127**, 266401 (2021).

[73] H. W. S. Arachchige, W. R. Meier, M. Marshall, T. Matsuoka, R. Xue, M. A. McGuire, R. P. Hermann, H. Cao, and D. Mandrus, Charge density wave in kagome lattice intermetallic ScV_6Sn_6, Phys. Rev. Lett. **129**, 216402 (2022).

[74] X. Huang, Z. Cui, C. Huang, M. Huo, H. Liu, J. Li, F. Liang, L. Chen, H. Sun, B. Shen, Y. Zhang, and M. Wang, Anisotropic magnetism and electronic properties of the kagome metal SmV_6Sn_6, Phys. Rev. Mater. **7**, 054403 (2023).

[75] Y. Hu, J. Ma, Y. Li, Y. Jiang, D. J. Gawryluk, T. Hu, J. Teyssier, V. Multian, Z. Yin, S. Xu, S. Shin, I. Plokhikh, X. Han, N. C. Plumb, Y. Liu, J.-X. Yin, Z. Guguchia, Y. Zhao, A. P. Schnyder, X. Wu *et al.*, Phonon promoted charge density wave in topological kagome metal ScV_6Sn_6, Nat. Commun. **15**, 1658 (2024).

[76] H. Yang, Z. Zhao, X.-W. Yi, J. Liu, J.-Y. You, Y. Zhang, H. Guo, X. Lin, C. Shen, H. Chen, X. Dong, G. Su, and H.-J. Gao, Titanium-based kagome superconductor $CsTi_3Bi_5$ and topological states, arXiv:2209.03840.

[77] B. Liu, M.-Q. Kuang, Y. Luo, Y. Li, C. Hu, J. Liu, Q. Xiao, X. Zheng, L. Huai, S. Peng, Z. Wei, J. Shen, B. Wang, Y. Miao, X. Sun, Z. Ou, S. Cui, Z. Sun, M. Hashimoto, D. Lu *et al.*, Tunable van Hove singularity without structural instability in kagome metal $CsTi_3Bi_5$, Phys. Rev. Lett. **131**, 026701 (2023).

[78] Z. Jiang, Z. Liu, H. Ma, W. Xia, Z. Liu, J. Liu, S. Cho, Y. Yang, J. Ding, J. Liu, Z. Huang, Y. Qiao, J. Shen, W. Jing, X. Liu, J. Liu, Y. Guo, and D. Shen, Flat bands, non-trivial band topology and rotation symmetry breaking in layered kagome-lattice $RbTi_3Bi_5$, Nat. Commun. **14**, 4892 (2023).

[79] S. Mozaffari, W. R. Meier, R. P. Madhogaria, N. Peshcherenko, S.-H. Kang, J. W. Villanova, H. W. S. Arachchige, G. Zheng, Y. Zhu, K.-W. Chen, K. Jenkins, D. Zhang, A. Chan, L. Li, M. Yoon, Y. Zhang, and D. G. Mandrus, Universal sublinear resistivity in vanadium kagome materials hosting charge density waves, Phys. Rev. B **110**, 035135 (2024).